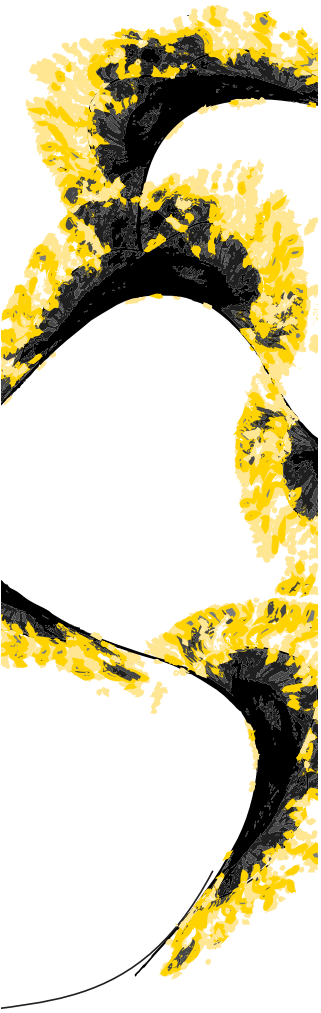

RAM ROBOTICS AND MECHATRONICS

DESIGN, FABRICATION AND EVALUATION OF A 3D PRINTED THRUST SENSOR FOR APPLICATION IN DRONES

N.T. (Nikhil) Shenoy

MSC ASSIGNMENT

Committee:
prof. dr. ir. G.J.M. Krijnen
G.J.W. Wolterink, MSc
A. Franchi, PhD
dr. L.D. De Santana

February, 2021

006RaM2021
Robotics and Mechatronics
EEMCS
University of Twente
P.O. Box 217
7500 AE Enschede
The Netherlands

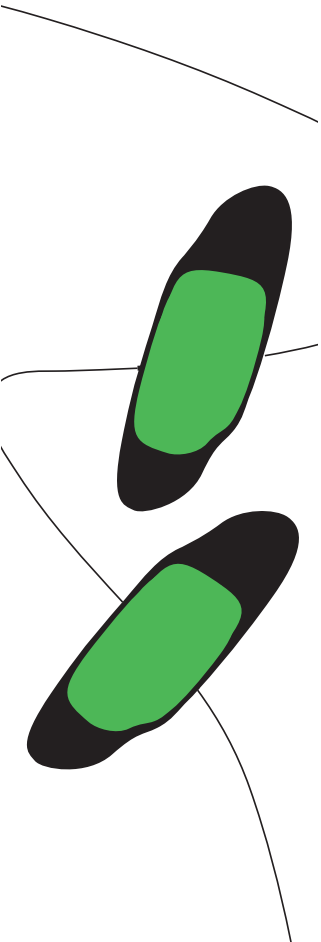

UNIVERSITY OF TWENTE. | TECHMED CENTRE UNIVERSITY OF TWENTE. | DIGITAL SOCIETY INSTITUTE

List of Figures

List of Tables

Summary

Recently, additive manufacturing, best known from 3D printing, has become a common method for fabricating a wide range of sensors. With 3D printing, sensors can now be fabricated with sufficient surface finish and accuracy. Furthermore, it is now possible to fabricate entire sensors or by embedding the sensor into printed structures.

This master thesis assignment deals with the design and fabrication of a 3D printed thrust sensor to be implemented on drones. Amongst other things, this approach of integrated sensors in standard structures of the drone by the use of 3D printing provides the flexibility to upgrade sensor designs easily so as to meet varying and customised requirements.

In this assignment, the lift force of a rotating propeller was first analysed considering two scenarios: blade flapping and drone arm deflection. The two scenarios were analysed using Finite Element Method (FEM) simulations and several factors were taken into account: implementation of the sensor, effect of additional weight, ease of 3D printing and so on. Based on the comparison between the two, it was deemed suitable to compute thrust by measuring the deflection of the drone arm.

The first part of the assignment deals with the design and fabrication of the sensor using two materials: Polylactic Acid (PLA) and Conductive PLA. With the help of FEM analysis, stress and strain distribution is analyzed on the drone arm to find an optimal position for sensor placement. Using a linear actuator, the sensor is then characterised to determine non-linearity, drift , hysteresis and repeatability. The results from characterisation are then validated using a motor setup.

The second part of the assignment incorporates the estimated deflection to develop a control architecture made of a sensor-based feedback channel, taking into account several factors such as hysteresis, drift, and non-linearity as exhibited by the sensor. The controller is then tested under the influence of ground effect. It was observed that the controller is able to compensate for the extra thrust generated due to the ground effect.

Acknowledgement

First and foremost, I would like to express my sincere gratitude to Prof. Gijs Krijnen for giving me the opportunity to be a part of the NIFTy group and introducing me to the fabulous world of 3D printing. Throughout this entire thesis, your guidance and feedback has helped me to a great extent. This work would have been a difficult task to accomplish if it wasn't for you.

I am extremely grateful to my daily supervisor Gerjan Wolterink for his valuable feedback and help while conducting experiments and 3D printing. His patience and calm personality enabled me to complete this assignment successfully.

I would also like to thank Antonio Franchi for sharing some knowledge in the field of controllers, which helped me to have an easy start for the second part of my assignment. Your immense knowledge has definitely helped me during this tough journey. Special thanks to Quentin Sable and Youssef Aboudorra , who helped me overcome some obstacles and making the time for feedback despite their busy schedule.

I am also thankful to dr. Leandro De Santana for graciously accepting to be a part of the examination committee.

Last but not the least, I am deeply grateful for all the love and support I received from my family. I am thankful to them for the sacrifices they made for my education and preparing me for the future.

Contents

1 Introduction

Additive manufacturing, best known from 3D printing, has become a common method for fabricating a wide range of components in industries [14]. By printing multiple layers of material, 3D physical objects can be created [15]. Compared to conventional manufacturing processes, additive manufacturing offers several other advantages such as the possibility of fabricating complex parts with ease and better topological optimisation. Recently, the advantages offered by additive manufacturing are attracting growing interest as this allows the possibility of embedding sensors into 3D printed structures for measurements in hard to reach points and without installing the sensors manually [16]. The use of such a process improves the integration of the sensor with the component/structure ensuring less material waste, minimal use of hazardous chemicals and fewer process steps [17] along with local fabrication and ease of testability.

Due to the rapid growth of the 3D printing technologies, it is now possible to use materials that are electrically conductive, allowing for realisation of objects with sensory characteristics [18,19]. By embedding 3D printed sensors into structures made using additive manufacturing, their functionality can be increased. This leads to more possibilities in terms of performance customisation, interfacing, and integration with shapes that are complex. Also, with no sensor assembly, the cost is reduced significantly [20]. Although 3D printing requires calibration and tuning of certain printing parameters to obtain the best printing quality, it offers the ultimate advantage of ease of accessibility and manufacturing of expensive parts that would otherwise be difficult with traditional methods. Furthermore, by embedding the sensors, the need for installation is eliminated along with various other errors that could potentially arise from it [3].

However, the method of printing embedded sensors using Fused Deposition Modeling (FDM) has certain limitations such as poor extrusion and inconsistencies [21]. Also, materials used in FDM suffer from non-linearities, hysteresis, and creep [20]. Another limitation is the repeatability of the printing process due to variations in raw materials and the printing process, as a result, the properties may vary between printed sensors. Also, integration of a sensor into any structure allows for the measurement of various parameters like pressure, applied force, and deformation due to the load. By analysing the effect of these parameters, the state of the structure can be determined under any load. In particular, a 3D printed strain gauge would serve this purpose, and measurement of strain allows for monitoring the system in both static and dynamic conditions as in the case of Unmanned Aerial Vehicles (UAVs) or Drones.

Unmanned Aerial Vehicles have seen immense growth in a wide range of applications like surveillance, inspection of buildings, land surveying, etc. On the other side, they have a higher accident rate due to various reasons like improper pilot training and inaccurate thrust estimation. Over the years, the number of cases of small UAVs crashing into public areas has increased considerably [22]. Hence, there is a need for improving flight stability which is highly dependent on accurate estimation of thrust produced by the propulsion system. As with most small multi-rotors, the thrust is usually estimated from either the motor velocity or the motor command. However, both of these techniques do not describe accurate thrust force under all flight conditions due to their feed-forward controller architecture [23]. Therefore, there is a need for an in-flight thrust measurement system that provides accurate measurements of thrust, thereby improving the robustness, stability, and safety of the aircraft to a great extent.

1.1 Motivation

Although strain gauges are known for their low cost and versatility, their application in the field of Unmanned Aerial Vehicles (UAVs) is missing. The inspiration behind this work arises from the interest to expand the applicability of strain gauges in the field of UAVs along with improved dynamic measurements while exploiting the advantages offered by 3D printing such as the use of

materials that are commercially available along with swift fabrication of relatively inexpensive structures/sensors. The work presented here has been performed with an effort to check/improve the measurement competence of UAVs by incorporating a 3D printed strain gauge. Furthermore, the use of 3D printed sensors for thrust estimation in drones has not been addressed in literature before.

1.2 Context

The objective here is to develop an in-flight thrust measurement system with the use of custom designed 3D printed strain sensors. Here, two materials, namely the electrially conducting PLA Proto-Pasta for strain gauges and the non-conductive material Polylactic Acid (PLA) are used in a single fabrication process. The thrust produced by the propeller causes the drone arm to flex and as a result, strain is induced on the drone arm, measured using the embedded 3D printed sensor. This strain is related to thrust by deducing a calibration equation. Using Finite Element Method (FEM) simulations, the stress-strain distribution on the drone arm is analysed to find an optimal position for placement of the strain gauge. A 13 inch propeller with a pitch of 4.5 is used in combination with an M3638 Mikrocopter motor and tested. Finally, an attempt is made to incorporate the estimated thrust and develop a control architecture based on a sensor-feedback channel that stabilises the drone in events of uneven airflow caused by random disturbances.

1.3 Project Goals

The impetus of this thesis is to realise a 3D printed strain sensor for in-flight thrust measurement in a drone, taking into account several factors such as hysteresis, drift, and non-linearity as exhibited by the sensor. Furthermore, the main goal is to improve the controllability of the lift-force by utilising FDM 3D-Printing to embed sensors on the drone arm and measure as accurately as possible.

The following questions are addressed:

- **Can the propeller thrust be measured indirectly by analysing the deflection of the drone arm or the propeller blades?**
- **Is a 3D printed strain gauge feasible for precise measurements of thrust?**
- **Can sensor behaviour such as non-linearity, drift, and hysteresis be compensated using differential measurements?**
- **Can a controller architecture be developed based on sensor feedback while nullifying the effects of hysteresis and non-linearity?**

1.4 Thesis Outline

This Chapter provides a brief introduction on 3D printing along with the motivation behind this work. Chapter 2 concerns a literature review outlining work done in the field of 3D printed sensors. This is followed by Chapter 3 which provides useful background information relevant to this work. Before finalising our approach to compute the thrust, it was important to look into various other scenarios. Chapter 4 describes these methods with a final comparison which serves as a solid motivation for our approach. The design and fabrication of the strain gauge and the drone arm are outlined in Chapter 5. Chapter 6 contains the complete testing procedure including the calibration of the sensor along with the results obtained from the tests. An overview of the control architecture developed and results for the same are presented in Chapter 7. Findings from this work are then discussed in Chapter 8. Finally, a conclusion is drawn in Chapter 9 .

2 Literature Review

Several publications have appeared in recent years pertaining to 3D printed sensors and in-flight thrust measurement system for aircrafts/drones. In this section, we review the literature outlining previous work that is relevant to this thesis with respect to the methodology, experimental results and accuracy of their design.

2.1 3D printed sensors

The feasibility of a 3D printed capacitive force sensor was investigated by Wolterink et. al [1]. The sensor fabrication as shown in Figure 2.1 consisted of two overlapping layers of conductive TPU along with a single layer of non-conductive TPU serving as an insulation material.

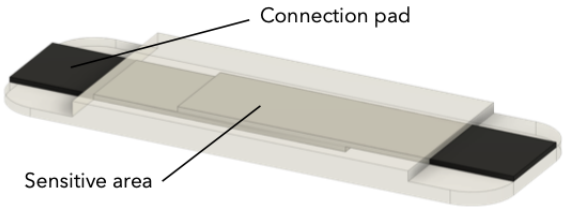

Figure 2.1: CAD drawing of the capacitive force sensor, Grey parts are dielectric while the conductive parts are denoted by black [1]

Force in the range of 0-10 N was applied on the sensor using a linear actuator and the measurements were read using an LCR meter. Results from the test indicated a good correlation between the measured displacement and capacitance. However, the TPU material did not return to its original shape, indicating the presence of creep. For forces between 0.2 N- 0.4 N, a large standard deviation is observed due to inaccuracies of the actuator. Moreover, the force-capacitance showed a non-linear behaviour due to the properties of the material used. Wolterink et. al further suggests that the accuracy of the sensor can be improved significantly by taking into account the influence of certain printing parameters like temperature and extrusion speed.

The work proposed by Dijkshoorn et. al [2] investigated the electrical properties of 3D printed conductors using characterisation techniques. Their design as shown in Figure 2.2 consisted of traxels that behave as conductors and were printed from carbon black-filled TPU.

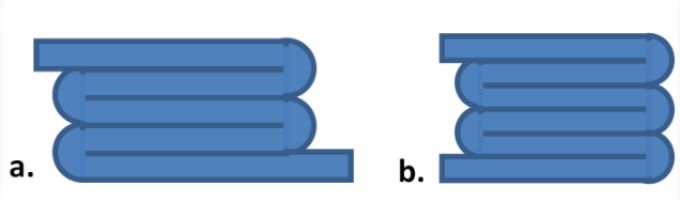

Figure 2.2: Two designs with (a) opposite leads and (b) leads on the same side [2]

The leads were made using copper tape with silver conductive paint. Using a gain-phase analyser, impedance measurements were taken from the sensor. FEM simulations were validated using a set of impedance measurements and heat distribution. A good agreement between FEM simulations and experiments was observed with gain phase measurements in the range of 1 kHz to 1 MHz. Also, power and temperature distribution along the traxels were similar when compared to results from FEM.

The possibility to integrate additive manufactures sensors in printed structures was also explored by Gooding et. al [3]. By embedding the sensors into the host structure, the need for manual installation of the sensor was completely eliminated. Gooding et. al investigated the effect of sensor geometry as well as different printer orientation for the 3D printed strain gauge. In their work, three different control factors were considered as shown in Figure 2.3 : the number of end loops on the strain grid, the width of each of the strands and the thickness of the strain gauge. The design of their strain gauge is shown in Figure 2.4.

		Levels			
Factors	ID	1	2	3	Units
Number of Loops	A	1	3	5	
Strand Width	B	1	1.5	2	mm
Gauge Thickness	C	0.2	0.4	0.6	mm

Figure 2.3: Control factor: No of end loops , Strand width and thickness of the gauge [3]

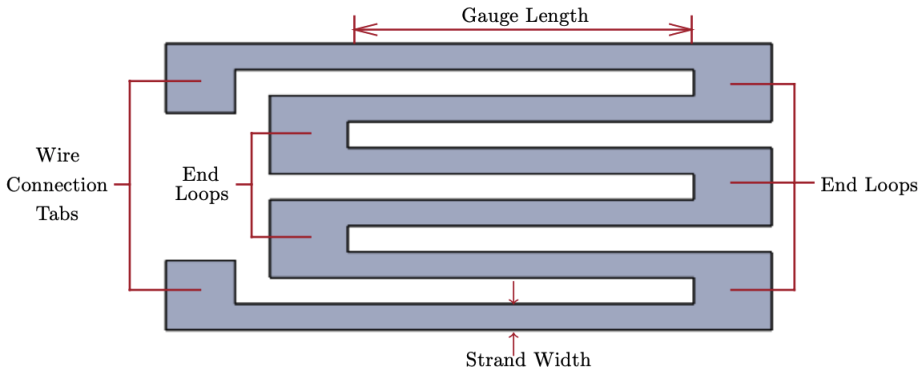

Figure 2.4: Design of the strain gauge [3]

A resistance of 2250 Ω was obtained using their 3D printed strain gauge. However, the estimated resistance from FEM simulation yielded a different resistance of about 2227 Ω. Gooding et. al attributes this to the inconsistent extrusion of 3D printing conductive materials. Results from tensile testing indicated that there was a decrease in hysteresis error with an increase in number of end loops on the printed strain gauge. Also, there was a noticeable increase in hysteresis with the increase in gauge thickness. Furthermore, different printing orientation can contribute to hysteresis errors. Specimens printed flat had the highest hysteresis error when compared to specimens printed with different orientations. Overall, the work of Gooding et. al summarises the influence of sensor geometry on performance and the importance of the same to design a perfect sensor although limited by extrusion inconsistencies.

As 3D printing opened new possibilities for printing sensors, dynamic measurements using 3D printed sensors were yet to be researched. A study published by Maurizi et. al [4] focused on dynamic measurements using an embedded conductive Polylactic Acid (PLA) based strain sensor taking into account the resistivity of conductive PLA, the effect of temperature and the dynamic range. The dynamic behavior of embedded 3D printed strain sensors was investigated on three different beam samples with Polylactic Acid (PLA) as the non-sensing material and conductive PLA or Protopasta for the sensing material. The samples are shown in Figure 2.5. Sample A had a total gauge length of 70 mm whereas the total length of sample B and C was 140 mm with the only difference between the two that sample C had an adjunctive sensor i.e. an additional sensor to check if noise can be compensated.

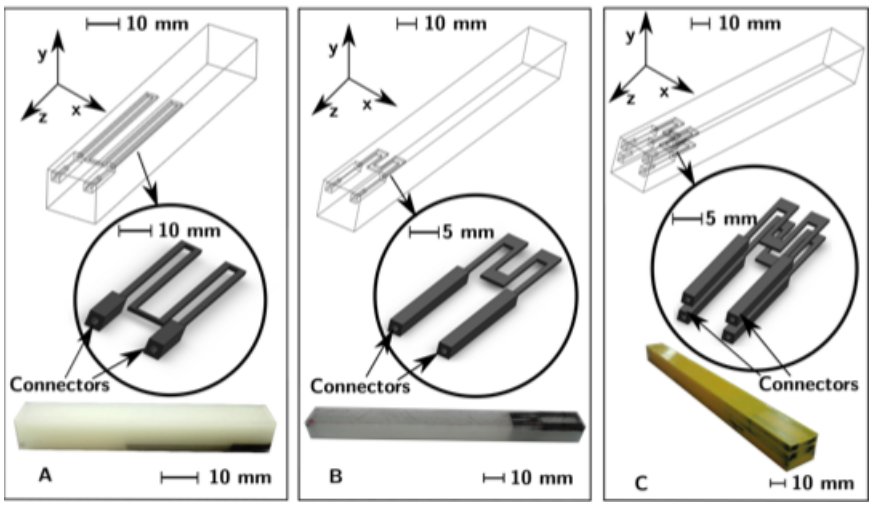

Figure 2.5: Geometry of Samples A,B and C. PLA is used for non-conductive part and Proto-Pasta for conductive [4]

Results from the test indicated different gauge factors of 3.2 , 1.71 and 1.77 for sample A, B and C respectively. Also, sample A exhibited more non-linearity than sample B and C. Although samples B and C in Figure 2.5 had the same geometry, their initial resistance was 16.41 kΩ and 16.45 kΩ respectively. Maurizi et. al attributes this to 3D printing uncertainty and different initial conditions for the test. Also, results from the experimental frequency response function (FRF) indicated that above 600 Hz, the sensor entered the non-linear region, thereby affecting the dynamics measurements at higher frequencies. The work of Maurizi et. al signifies mainly that sensor performance is affected by the choice of certain printing parameters.

2.2 In-flight thrust measurement system

With the increased use of Unmanned Aerial Vehicles (UAVs), there comes a need for improved performance in terms of utility and efficiency. With most performance evaluation methods, there is an extensive need for wind tunnel testing at various angles of attack and range of speed [24]. However, this is a time-consuming process. An in-flight thrust measurement system (IFTMS) proposed by Gong et. al [5] attempts to solve this issue by measuring the thrust directly during all possible flight conditions. The thrust measurement system as shown in Figure 2.6 makes use of a strain gauge fixed on mounting devices. Two mounting devices were considered, the hinge prototype and linear bearing prototype. By placing a series of known weights and recording the output voltage reading, the strain gauge was calibrated. Results indicated that better linearity was observed with the hinge prototype when compared to the linear bearing prototype. Based on this, a final hinge type thrust measurement system was designed.

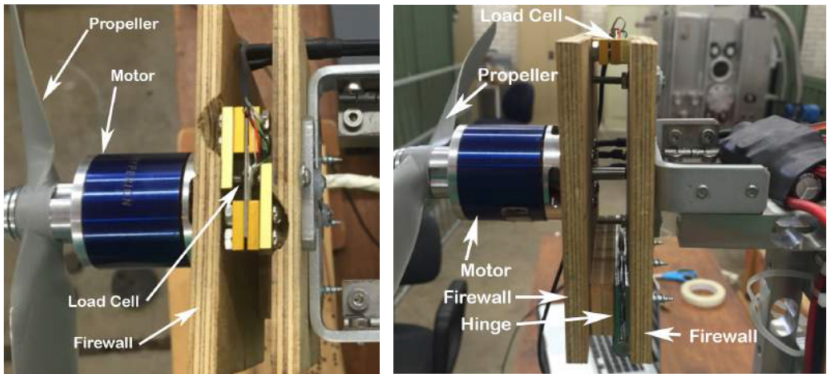

Figure 2.6: Thrust measurement system developed by Gong et. al [5]

To validate the IFTMS, a series of tests were conducted in a wind tunnel at different flying conditions and for a range of throttle settings. In a steady-level cruise, drag on the aircraft is equal to the thrust produced by the propulsion system. Thus, a measurement of thrust would give an estimate of the drag. A close correlation for drag was observed between the wind tunnel measurement and IFTMS. Tests conducted for steady-level flight conditions demonstrated that the estimated drag co-efficient correlates well with the drag co-efficient obtained using wind tunnel testing. Therefore, an in-flight thrust measurement system further enables a more accurate evaluation of the UAV performance in real flying conditions.

An attempt to individually control the thrust of the motor using integrated strain gauges was presented by Scholten [6]. Using integrated strain gauges on each of the drone arms, the goal was to measure the thrust of each motor individually and use in a feedback loop to achieve thrust control of the motors. The design of their multi-platform is shown in Figure 2.7.

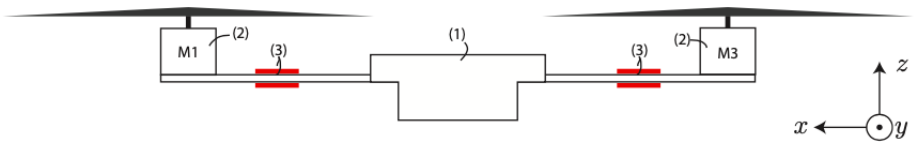

Figure 2.7: Cross-section of the multi-rotor platform: (1) - Electronics and Battery , (2) - Motor-propeller combination and (3) - Strain gauges to measure thrust [6]

Also, a F-T Sensor was used to validate measurements obtained with the conventional strain gauge. Results from their experiments showed that the vibrations induced on the drone arm caused an offset to occur on the F-T sensor. This was not the case for the strain gauge measurements whatsoever. Furthermore, the electrical connections were affected by the torsional vibration due to the motor. Overall, the results from the strain gauge and F-T sensor showed a good correlation. The influence of the ground and ceiling effect was also investigated and the same fluctuations were reflected in the strain gauge measurements.

Another approach proposed by Bazin [7] makes use of a quadcopter frame which was custom designed (Figure 2.8) to accommodate a full-bridge strain gauge assembly that is mounted to each of the quadcopter arms thereby enabling measurement of thrust and inertial forces.

Figure 2.8: Quadcopter frame mounted onto a test stand comprising of load cells [7]

From a series of tests performed, it was observed that there was a good agreement between the experimental strain gauge and conventional off the shelves load cell products. This strain gauge data was coupled to a motion capture system to create a dynamic model that calculated the thrust forces and inertial forces that are caused by translational and rotational acceleration. Their work demonstrated how monitoring the strain could help in high-speed maneuvres along with some important data regarding the condition of the UAV. Also, the developed thrust measurement system seemed to perform well at high oscillation frequency but the accuracy of the system was limited at low oscillation frequency due to the noise present in the data.

The use of a thin-foil strain gauge based thrust stand was also demonstrated by Marchman [8] where various motor propeller combinations were tested on a cantilever beam. The strain gauges were mounted on the beam in a full-bridge configuration as shown in Figure 2.9 where the beam flexed in response to the motor thrust. The thrust stand was tested in both static and dynamic conditions. Tests were conducted on five propellers of different sizes in combination with three brush-less direct current (BLDC) motors. It was found that a resolution of 0.01 N was obtained for thrust in the range of 0 -3 N. Also, the mounted strain gauges were able to detect vibrations produced by the motor but had to be sampled at a rate high enough to detect the vibration in the range of several hundred hertz.

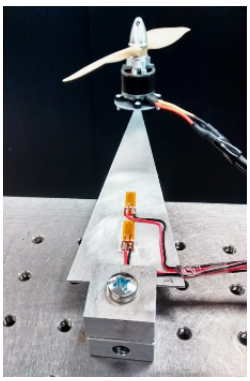

Figure 2.9: Cantilever Beam comprising of thin-foil gauges [8]

From the work of Marchman [8] and Stephen et. al [25], it was shown that a significantly smaller resolution can be obtained with thin-foil gauges. However, this may not be conventional in the area of 3D printing. In our application, we are limited to a minimum rotational frequency of 15 Hz which corresponds to approximately 0.3 N of thrust.

As seen from the above literature, a well-calibrated in-flight thrust measurement system (IFTMS) is capable of providing accurate measurements of performance determining characteristics like thrust and drag in different flying conditions. Also, in conventional load cell-based thrust mea-

surement systems, the measurement is limited to total thrust rather than individual thrust produced by each of the motor [26]. However, in this work, only thrust will be measured.

2.3 Conclusion

This thesis adds to the work done by previous authors by integrating a 3D printed strain gauge on the drone arm which serves as an in-flight thrust measurement system in real-time. However, the technique used in this thesis can be adapted based on user requirements i.e. the range of thrust sensing can be increased or decreased by varying certain parameters like thickness and length of the drone arm. This way, a large number of motor-propeller combinations can be tested in a short time due to the advantages offered by 3D printing.

3 Background

This chapter provides relevant background information to further the understanding of materials discussed in later chapters. The included topics are stress and strain, Fusion Deposition Modelling (FDM) and commonly used 3D printing materials. Also, the working principle of a strain gauge is discussed along with various factors that influence the design and performance of the gauge. Finally, the working of a electronic speed control and brushless dc motor is also discussed.

3.1 Stress and Strain

Stress (σ) is defined as the force that is exerted on an object per unit area, thereby causing deformation of the material. The unit of stress is N/m^2. Strain may be defined as the fractional change in length or the magnitude of deformation of a body due to an applied force [9].

$$\epsilon = \frac{\Delta L}{L} \tag{3.1}$$

Strain can be tensile (positive) or compressive (negative) depending on the direction of the applied load. Strain is a dimensionless quantity but sometimes expressed in units as mm/mm or inch/inch. As the magnitude of strain can be quite small, it is sometimes expressed as microstrain $\mu\epsilon$ [9]

In a uni-directional stress field, stress is proportional to strain with the condition that elastic limit of the material is not exceeded. The Young's Modulus E equals the slope of the stress-strain curve in the linear regime and indicates the material's resistance to deformation under the application of force [8]. In formula:

$$\sigma = \epsilon \cdot E \tag{3.2}$$

where σ is the stress, ϵ is the strain and E is the Young's modulus of the material.

3.2 Additive Manufacturing or 3D printing

With additive manufacturing or 3D printing, objects can be created by repeated addition of materials i.e layer by layer fabrication of 3D printed structures originates from a computer-aided drawing (CAD). Due to its innovative and versatile approach, it offers many possibilities in a variety of fields [27]. Using 3D printing technology, certain materials like conventional thermoplastics, ceramics, and graphene-based materials can now be printed. [28].

Due to the versatility of 3D printing, varieties of 3D printing technologies have been developed for different applications. 3D printing technologies have been cataloged into different groups such as binding jetting, material extrusion, sheet lamination, and energy deposition [29]. Only FDM will be discussed in this chapter as other 3D printing methods are beyond the scope of this paper.

3.2.1 Fusion Deposition Modelling (FDM)

The possibility of printing multi-materials and multi-colour printing is offered by material extrusion-based 3D printing technology [27]. 3D printing has been used widely due to its simplicity and low cost

Due to the relatively low cost and simplicity of this process, it has been widely used. An example of a material extrusion system is the Fused Deposition Modelling (FDM) which will be discussed in the following section.

Fusion Deposition Modelling or FDM is a 3D printing process where melted material is deposited layer by layer in a pre-determined path. The materials are thermoplastic polymers in the form of a filament. The thermoplastic filaments are pushed through into the nozzle, by the extruder and then deposited on a platform, mainly the heat bed [30,31]. By electronically slicing the 3D model in a CAD software, 2D curves are obtained. These curves define the area where the material is added layer by layer [32,33].

The benefits of Fusion Deposition Modelling are:

- Simplicity of the approach and cost-effective
- Practicality of FDM enables complex geometries to be fabricated [34]
- Suitable for rapid prototyping as most of the thermoplastic materials are widely available

Although FDM is a relatively simple process, it has certain limitations i.e. the structural properties of FDM printed parts are affected by the building orientation i.e. the direction in which the sample is built on the 3D printer. Also, FDM printed parts show anisotropic behaviour because of the dependence of mechanical properties on building orientation [35]

3.2.2 FDM Printing Materials

Using FDM technology, fully functional parts can be printed using a wide range of materials which include polymers, metals and ceramics, or a combination of these. However, with FDM, we are limited to thermoplastic polymers. Although there are many materials available for FDM, the choice of materials in this assignment is one of the existing material combinations, preferably Polylactic Acid (PLA) and a conductive PLA variant. Due to their low cost, weight, low melting point, and processing flexibility, polymers are being widely used for FDM [27].

Polylactic Acid (PLA)

Polylactic Acid or PLA is classified as a biodegradable thermoplastic that is derived from renewable resources namely corn starch, sugarcane, or tapioca roots [34]. PLA is often used in the form of filaments for 3D printing and is preferred due to its high mechanical resistance, rigidity, and ease of use [36]. Also, due to its lower printing temperature, PLA is easier to print with and suited for parts where aesthetics are important.

Conductive PLA

Conductive PLA is a compound of 4043D PLA mixed with conductive carbon black [4]. Due to similar printing temperatures like PLA, it can be printed in the same cycle.

Nylon

Another commonly used material in 3D printing is Nylon. Parts printed from Nylon exhibit low creep and high impact strength along with good resilience. At higher printing temperatures, better mechanical properties can be achieved. This is attributed to strong bond formation between layers at high temperatures [37]. However, due to its hydrophilic nature, the mechanical properties of printed parts are affected in the presence of moisture [38]

ABS Plastic

ABS or Acrylonitrile Butadiene Styrene is another filament used in FDM. The strength of ABS printed parts depends on the nozzle diameter. An increased nozzle diameter enhances the strength of parts, which in turn impacts the tensile strength of ABS printed parts [39–41]. Also, when printing with ABS, there are several important printing parameters that must be taken into consideration: Printing layer thickness, infill density, orientation, and air gaps. These parameters provide better strength to printed parts [42, 43].

3.3 Strain Gauge

A commonly used method of strain measurement is the use of a strain gauge. The resistance of a strain gauge varies proportionally to the amount of strain on the structure. While there are several strain gauge patterns to sense strain in different directions, the majority of the commercial strain gauges are designed in such a way that unidirectional deformation can be sensed. Also, the positioning of the strain gauge on the test specimen is important to measure the strain accurately. A significant parameter of the strain gauge is its gauge factor (GF) which determines its sensitivity to strain and is defined as the ratio of fractional change in resistance to fractional change in length, i.e. strain [9].

$$\text{Gauge Factor(GF)} = \frac{\Delta R/R}{\epsilon} \tag{3.3}$$

If the resistivity of the material and geometry of the strain gauge is known, the resistance of a strain gauge can be calculated as:

$$R = \frac{\rho L}{A} \tag{3.4}$$

where the resistivity of the material is given by ρ, L is the gauge length and A is the cross-sectional area of the strain gauge characterised by the width and thickness of the strand.

The working principle of a strain gauge is straight forward. When an external force is applied on a material, the material deforms, and the electrical resistance of the material changes. In the ideal case this change in the electrical resistance of the material is directly proportional to the strain. Strain gauges are often used in Wheatstone bridge configurations (Quarter, Half, Full) along with an excitation source (current or voltage). A typical Wheatstone bridge configuration is shown in Figure 3.1.

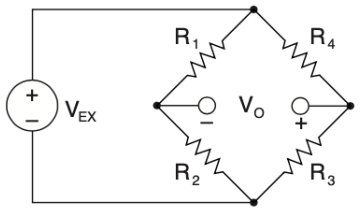

Figure 3.1: Wheatstone bridge [9]

Here, V_o is the output voltage of the bridge given by:

$$V_o = \left[\frac{R_3}{R_3 + R_4} - \frac{R_2}{R_1 + R_2} \right] \cdot V_s \tag{3.5}$$

From the above eq. 3.5, it is obvious that the output voltage is zero when the bridge is said to be balanced or when $\frac{R_1}{R_2} = \frac{R_4}{R_3}$. In other words, any small change in resistance in the bridge will result in a non-zero output voltage V_o.

Different Wheatstone bridge configurations:

- **Quarter Bridge Circuit**

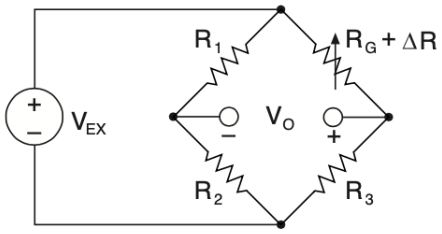

Figure 3.2: Quarter bridge circuit [9]

In the case of a quarter bridge circuit as shown in Figure 3.2, one of the resistors is replaced with a strain gauge, while other resistors serve as fixed resistors. Therefore, any change in resistance of the strain gauge will cause the bridge to unbalance with a non-zero output. Then, the bridge output can be written as a function of strain and gauge factor [9]:

$$\frac{V_o}{V_{EX}} = \frac{\text{-GF} \cdot \epsilon}{4} \left[\frac{1}{1 + \text{GF} \cdot \frac{\epsilon}{2}} \right] \tag{3.6}$$

The above Equation 3.6 is true when the value of the resistors is same $R_1 = R_2 = R_3 = R_G$.

- **Half Bridge Circuit**

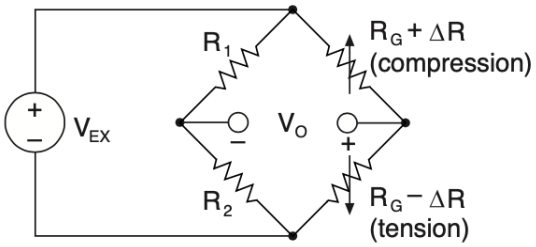

Figure 3.3: Half bridge circuit [9]

As for a half-bridge circuit in Figure 3.3, two fixed resistors are replaced by strain gauges. This way the sensitivity of the bridge is also doubled. With the use of two gauges, the effect of temperature is minimised. Any temperature change will affect both the gauges uniformly. Hence, due to identical temperature changes, the resistance ratio of the gauge does not change and neither the output voltage. This way temperature effects are minimised. The output voltage of such a configuration is given by [9]:

$$\frac{V_o}{V_{EX}} = \frac{\text{-GF} \cdot \epsilon}{2} \tag{3.7}$$

- **Full Bridge Circuit**

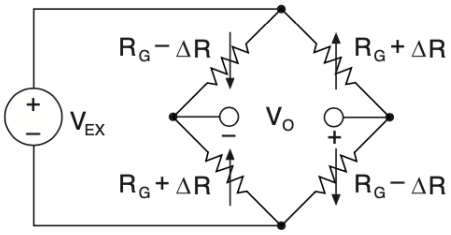

Figure 3.4: Full bridge circuit [9]

The sensitivity of the circuit can further be increased with the help of a full-bridge configuration shown in Figure 3.4 where all fixed resistors are replaced with strain gauges [9]. Furthermore, the use of a full-bridge allows for measurements of small changes in strain along with improvement in signal to noise ratio [8]. The output of a full-bridge configuration is given by [9]:

$$\frac{V_o}{V_{EX}} = \text{-GF} \cdot \epsilon \tag{3.8}$$

3.3.1 Selection of a Strain Gauge

To achieve accurate measurements, there are certain parameters that affect the operating characteristics of a strain gauge [10]:

- **Gauge Length:** The strain sensitive length of the grid is termed Gauge length (Figure 3.5). The end-loops and solder tabs are relative insensitive to strain because of the large cross-section. The gauge length is one of the important factors that determines the performance. Larger strain gauges offer the advantage of improved heat dissipation and the importance of this can be seen when the gauge is installed on materials like plastic which have poor dissipation [10]

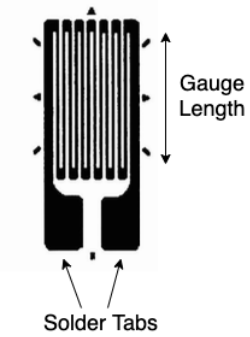

Figure 3.5: Gauge length [10]

- **Gauge Pattern**: There must be some knowledge of the structure's response to load for effective use of the strain gauge. In order to position the strain gauge on a structure, it is important to know the actual strain distribution and nature of stress to determine what gauge pattern would be suitable for the application. A single grid pattern strain gauge would only be able to measure strain in one direction in the non-linear regime. However in the linear regime, the gauge factor can still be used when the gauge is subjected to compressive stress. To measure bi-axial strain, a 2 or 3 element rosette is required.

When the direction of stress/ strain is known, a 2-element 90-degree rosette is ideal [10]. However, in our application, we measure strain in only one direction.

- **Grid Resistance**: In the above gauge patterns, the only difference is the resistance of the grid. Based on the application, a higher resistance strain gauge can reduce heat generation to a great extent for the same applied voltage. Using a higher gauge resistance decreases lead wire effects such as random signal variations caused by change in resistance of the lead wire due to fluctuations in the temperature. Also, with the use of a high gauge resistance in circuits with slip rings and switches, the signal to noise ratio is improved to a great extent [10].

- **Self-Temperature Compensation:** As with all electrical conductors, the resistivity changes with temperature. This phenomenon is referred to the TCR or Temperature co-efficient of resistivity. This co-efficient represents the possible error in strain gauge measurements induced by temperature variations. Therefore, it is important to deal with these errors to obtain accurate measurements of strain. The first method involves recording the strain output and temperature of the gauge simultaneously with time. However, this method of error correction is enduring as it requires two data channels. The second method involves the use of a compensating strain gauge (Dummy strain gauge) in the bridge circuit. By placing the compensating gauge beside the active gauge, the two gauges experience the same temperature change. As a result, the two gauges will experience the same change in resistance due to temperature change and will be cancelled in the bridge circuit. While this method compensates for the temperature change, installation of the dummy gauge is a challenge as it requires the dummy gauge to be at the same temperature as that of the active gauge [10]. In this work, instead, a simple voltage divider circuit will be used individually for the two sensors.

Overall, the strain gauge is only a part of the measuring system. It is important to design a strain gauge as per the requirements. Therefore, to obtain accurate measurements of small fluctuations in voltage, a sensitive strain gauge is necessary. Although a perfect strain gauge can still be designed, it is the limitation of 3D printing that can affect the quality, accuracy, and repeatability of printed gauges due to probable inconsistencies in extrusion and other printing parameters. Additional errors may be induced by nonlinear response of the resistive material.

3.4 Electronic Speed Control (ESC)

ESC or Electronic Speed Control provides an AC signal to the BLDC motor, which in turn causes it to rotate. The two out of the three wires leading to the motor are energised by the ESC. The third wire generates the required voltage corresponding to the speed, as the motor spins.

Using a PPM (pulse position modulation) signal, the speed of the BLDC motor can be controlled, similar to a PWM signal (Pulse Width Modulation). Information is conveyed by PWM signals by changing the duty cycle of the pulse. However, in the case of PPM, the time between the fixed-width pulses is adjusted [8]

3.5 Brushless Direct Current Motor (BLDC)

A brushless direct current motor has a permanent magnet rotor along with stator coils, unlike brushed motors which are the opposite. Also, a Brushless motor proves to be more superior to brushed motors. Unlike brushed motors where the brushes wear out over time and are noisy, a brushless motor does not face these problems. Their low weight makes them more efficient. Also, brushed motors have a constant torque profile, making them suitable for smaller UAVs. However, the major disadvantage of a brushless motor is the high price and use of complex control electronics.

An important specification of the brushless motor is its K_v rating which defines the RPM for every volt. A motor with a high K_v rating has a low torque profile and high speed while a low K_v equates to high torque and low speed.

A brushless motor with a K_v rating of 1000 when used with a 11.1 V battery would give a max RPM of 11 100 RPM at no load condition [8].

3.6 Conclusion

The theory behind stress and strain was discussed, followed by fusion deposition modelling and commonly used FDM printing materials. The geometry of the strain gauge, different wheatstone configurations and the influence of certain parameters such as gauge length , grid resistance and gauge pattern was also addressed. This was followed by a brief description about the electronic speed control and brush-less DC motor.

4 Scenarios

In this chapter, two scenarios are discussed: Blade Flapping and Drone Arm Deflection. These methods are analysed to check if thrust can be measured indirectly by mounting a strain gauge. There are several parameters that are taken into account; magnitude of the two phenomena, sensing principle, and effect of the same on the weight of the drone and so on. Their advantages and drawbacks are discussed and finally, a choice of method is made based on a final comparison between the two.

4.1 Blade Flapping

Although blade flapping is usually seen in large rotor-crafts like helicopters, it does occur in small rotor-crafts like UAVs. The phenomenon of blade flapping occurs in forward flight condition due to the asymmetric lift generated by the advancing and retreating sides of a blade [44] i.e. a difference in lift between the advancing and retreating blades causes the rotor tip path plane to tilt. The phenomenon of blade flapping is shown in Figure 4.1.

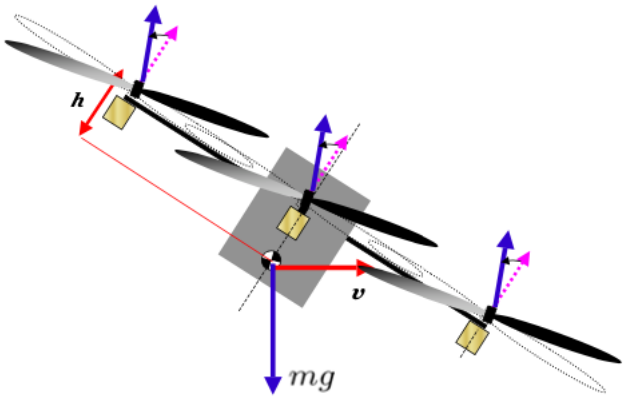

Figure 4.1: Blade Flapping as seen in forward flight: Deflection of the thrust vector is seen as a result of deflection of the rotor plane due to flapping [11]

The blade is said to be advancing if $0° < \psi < 180°$ and retreating if $180° < \psi < 360°$, where ψ' is the azimuth angle of the blade on the rotor disc as described in Figure 4.2 [45]. The azimuth angle ψ is defined as the angle measured in the direction of the rotating blade from the downstream to the axis of the blade span [12].

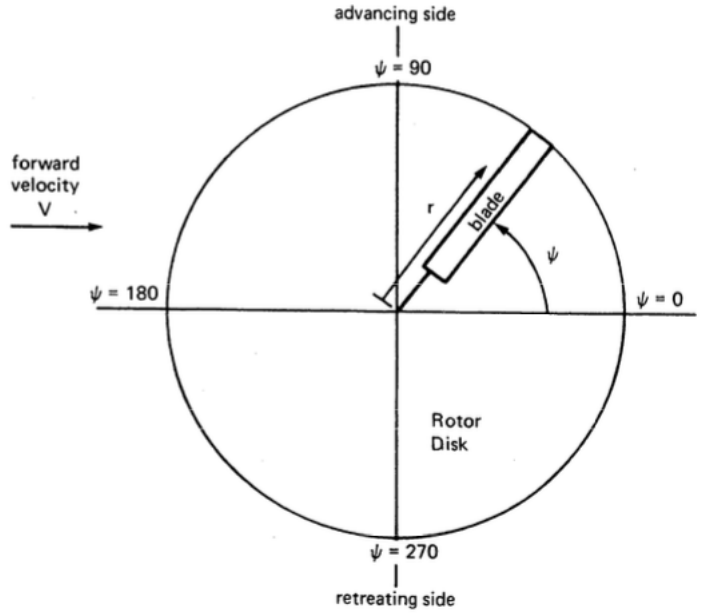

Figure 4.2: Rotor Disk depicting the rotation of advancing and retreating blades using azimuth angle ψ [12]

The rotor tip path plane is referred to as the axis of zero flapping or the plane where the rotor disc does not tilt. Due to the blade rotation, the rotor tip path plane tilts backward and sideways, causing the rotor tip path plane to move at an angle called the Blade Flapping angle, denoted by the angle β [46].

Much of the aerodynamic force approximation methods are based on the Blade Element Theory (BET), which is a quasi-steady analysis where the effects of blade flapping are not considered. The inclusion of blade flapping can help significantly in obtaining an accurate approximation of aerodynamic moments and forces [44].

4.1.1 Mathematical Model

Before presenting the blade flapping model, some non-dimensional variables have been defined. If N_b - number of rotor blades, R - Radius of the blade, I_b - Mass moment of inertia of the rotor blades and c - chord length, then [46]:

- **Lock number** : Lock number may be defined as the ratio of aerodynamics forces on the blade to inertial forces on the blade [47].

$$\gamma = \frac{\rho A c R^2}{I_b} \tag{4.1}$$

  and A is the slope of 2D airfoil lift curve.

- **Co-efficient of Thrust** :

$$C_t = \frac{T}{\omega^2} \tag{4.2}$$

  where T is the thrust and ω is the angular velocity

- **Rotor inflow ratio** λ [48] :

$$\lambda = \sqrt{C_t/2} \tag{4.3}$$

  where C_t is the co-efficient of thrust.

- **Pitch angle** θ_0:-

$$\theta = tan^{-1}(\frac{p}{2\pi R}) \tag{4.4}$$

  where p is the pitch of the blade

A few assumptions have been made while modelling the blade flapping angle:

- The UAV is operating at steady-state flight condition
- Motion of the blade is periodic
- The propeller is assumed to be cylindrical while calculating the moment of inertia

In a steady forward flight condition, the forced motion of the blade corresponds to a given pitch angle θ_0, advance ratio μ, and inflow ratio λ. Following the assumption that the forced motion of the blade is periodic, it can be expressed in harmonic terms as [45]:

$$\beta(\psi) = a_0 - a_1 cos\psi - b_1 sin\psi \tag{4.5}$$

where $\beta(\psi)$ is the blade flapping angle and a_0, a_1 and b_1 are the flapping co-efficients.

In the above Equation 4.4, only harmonics of the first order have been considered as the effect of higher-order harmonics is quite negligible in the case of small rotor-crafts like UAVs [46]. The flapping coefficients are defined by [45]:

$$a_0 = \frac{\gamma}{8}(\theta_0(1+\mu^2) - \frac{4}{3}\lambda) \tag{4.6}$$

$$a_1 = 2\mu(4\theta_0/3 - \lambda) \tag{4.7}$$

$$b_1 = \frac{4}{3}\mu a_0 \tag{4.8}$$

where a_0 is the coning angle defined as the upward angle formed by the blades due to the thrust produced. that is relatively small due to the rigidity and stiffness of the rotor blades. a_1 and b_1 are backward and sideways tilting of the rotor tip path plane and θ_0 is the pitch angle.

Results

The above blade flapping model for an 8x4.5 inch propeller was implemented in Matlab. The value of C_t at a specific advance ratio was obtained from the APC database [49]. The chord length c of the propeller was assumed to be at 3/4 radius [45]. While defining the Lock number, the value of 2D lift curve slope of 0.083 was obtained using XFOIL (XFOIL, USA) with a plot of co-efficient of lift at a certain angle of attack for a NACA 4412 airfoil which is a basis for modern propeller shape [49].

A graph of blade deflection (°) vs azimuth angle (ψ) was plotted to check the magnitude of blade deflection at different advance ratio μ and are represented in the Figure 4.3 below:

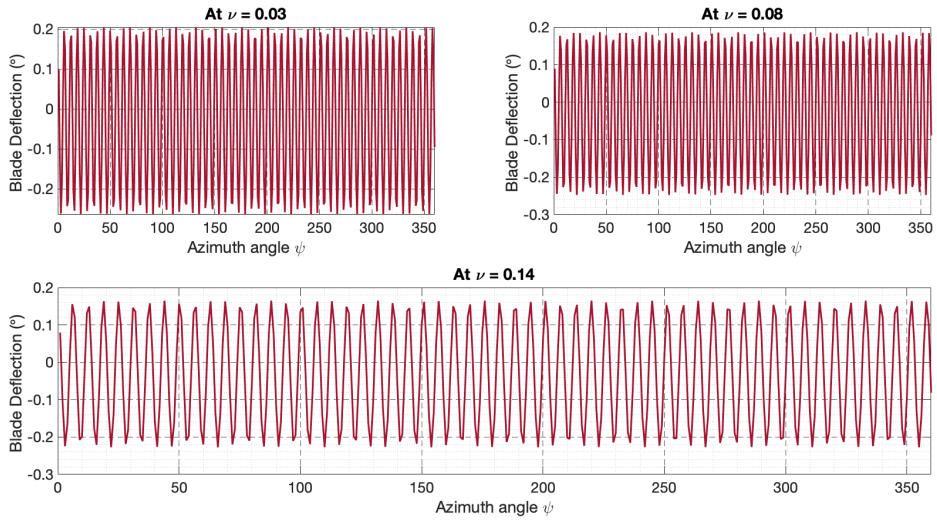

Figure 4.3: Blade Deflection at different advance ratios μ= 0.03, 0.08 and 0.14: With increase in advance ratio, the magnitude of blade deflection decreases.

As seen from Figure 4.3, the dynamics of blade flapping is quite fast and occurs for every azimuth angle and for every revolution of the rotor blades. The influence of advance ratio on blade deflection is quite significant i.e. at a higher advance ratio, the blade deflection decreases. With increasing advance ratio, there is a significant decrease in the co-efficient of thrust. This trend can be explained using the momentum theory developed by Rankine where the thrust is calculated using the following equation:

$$T = m(v_i - v_a) \tag{4.9}$$

where 'T' is the thrust, 'm' is the mass of the fluid,'v_i' and 'v_a' are the incoming and accelerated velocity respectively.

From equation 4.9, it can be seen that any difference in velocity can affect the magnitude of thrust to a great extent. As with increasing advance ratio (μ), the decrease in thrust is attributed to the increasing axial velocity i.e. the difference in velocity is lower at increasing advance ratio. In other words, the fluid medium surrounding the propeller is already moving at high velocity and the propeller hardly makes any changes to the accelerated velocity v_a. Therefore, the difference in velocity is smaller and hence the thrust [50]. As a result of which, the magnitude of the aerodynamic force on the blade is quite small and hence a smaller deflection is observed at a higher advance ratio.

4.1.2 Blade Deflection Simulation using Finite Element Analysis

Using ANSYS (ANSYS Inc, USA), structural analysis was carried out on an 8 inch propeller with a pitch of 4.5, to investigate the effect of blade deflection under varying load. In order to facilitate faster computation, only one section of the blade was analysed. Two common materials were used for the propeller: ABS Plastic and Nylon 6-6. The only point of interest in this simulation is the tip of the blade as the deflection would be the highest at these points [48].

The geometry of the propeller is shown in Figure 4.4. The model was meshed with an element size of 50 mm with 1639 nodes and 699 elements as smaller element size distorted the propeller geometry.

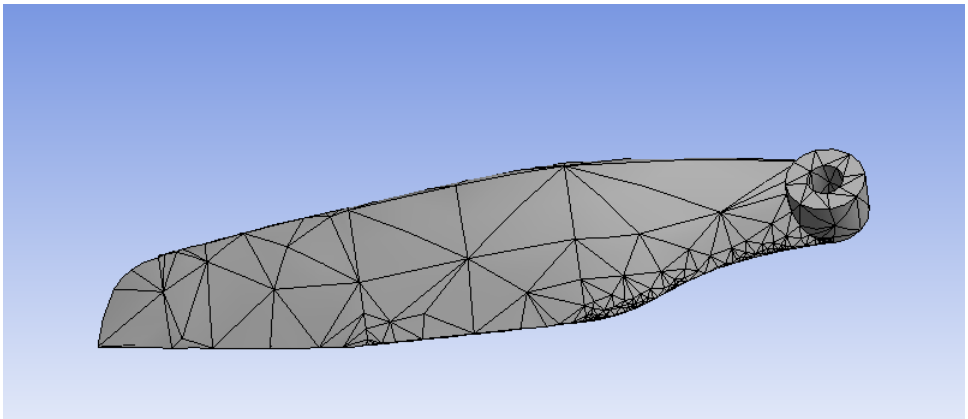

Figure 4.4: 8x4.5 propeller

As for the boundary conditions, three loads were applied to the propeller blade:- Inertial forces, Gravitational force and lift. Lift force was modelled as a load on the bottom surface of the blade where the value of lift force was referred from the APC Database [49]. Standard gravity could be applied by default on ANSYS along with rotational velocity that makes up for the inertial forces. Also, the hub of the propeller was constrained at the bottom and along the axis of rotation.

Results

Results obtained from ANSYS are shown in Figures 4.5 – 4.7, where deformation and strain on the propeller were analysed at 8000 RPM and advance ratio of 0.03 for Nylon 6 material:

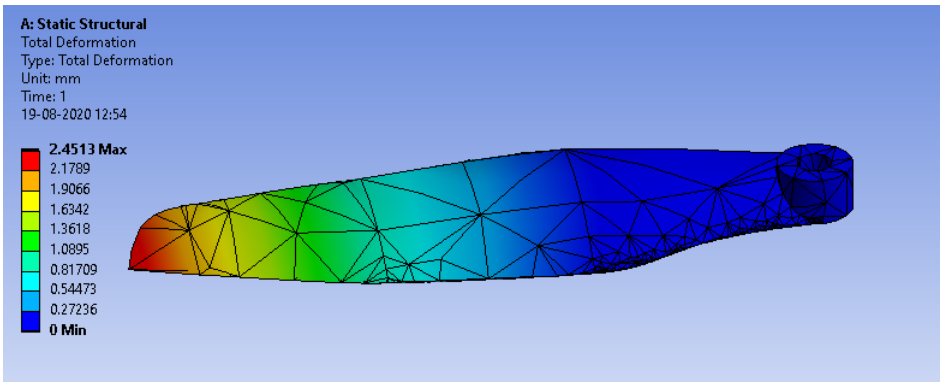

Figure 4.5: Deformation

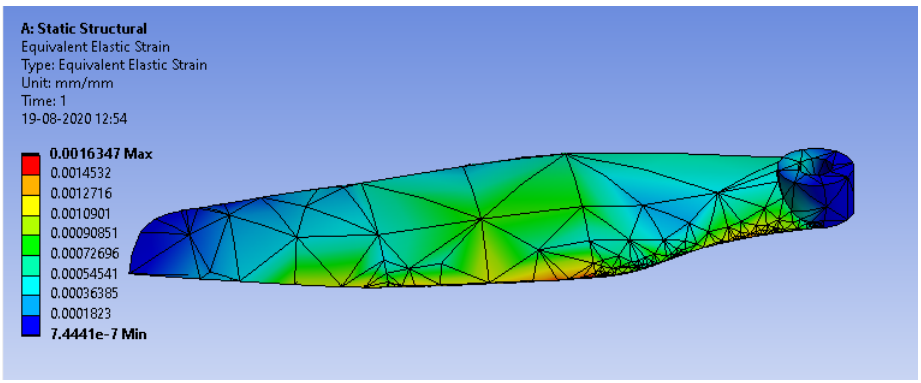

Figure 4.6: Strain

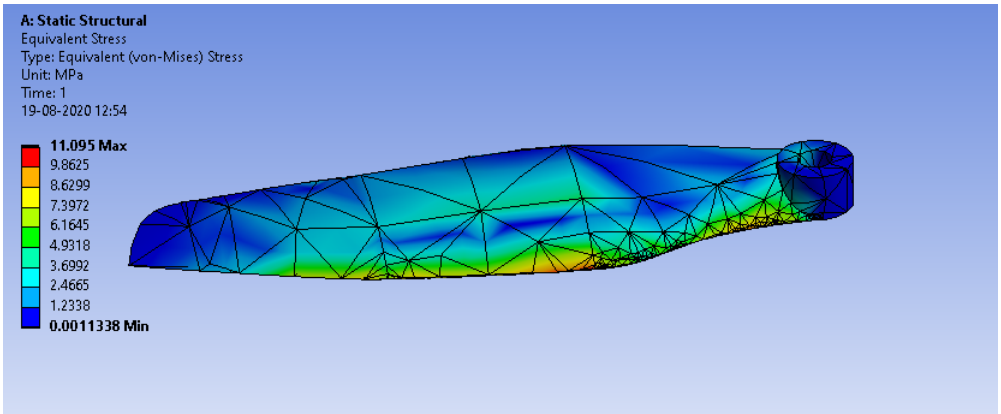

Figure 4.7: Stress

As seen from Figure 4.5, the deflection at the tip is about 2.4 mm and the magnitude of strain is quite small of the order 1600 $\mu\epsilon$. Also, stress is within the elastic limit of the material. Similarly, the propeller was analysed with ABS Plastic as the material and the deformation and strain were 4.6 mm and 2960 $\mu\epsilon$ which is almost double that of Nylon. It is quite obvious that with increased thrust, strain, and deflection at the tip would be much higher and vice versa. Moreover, with the use of a stiff material like Nylon, the effect of blade flapping/deflection is reduced drastically and such a small deflection (2.4 mm - 4.6 mm) of the blade tip may be ignored.

4.1.3 Vibration Analysis

Due to the fast dynamics of the blades, the propellers may undergo vibrational excitation. Vibrations may be induced on a propeller blade in different ways, as reported by Lieber [51]. Unstable vibrations can occur at critical speed due to the absorption of energy from the air and these vibrations may result in fracture when certain amplitudes are reached. Another important cause of vibration is due to unequal impact of the blades because of uneven airflow. This way, for every revolution, the propeller stress varies and may produce resonance vibrations. Therefore, it is important to investigate this resonance vibration before implementing a sensor on it to obtain intelligible results of blade deflections.

Modal Analysis

Vibrational excitation induced on the propeller can translate to a sensor mounted on the propeller irrespective of the sensing principle used. Dynamic excitation like this can be measured with the help of modal analysis. Using modal analysis, different mode shapes and natural frequencies of a structure can be determined. The natural frequency is the lowest frequency at which the system may tend to vibrate. The mode shapes describe the configurations into which a propeller may naturally displace under no load and each of the mode shapes corresponds to a specific natural frequency. Although a structure can have an infinite number of mode shapes, only three mode shapes will be considered for our analysis as higher-order mode shapes do not necessarily correspond to displacement patterns that could be seen in the case of blade flapping.

Modal analysis was performed on an 8x4.5 inch propeller to investigate the effect of material properties on the natural frequency of the propeller. Three different materials were considered namely: Nylon 6-6, ABS Plastic, and Polylactic Acid (PLA). Results from the modal analysis are shown in Figures 4.8 – 4.10 for Nylon 6-6 Material:

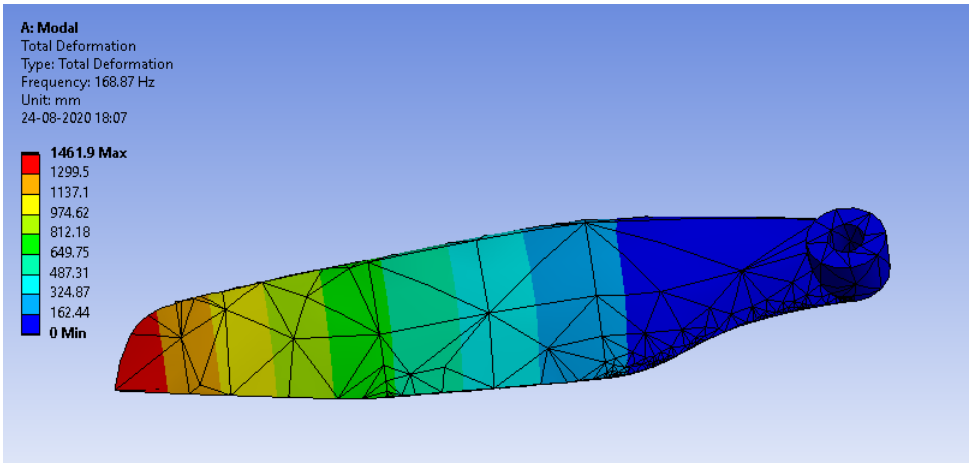

Figure 4.8: First mode shape

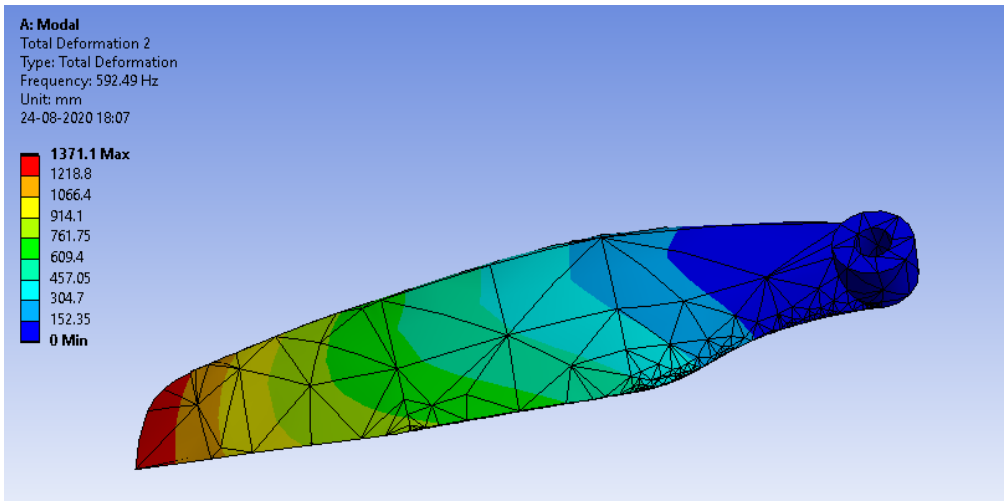

Figure 4.9: Second mode shape

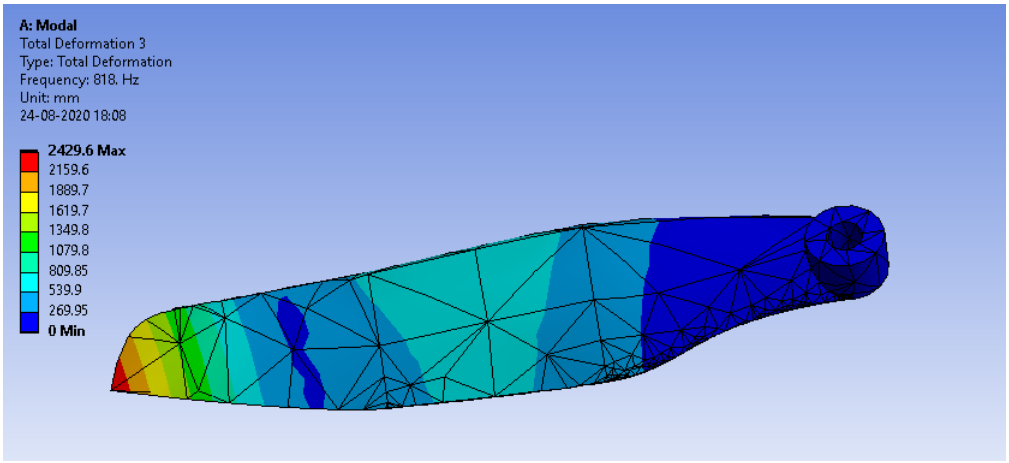

Figure 4.10: Third mode shape

As seen in Figures 4.8 – 4.10, different mode shapes correspond to different natural frequencies. The results from Figure 4.9 and Figure 4.10 show displacement patterns which are not relevant to our application of blade flapping. Only the first mode shape in figure 4.8 is of interest as it

clearly depicts the deflection of blades in the vertical direction as in the case of blade flapping. This mode shape has a natural frequency of 168.87 Hz.

When the rotational frequency approaches this natural frequency, resonance occurs or the object begins to resonate and this increases the system vibration. This condition of resonance occurs at a critical speed i.e. when the rotational speed equals this value of natural frequency, causing significant vibration on the propeller at 168.87 Hz which corresponds to approximately 10 132 RPM. However, the propeller is able to reach higher RPM depending on the motor chosen. Therefore, at 10132 RPM, resonance would the highest and can affect sensor readings significantly by adding noise to measurements due to the vibrations induced on the drone arm. However, the magnitude of vibrations would eventually above the natural frequency/resonance frequency.

The magnitude of natural frequency depends mainly on the geometry of the structure and the material properties. To validate this, modal analysis was performed on two other materials, PLA, and ABS Plastic. The results from the analysis are presented below in Table 4.1 comparison with the results obtained for Nylon 6-6.

Mode	ABS	PLA	Nylon 6-6
Mode 1 (Hz)	101.78	111.51	168.87
Mode 2 (Hz)	337.96	370.69	592.49
Mode 3 (Hz)	459.98	504.11	818

Table 4.1: Natural frequency for different materials

As seen from the above results in Table 4.1, the natural frequency depends on the material properties as well. Irrespective of the material used and its elastic properties, resonance occurs in the propeller. As modal analysis only accounts for free vibrations on the structure, it can be estimated that in reality, the vibration amplitude at the natural frequency of the propeller may be much larger in the presence of forced vibrations that may be induced by the aerodynamic forces acting on the propeller at a specific velocity and RPM. This vibration on the propeller can significantly change the angle of attack, causing a torsional moment [51], which wouldn't be ideal if a strain gauge were to be mounted close to the hub. The only way to nullify the effect of resonance is to run the propeller below the natural frequency. This would mean that the propeller performance is restricted to a great extent.

Hence, this method of analysing the thrust using strain pattern on the propeller is not technically feasible due to the vibrations induced on the propeller along with the added weight of the sensing principle and magnitude of blade flapping. From the mathematical model and FEM simulations, it can be observed that the magnitude of blade flapping is quite small (2.4 mm - 4.6 mm) and the effect it has on thrust is minimal as a small deflection of the blades only decreases the rotor disc area by a small amount and may be deemed negligible. Hence, another method is analysed in the next section.

4.2 Deflection Of The Drone Arm

Another potential way of computing the thrust of the propeller is by measuring the deformation of the Drone arm. The thrust produced by the motor propeller combination causes the drone arm to flex, thus inducing a strain on the fixed end of the arm. This strain is measured using a strain gauge embedded on the drone arm. The strain gauge is calibrated by applying a known load and an equation for thrust is deduced based on the force-strain relationship.

4.2.1 Finite Element Method Simulation

A CAD model of a drone arm was created in Fusion 360 (Autodesk, USA) and further analysed using ANSYS (ANSYS Inc., USA) to estimate the magnitude of deformation, the induced stress, and strain caused by the thrust produced by the propeller. A free-body diagram of the system

is shown in Figure 4.11 where propeller thrust causes the drone arm to displace, thus inducing strain closest to the fixed support. As the drone arm will be 3D printed, three different materials were considered for the simulation: Polylactic acid (PLA), Nylon 6, and ABS plastic.

Figure 4.11: Free-body diagram of the drone arm due to the thrust produced by the propeller.

Drone Arm

The drone arm as shown in Figure 4.12 was meshed with element size of 2 mm with 16.5k nodes and 68.5k elements.

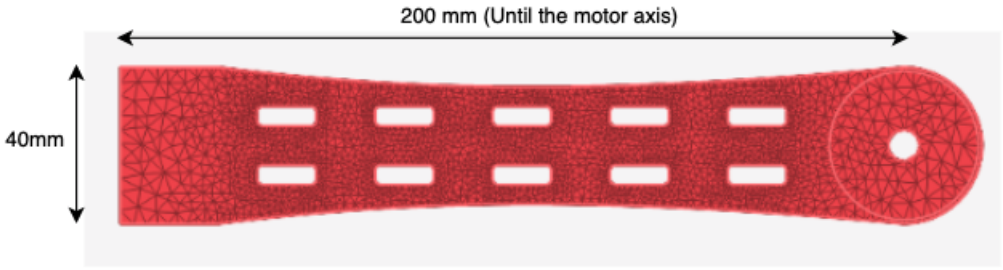

Figure 4.12: Meshed drone arm

The following boundary conditions were applied to the drone arm in Figure 4.13:

- Fixed support (To replicate fixture on the frame)
- Force at the free end of the drone arm (Thrust produced by the propeller)
- Standard earth gravity of 9.81 m/s^2

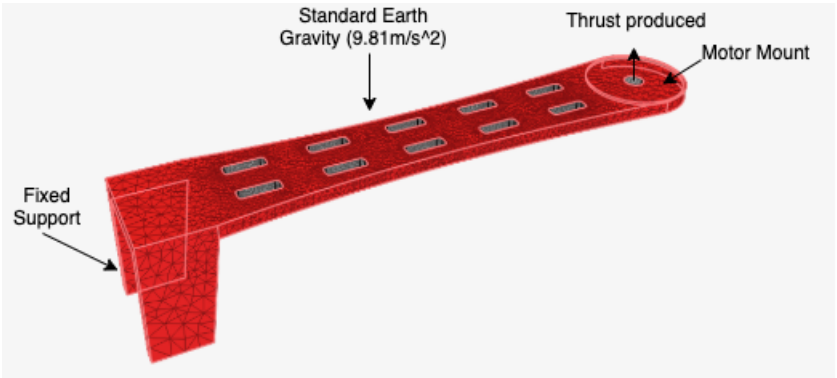

Figure 4.13: Applied boundary conditions on the drone arm

4.2.2 Material Choice

The design is analysed for three different materials: PLA, Nylon 6, and ABS plastic. Finally, a comparison is made between the three along with a final choice for the design.

Material Properties

The material properties for PLA , ABS Plastic and Nylon 6 are listed below in Table 4.2:

	PLA	ABS Plastic	Nylon 6
Young's Modulus (MPa)	3450	2390	1060
Poisson's Ratio	0.39	0.399	0.35
Ultimate Tensile Strength (MPa)	59.2	44.3	49.7
Tensile Yield Strength (MPa)	54.1	41.4	43.1

Table 4.2: Material properties (ANSYS Inc, USA)

Results

The design was simulated at 10 N with different materials to investigate the influence of material properties on deflection, strain, and stress. Results from the static structural analysis are shown below in Figure 4.14

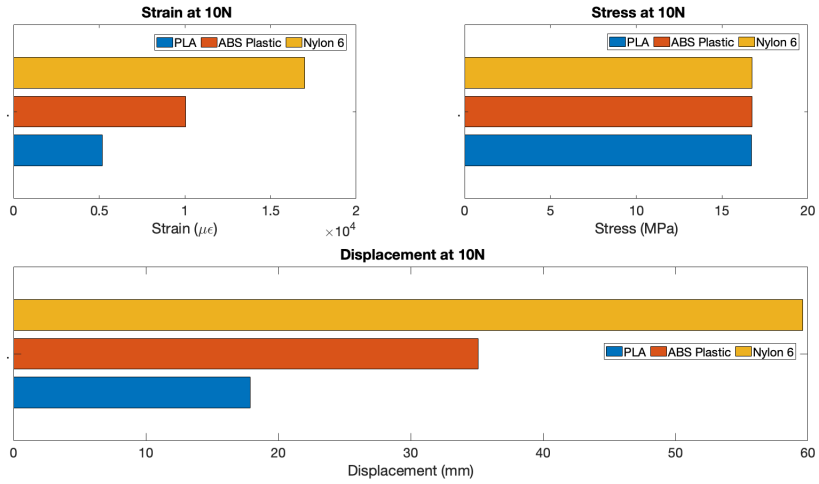

Figure 4.14: Effect of material properties on displacement and induced stress, strain on the drone arm

From the results in Figure 4.14, it can be seen that the deformation and strain characteristics vary between the three materials. It is also interesting to see that the induced stress is similar amongst the three materials. Stress is well within the limit for all materials, indicating that the design is safe irrespective of the material used.

With respect to the influence of material properties, small deflection and strain are obtained with PLA and ABS but the deflection and strain are the highest with the use of Nylon. Also from Table 4.2, it can be seen that the ultimate strength and tensile strength of PLA is much higher than Nylon and ABS Plastic. Based on the comparison above, the choice of material is PLA as strength is an important factor while designing a drone arm.

Simulation Results

The deflection of the drone arm along with induced stress and strain was analysed at 7 N (For a propeller running at 8000 rpm). Results from the static structural analysis are presented below for PLA in Figures 4.15 – 4.17:

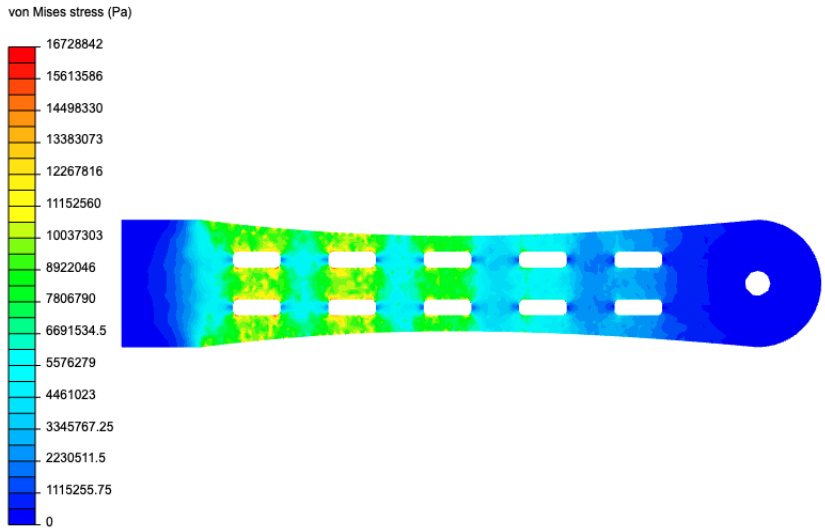

Figure 4.15: Stress induced on the drone arm with material PLA

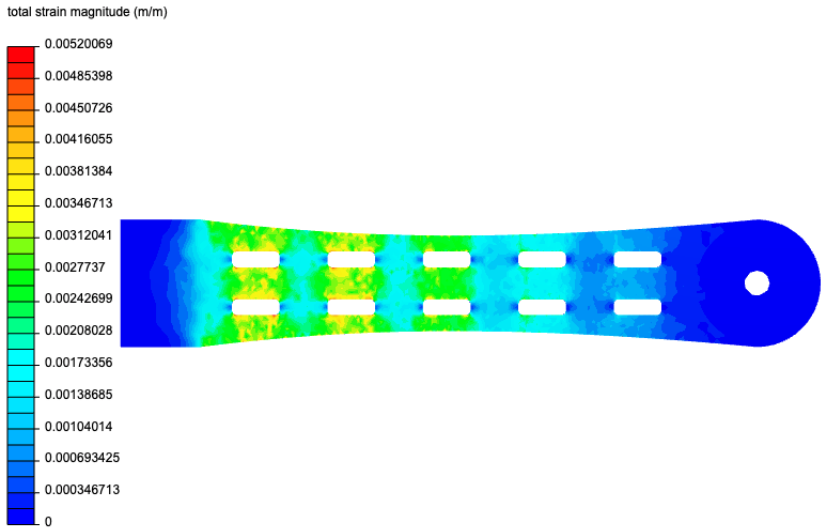

Figure 4.16: Strain distribution on the drone arm

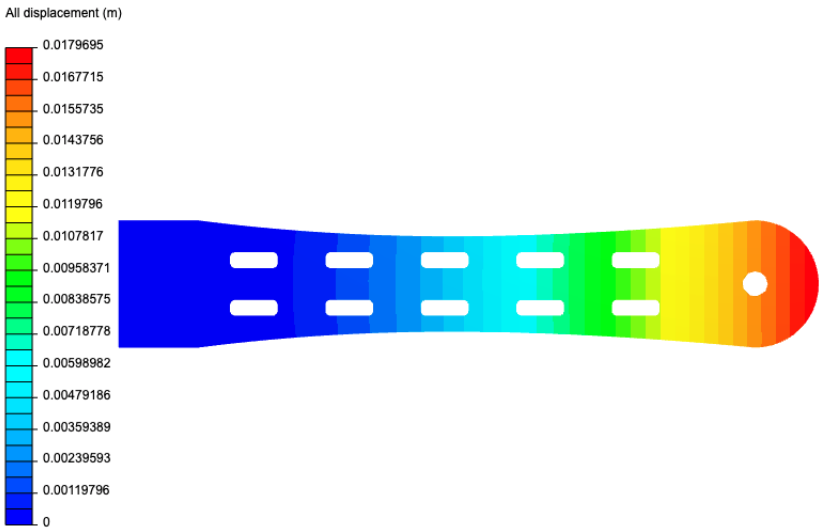

Figure 4.17: Displacement of the drone arm

Results indicate that maximum stress (Von-mises) of 16.728 MPa was induced on the drone arm and the stress is well within the tensile strength of the material. The maximum deflection of 17.9 mm was observed at the free end of the arm. A maximum strain of 5200 $\mu\epsilon$ is seen close to the supporting structure/fixed end.

In any case, the above parameters highly depend on the geometry of the structure and the magnitude of force applied, i.e the higher the thrust produced by the propulsion system, the higher is the magnitude of the above stress, strain, and deflection. Also, to attain stability, the deflection of the drone arm should be minimal, the effect of which is highly dependent on the thickness of the drone arm i.e. with an increase in thickness, the deflection of the drone arm is significantly reduced. However, a smaller deflection would affect the sensing capability, requiring a very sensitive strain gauge. In our application, a higher deflection is indeed an advantage because the sensor would be much more sensitive at these deflections.

4.2.3 Modal Analysis

An important aspect of the design is the study of vibrations and natural modes of a structure. It is a well-known fact that a structure vibrates under a specific load, causing frequency excitation. By performing modal analysis, the natural frequency (or resonant frequency) of the drone arm can be determined. When the natural frequency of a system is known, design failure can be avoided as the frequency serves as a limit of the design.

Also, it is important to identify the possible sources of vibrations to perform modal analysis. In the case of drones, mode excitation originates from the propulsion system (BLDC motor and propellers). The vibration from the propulsion system translates to the drone arm and hence there is a need to determine the natural frequency and potential mode shapes that the drone arm may displace to.

Results

The natural frequency and possible mode shapes for a drone arm are shown in Figures 4.18 – 4.20 :

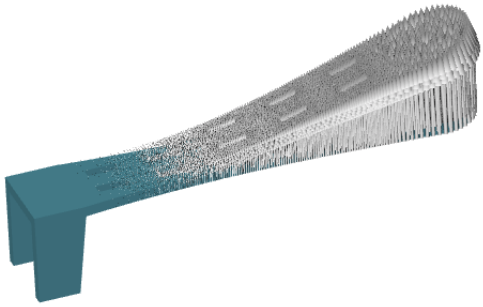

Figure 4.18: First mode frequency 38.2154 Hz

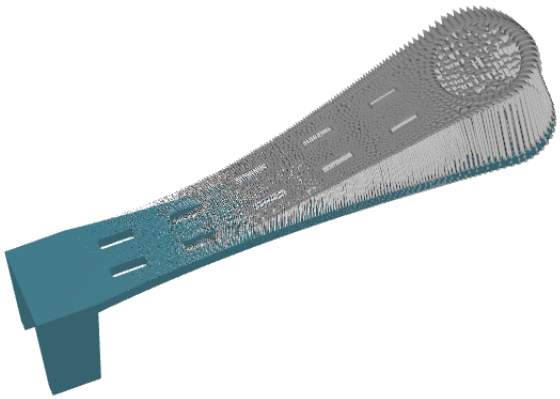

Figure 4.19: Second mode frequency 230.143 Hz

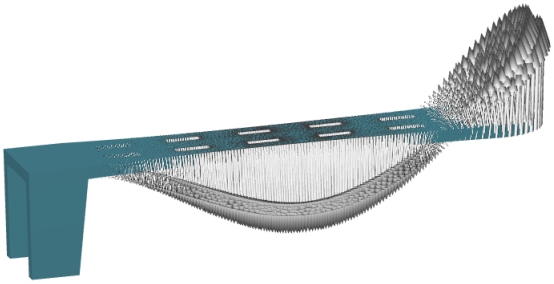

Figure 4.20: Third mode frequency 245.597 Hz

The above three mode shapes in Figures 4.18, 4.19 and 4.20 describe the mode shapes that the drone arm may displace into. The first mode shape has a natural frequency of 38.2154 Hz and is a case of simple bending. The second and third mode shape have a natural frequency of 230.143 Hz and 245.597 Hz respectively. The second mode shape exhibits torsion whereas the third mode shape describes the twisting of the beam. Only the first mode shape is taken into consideration as it describes the flexing/deflection of the drone due to the thrust produced by the propulsion system. There's a possibility of second and third mode being excited. However, this depends on the range of motor frequency and excitation.

In order to determine the occurrence of vibrations on the drone arm, the condition of critical speed can occur when the natural frequency of the beam matches the frequency of the propulsion system. However, the natural frequency of the first mode shape of the drone arm is 38.2154 Hz which is relatively low compared to the frequency of the propeller as found out in Figure 4.8. This indicates that the condition of resonance is not reached. But, the resonance may drop to smaller values if the mass of the drone arm is considered. However, vibrations may still be present around the region of natural frequency. Furthermore, small vibrations could be compensated with the use of rubber dampers for the motor mount.

4.3 Discussion

The implementation of the sensor on the curved geometry of the propeller makes it quite challenging to embed a strain gauge. To read data from the strain gauge, various other sensing principles like capacitive coupling, rotary transformer, or slip rings could be used but add unnecessary weight and complexity on the motor shaft and may not be feasible. Also, to incorporate the above sensing principles, a complete redesign of the motor-propeller assembly is required which is beyond the scope of this assignment. Furthermore, the use of sensors on rotor-propeller assembly makes this method quite complex to implement. In the case of the second scenario (drone arm deflection), the only drawback in this approach is that the accuracy of thrust prediction is highly dependent on the accuracy of the strain gauge and geometry of the drone arm. Therefore, there is a trade-off between the sensitivity of the strain gauge and the deflection of the drone arm.

4.4 Conclusion

A comparison is made between blade flapping and drone arm deflection discussed above. The comparison in Table 4.3 serves as a basis for the selection of the methodology that we intend to proceed with.

Parameters	**Blade Flapping**	**Drone arm deflection**
Implementation of printed sensor	Difficult to implement due to propeller geometry	Easier to implement on a cantilever beam
Effect of additional weight	Sensing principles add unnecessary weight	A simple strain gauge adds negligible weight
Complexity	Complex approach to calculate thrust	Simple approach to calculate thrust using strain pattern
Ease of 3D printing	Difficult to 3D print considering propeller geometry	Easier to print the drone arm than propeller
Design	The propeller will have to be re-designed to accommodate the sensor	Much easier to design a cantilever beam with embedded sensors

Table 4.3: Comparison between blade flapping and drone arm deflection

As seen from the above comparison, the method of blade flapping has various drawbacks. Whereas, in the case of deflection of the drone arm, the approach is quite simple with respect to the implementation of the strain gauge along with the ease of printing the arm and the sensor. The inclusion of a sensor on the drone arm adds negligible weight since it is part of the drone arm. Unlike the method of computing thrust through blade flapping, the condition of the resonance is not reached and the strain gauge measurements are not affected. Therefore, the approach of measuring the thrust indirectly by measuring the strain on the drone arm is more ideal when compared to the method of blade flapping. In the following chapters, this method will be discussed in detail.

5 Design and Fabrication

In this chapter, the design of the drone arm is first presented, supported by FEM analysis to predict potential limits of the design with regards to the maximum permissible stress, strain, and deflection. This is followed by the design of the strain gauge. Next, the positioning of the gauge is determined by a cantilever beam analysis to determine the maximum strain region and bending moment along the length of the beam. Stress-strain distribution is analysed on the chosen design before the final positioning of the gauge. The fabrication of the sensor and the drone arm is then discussed along with the chosen printing parameters.

5.1 Drone Arm

5.1.1 Design

Two iterations of the drone arm were designed in FUSION 360 (Autodesk, USA) to investigate the effect of geometry on parameters such as stress, strain, and deflection at the free end of the drone arm. Both the iterations have the same length and thickness of 200 mm and 5 mm respectively. The only difference between them is that Design 2 has a varying cross-section. Although there is a small difference in the two designs, small factors like varying cross-section may affect the above mentioned parameters such as stress, strain and displacement. On such a structure, the above parameters may be higher or lower and this would be beneficial if sensors were to be mounted on it. This way the effect of drone arm geometry on parameters such as stress, strain, and deflection can also be determined. The two designs are shown in Figure 5.1 and 5.2 respectively.

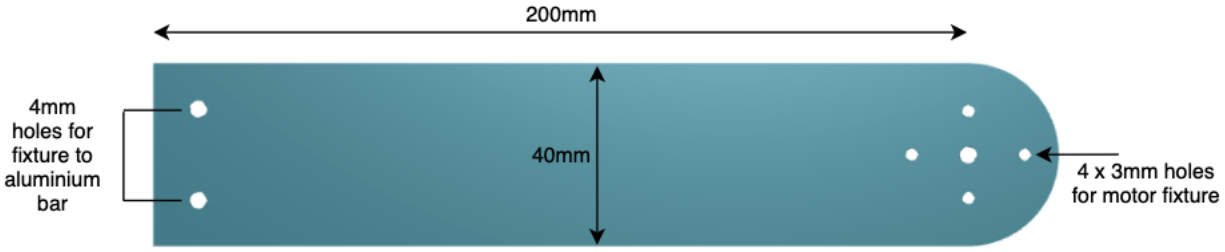

Figure 5.1: Design 1 about 200mm in length, 40 mm wide and 5mm thick. The left side of the drone arm is fixed to a aluminium bar while the motor is fixed on the right side

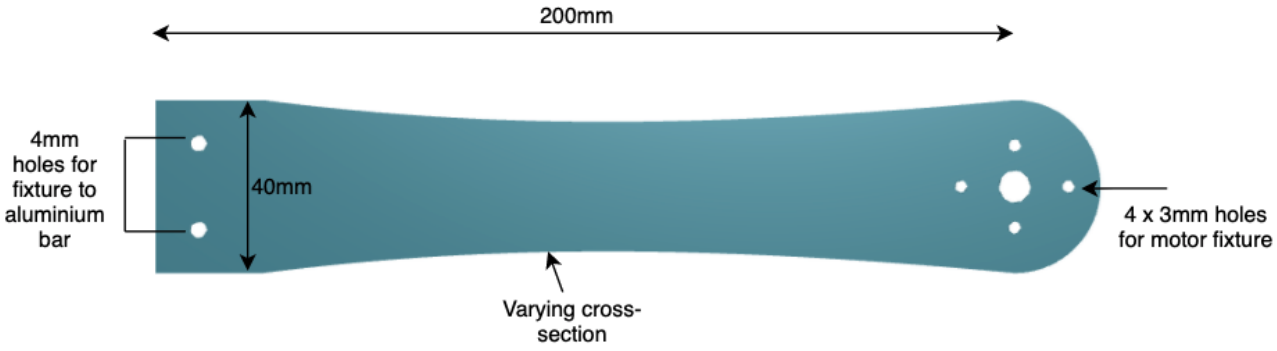

Figure 5.2: Design 2 about 200 mm in length with a varying cross-section.

5.1.2 FEM

The two iterations of the drone arm were analysed using Simscale (Simscale GMBH, Germany) to estimate the magnitude of deformation and the induced stress and strain due to the thrust

produced by the propeller. A free-body diagram of the system is shown in Figure 5.3. The choice of materials for simulation is Poly-lactic acid (PLA).

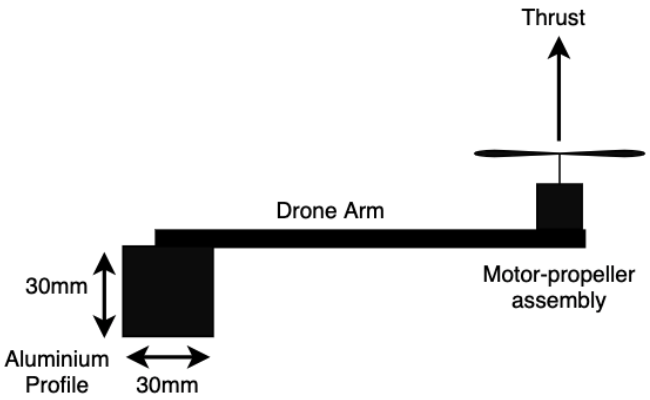

Figure 5.3: Free-body diagram of the drone arm fixed

The materials properties for PLA are listed below in Table 5.1:

	PLA
Young's Modulus (MPa)	3450
Poisson's Ratio	0.39
Ultimate Tensile Strength (MPa)	59.2
Tensile Yield Strength (MPa)	54.1

Table 5.1: Material properties of PLA (ANSYS Inc, USA)

The two design iterations were meshed with an element size of 2 mm as shown in Figure 5.4 and 5.5. Design 1 consists of 32.5k nodes and 160.5k cells whereas Design 2 consisted of 31.4k nodes and 135.6k cells. Each of the design was analysed up-to 10 N.

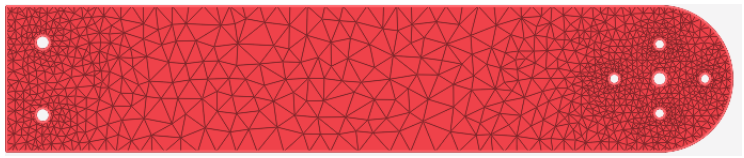

Figure 5.4: Design 1 meshed

Figure 5.5: Design 2 meshed

Boundary Conditions

The following boundary conditions were applied to the drone arm similar to the ones in Section 4.2.1:

- Fixed support on the left side of the drone arm (To replicate fixture on the test setup)
- Force at the center of the motor mount (Thrust produced by the propeller (0.508N-10.287N)). The four holes at the free end (right side) are for the motor fixture.

- Standard earth gravity of 9.81 m/s^2
- Displacement constraint for the screws in all directions (replicates a tight fixture of the screws)

5.1.3 Results

The strain on the PLA drone arm was simulated using a normal force of 10 N, to investigate parameters such as deflection, strain, and stress. Results from the static structural analysis are shown below in Table 5.2:

	Design 1	**Design 2**
Displacement (mm)	13.5	13.8
Von-Mises Stress (MPa)	12.95	14.32
Maximum total strain magnitude ($\mu\epsilon$)	4111	4506
Strain close to fixed support ($\mu\epsilon$)	2741 - 3289	2105 - 3005

Table 5.2: Comparison between Design 1 and Design 2 based on drone arm displacement, induced stress, strain close to fixed support and total strain magnitude

The comparison in Table 5.2 show similar characteristics between the two designs but differ by a small margin. At 10 N, the second iteration is displaced by 13.8 mm and the first iteration by 13.5 mm. The maximum Von-mises stress-induced is 14.32 MPa and 12.95 MPa for Design 2 and Design 1 respectively. Also, the Von-mises stress is well within the limit for both the designs (within the tensile yield strength of 54.1 MPa, indicating that the design is safe. Furthermore, the magnitude of strain at fixed support is higher for Design 2 (4506 $\mu\epsilon$) than Design 1 (4110 $\mu\epsilon$). This would be expected for Design 2, considering the varying cross-section.

Next region of interest is the strain distribution close to the fixed support. It is interesting to see that the strain distribution is higher for Design 1, in the range of 2741 $\mu\epsilon$ - 3289 $\mu\epsilon$, whereas for Design 2, the range of strain is smaller (2105 $\mu\epsilon$ - 3005 $\mu\epsilon$). Based on the comparison between the two designs, Design 1 performs better in terms of a smaller deflection by 0.3 mm. With much higher strain close to fixed support, Design 1 is more suitable as the the strain gauge would be much sensitive at higher strain. Also, a smaller von-mises stress of 12.92 MPa is acceptable for the structural health of the beam.

5.2 3D printed Strain Gauge

In this section, the design of the strain gauge is presented along with the factors that influence the resistance of the strain gauge.

5.2.1 Geometry

Figure 5.6 illustrates the different parameters of a strain gauge: Grid width, U shaped Turns or End Loops, Gauge Length, and Solder tabs.

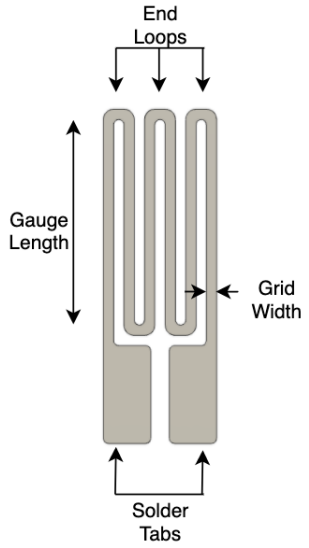

Figure 5.6: Strain gauge geometry

For a grid pattern strain gauge, the end loops limit the effects of transverse strain when under load [52]. The gauge length defines the part of the grid that is sensitive to strain and the solder tabs are insensitive to strain due to their relatively large cross-section or when not placed in the strain region.

The three different gauge geometries listed in Table 5.3 were used to investigate the effect of geometry on resistance. Although these parameters do not necessarily affect the final design of our strain gauge, they are selected based on the dimensions of the drone arm and the region of strain. Table 5.3 mainly provides an insight on the effect of increasing/decreasing the geometric parameters. The number of end loops and grid width has been chosen based on the region of induced strain on the drone arm while the gauge thickness is based on printing layer heights.

Grid Width (mm)	1	1.5	2
Gauge Thickness (mm)	0.2	0.4	0.6
No of End Loops	1	3	5

Table 5.3: Different strain gauge parameters: The choice of parameters can affect the resistance of the strain gauge

Figure 5.7 shows the change in resistance of the gauge to cross-sectional area and clearly show the significant increase in resistance with increasing end loops due to increasing length l in Equation 5.1. Also, an increase in the cross-sectional area A in Equation 5.1 led to a decrease in gauge resistance. Gauges with 5 end loops had nearly thrice as much resistance as that of a gauge with one end loop.

$$R = \frac{\rho l}{A} \tag{5.1}$$

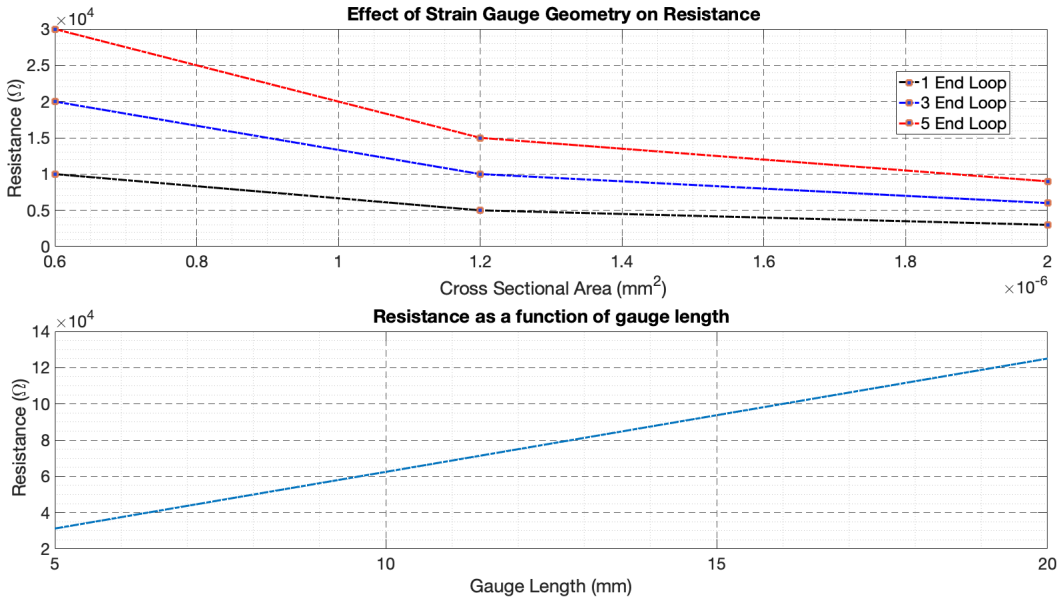

Figure 5.7: Effect of strain gauge geometry on resistance

Therefore, it would be ideal to have 5 end loops and a smaller cross-section . From Table 5.3, a grid width of 1 mm and gauge thickness of 0.2 mm would have the smallest cross-section and inclusion of 5 end loops would give a higher resistance. Also, the resistance increases with increase in gauge length l in Figure 5.7 based on eq. 5.1. The final gauge length was chosen based on the strain region in Table 5.2.

Figure 5.8 shows the designed strain gauge with five end loops, gauge length of 20 mm, grid width of 1 mm and thickness of 0.2 mm. The 3D model was made using Fusion 360 (Autodesk, USA).

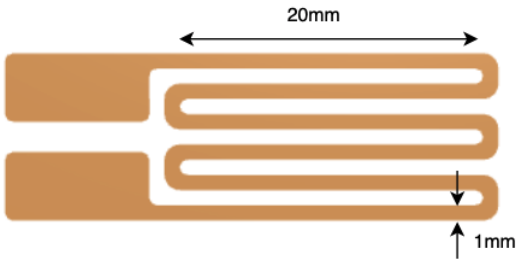

Figure 5.8: 3D model of a strain gauge: gauge length 20 mm, grid width 1 mm, gauge thickness 0.2 mm and 5 end loops

As the strain gauge will be printed using carbon-doped PLA (Proto-Pasta, Protoplant, Inc, USA), it holds a property known as resistivity. A bulk resistivity or volume resistivity (ρ) of 30 Ω-cm was reported by the manufacturer [53]. Therefore, as a first approach, the resistance of the strain gauge can be calculated when the bulk resistivity of the material is known, using the equation:

$$R = \frac{\rho L}{A} \tag{5.2}$$

Here, L is the gauge length and A is the cross-sectional area given by the grid width w and gauge thickness t. The resistance of the gauge was calculated using Equation 5.2 and found to be 180 kΩ.

Although this is true for bulk materials, Equation 5.2 may have limited applicability for a 3D printed structure where the resistance is anisotropic. In such structures, the resistance change due to the piezoresistive effect is much higher when compared to the geometric effect. This piezoresistive effect is mainly due to the changing conductive paths in the polymer matrix [54]. Therefore, the final resistance of the printed structure is not based on Equation 5.2 unless the effect of gauge factor is considered.

5.3 Positioning of strain gauges

5.3.1 Cantilever beam analysis

A simple cantilever beam was analysed to determine the region of maximum strain and bending moment. Based on this, the optimal position for sensor placement can be determined. A simple cantilever beam is shown in Figure 5.9.

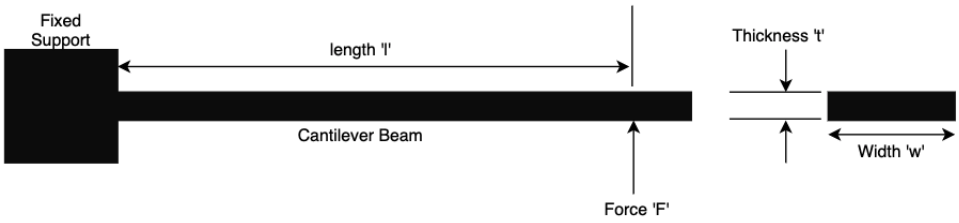

Figure 5.9: A cantilever beam fixed to one end

The beam is fixed to one end and has a width w and thickness t. A force F is applied at the free end of the beam. The distance between the fixed support and force vector is denoted by length l.

For a cantilever beam fixed to one end, strain can be calculated as:

$$\epsilon = \frac{6 \cdot F \cdot l}{E \cdot I} \tag{5.3}$$

Also, the maximum bending moment can be calculated as:

$$M = F \cdot l \tag{5.4}$$

where F is the force in N and l is the distance between the fixed support and force vector. The bending moment is positive if the beam deflects upwards.

It is assumed that the length l is 190 mm, width of the beam w is 40 mm and thickness of the beam t = 5 mm. Now, the strain distribution and bending moment on the beam can be calculated from eq. 5.3 and 5.4 as a function of distance starting from an initial distance of 0 mm until 190 mm in steps of 0.1 mm as shown in Figure 5.10.

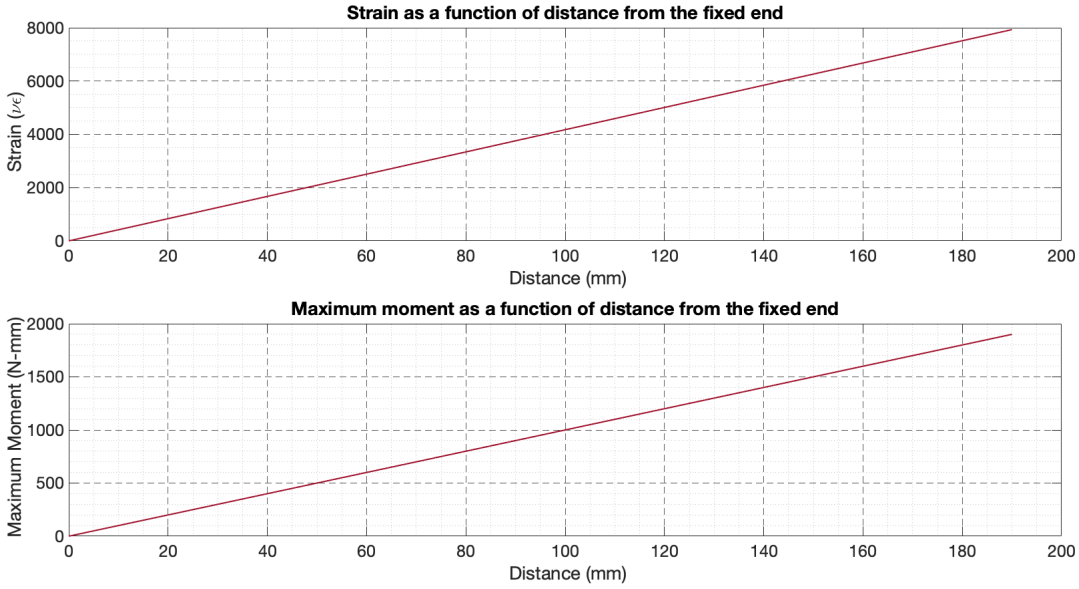

Figure 5.10: Strain and maximum moment on a cantilever as a function of distance from the fixed support

As seen in Figure 5.10, the bending moment and strain is clearly dependent on the distance between the fixed support and the force vector. At a distance of 190 mm or at fixed support, the moment and strain is at its maximum. However, this is not the case away from the fixed support where the magnitude of strain and moment decreases linearly. Therefore, it is ideal to have the sensor closest to the fixed support where induced strain and bending moment is maximum.

5.3.2 Stress-strain distribution on Design 1

To position the sensor on the drone arm, stress and strain distribution is analysed on the chosen design (Design 1). The same boundary conditions from Section 5.1.2 are applied, Figure 5.11 and 5.12 show results from static structural analysis at a force of 10 N:

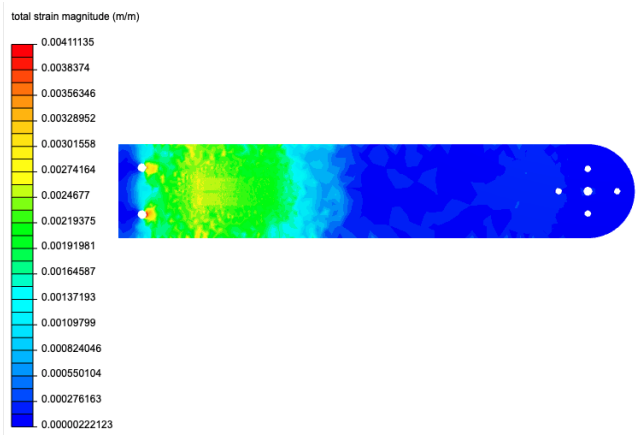

Figure 5.11: Strain distribution on the drone arm

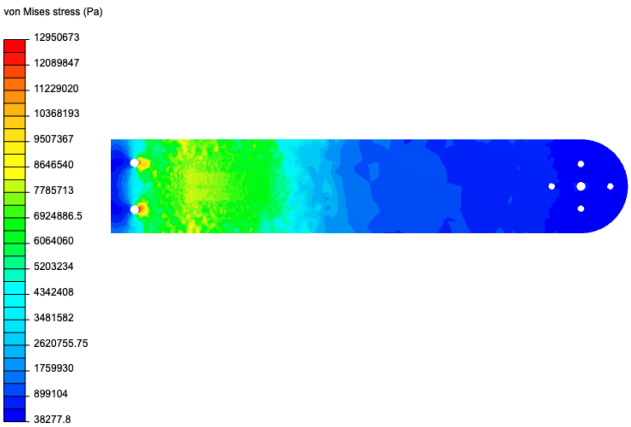

Figure 5.12: Stress induced on the drone arm

As seen in Figure 5.11 and 5.12, most of the stress and strain is concentrated on the left side of the arm , close to the fixed support as estimated earlier in Figure 5.10. Besides the fixed support (screw fixture), where the stress and strain is maximum , the next region of interest is the yellowish and green region. This region is ideal for sensor placement where strain is in the range of (2741 $\mu\epsilon$ - 3289 $\mu\epsilon$). Also, the stress in this region ranges from 6.04 MPa - 9.5 MPa.

The strain gauge cannot be placed closest to the fixed support due to a 30 mm x 30 mm aluminium profile on which it will be mounted on. Also provided is a tolerance of 2 mm for sensor wiring. Hence, a total offset of 32 mm is used as shown in Figure 5.13. It must be noted that another strain gauge is placed symmetrically at the bottom of the drone arm. The strain distribution at sensor location is shown in Figure 5.14. It can be seen that that the sensor is placed in a strain dominant region.

Figure 5.13: Final design of the drone arm

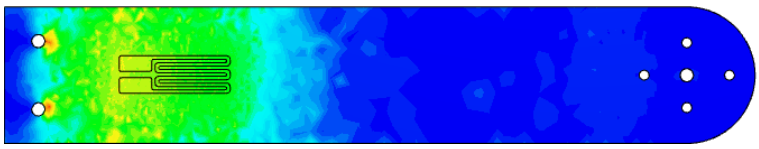

Figure 5.14: Strain distribution at sensor location

5.4 Fabrication

The drone arm was 3D printed using a Diabase H-series (Diabase, USA) printer. The printer comprises of 5 nozzles, thus enabling the use of multiple filament/materials in a single printing cycle. Two materials were chosen for the fabrication process: carbon-doped PLA (Proto-Pasta conductive PLA, ProtoPlant Inc., USA) for the strain gauge and PLA (PLA, 3D-Prima, Sweden) for the non-conductive parts, mainly the drone arm. This combination of PLA and carbon-doped PLA is suitable mainly due to their similar printing temperatures, thus avoiding problems in adhesion when fabricated together.

Using SIMPLIFY 3D (Simplify 3D, USA), the printing parameters were adjusted along with the slicing of the 3D model of the drone arm. The sliced model is shown in Figure 5.15 and the printing parameters in Table 5.4. The diameter of the two nozzles was 0.4 mm.

	PLA	Conductive PLA
Printing Temperature	210	205
Heat Bed Temperature (°C)	60	60
Nozzle Diameter (mm)	0.4	0.4
Print Speed ($mm\,min^{-1}$)	1800	1800
Infill Percentage	20	20
Extrusion Multiplier	0.9	1.1
Extrusion Width (mm)	0.43	0.43
Infill Pattern	Rectilinear	Rectilinear
Layer Height (mm)	0.2	0.2
Outline/ Perimeter Shells	5	5
Amount of Top Layers	3	3
Amount of Bottom Layers	3	3

Table 5.4: Printing parameters

The printing temperature was chosen as specified by the manufacturer. A layer height of 0.2 mm was selected so as to maintain the right layer quality. To improve the adhesion between the initially printed layers, a heat bed temperature of 60 °C was deemed suitable. During the printing process, it was observed that the print quality of the sensor was affected i.e. gauge length of the sensor was distorted. This was then fixed by using 5 Outline/Perimeter shells to ensure better strength and finish. An infill density of 20% was mainly chosen to reduce the weight of the drone arm. Also, with 20% infill, the printing time reduced significantly. The final printing time was approximately 50% lower when compared to a much longer printing time if a 100% infill was used, although the stiffness of the beam was compromised. In Figure 5.15, PLA is highlighted in Purple and carbon-doped PLA in orange. The slicing software estimated a printing time of 3 hours and 8 minutes with an approximate material cost of 1.52 €. The printed drone arm is shown in Figure 5.16

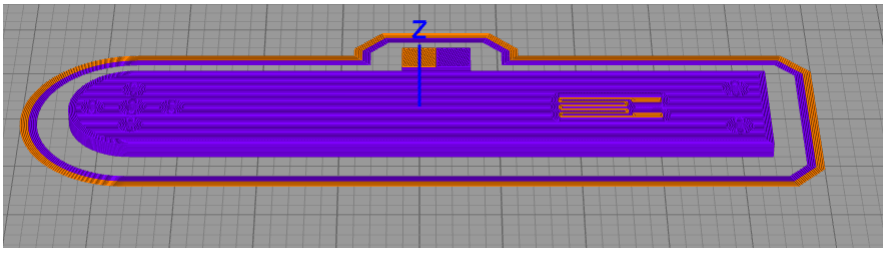

Figure 5.15: Sliced model of the drone arm on SIMPLIFY 3D software

Figure 5.16: Printed drone arm

The resistance of the embedded sensors was found to be 105 kΩ for the top and 54.7 kΩ for the bottom (printed on the heat bed). It was also observed that the print quality of the bottom sensor was much better when compared to the top sensor. Potential causes may be the choice of printing parameters or extrusion inconsistencies. This could indicate that certain printing parameters significantly affect the quality of the print.

5.5 Conclusion

Based on FEM analysis, Design 1 performed better with smaller deflection when compared to Design 2. The strain distribution close to fixed support was found to be higher for Design 1. The stress induced on Design 1 is well within the Tensile Yield Strength of 54.1 MPa, indicating a safe design. Also, the fabricated structure showed reasonable print quality in terms of the final dimensions of both the sensor and the drone arm, albeit better results can still be obtained with certain printing parameters. However, investigating the effect of these parameters is beyond the scope of this assignment.

6 Characterisation and Validation

This section describes the process of characterising the printed sensors using a measurement setup. Also discussed are the measurement protocols and readout technique. The sensor is characterised for accuracy, non-linearity, hysteresis and repeatability. The bandwidth of the sensor is also determined. The performance of the sensor in close proximity to the ground is also discussed. Finally, results from the sensor characterisation and motor setup are presented.

6.1 Methodology

6.1.1 Setup

To understand the behaviour of the sensor, a test setup comprising of a linear actuator was used in combination with a digital oscilloscope that reads sensor measurements.

(a) SMAC actuator **(b)** Tie-pie HS5 oscilloscope

Figure 6.1: SMAC actuator and digital oscilloscope

Using a force-controlled SMAC linear actuator (LCA25-050-15F) as shown in Figure 6.1, force is applied on the free end of the drone arm (along the motor axis) in the range of 0 N - 10 N. The actuator is controlled using MATLAB (MathWorks Inc., USA). With a MATLAB script, the force can be applied linearly or sinusoidally.

The printed sensors are connected individually in a voltage divider configuration (Figure 6.2) comprising of a fixed resistor with a resistance of 100 kΩ and 47 kΩ for sensor 1 (under tension) and sensor 2 (under compression) respectively. The measurements are read out using the 2 channel HS5 digital oscilloscope from Tie-Pie as shown in Figure 6.1 and visualised on Tie-Pie multi-channel software (Tie-Pie Engineering, Netherlands). The input voltage is set to 1 V and sampling frequency to 2 KHz.

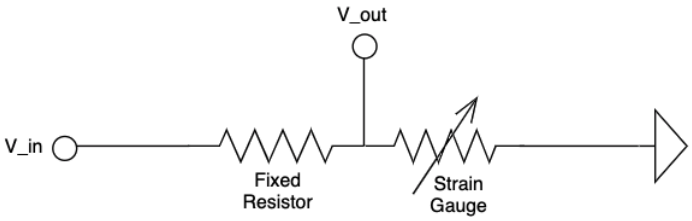

Figure 6.2: Voltage divider circuit : V_{in} is the supply voltage and V_o is the output voltage

Measurement Protocol

The force (F_L) of the linear actuator is controlled using MATLAB (Mathworks Inc., USA). The same program also captures the actual position and force data. The preliminary step involves measuring the resistance of both the strain gauge under no load. This way it can be verified that the resistance increases/decreases based on the load applied. To characterise the sensor, force is applied on the drone arm in the range of 1 N-10 N in increments of 1 N. This way force-strain relation is determined along with the displacement of the arm. Repeatability of the sensor is measured in a similar manner by loading the beam sinusoidally at 0.5 Hz. To measure the hysteresis, force commands of 0 N - 10 N are sent and then unloaded in decrements of 1 N.

The obtained output voltage from the sensor is converted into force based on calibration equations:

1. First, the initial output voltage V_{initial} (under no load) of the two sensors is noted. This output voltage is converted into resistance using the simple voltage divider equation:

$$R_{\text{initial}} = \frac{V_{\text{initial}} \cdot R_f}{V_{\text{in}} - V_{\text{initial}}} \tag{6.1}$$

   where R_f is the value of the fixed resistor. The input voltage V_{in} is set to 1 V.

2. The output voltage of the sensor is measured for a range of force commands and converted into resistance using the same Equation 6.1. This change in resistance is given by:

$$R_{\text{gauge}} = \frac{V_{\text{gauge}} \cdot R_f}{V_{\text{in}} - V_{\text{gauge}}} \tag{6.2}$$

   Here, V_{gauge} is the output voltage of the sensor corresponding to different force commands.

3. Due to the presence of noise in the measurements, the data is filtered using a 2^{nd} order Butter-worth low pass filter with a cut-off frequency of 5 Hz.

4. The strain on the drone arm at the position of the strain gauge (ϵ_g) is then calculated using the filtered data:

$$\epsilon_g = \frac{\Delta R / R_{\text{initial}}}{\text{GF}} \tag{6.3}$$

   where R_{initial} is the initial resistance of the sensor and GF is the gaugefactor. ΔR is given by:

$$\Delta R = R_{\text{gauge}} - R_{\text{initial}} \tag{6.4}$$

5. Finally, the sensor determined force ($\tilde{F}_L$) is obtained from the strain equations for a cantilever beam using:

$$\tilde{F}_L = \frac{\epsilon_g \cdot E \cdot I}{6 \cdot x} \tag{6.5}$$

   where E is Young's modulus of the material, I is the moment of inertia and x is the distance from the motor axis to the sensor.

6. A calibration factor of 0.5 is used to determine the final value for $\tilde{F}_L$, due to the effect of infill density.

6.1.2 Results

In this section, results from the characterisation are presented. The behaviour of sensors is discussed in terms of noise, non-Linearity, hysteresis and repeatability.

Noise

To characterise noise in the sensor, a test was conducted at no load. The output voltage of the two sensors was recorded for 12 s. Figure 6.3 clearly show the presence of noise in the top and bottom sensor along with differential measurements.

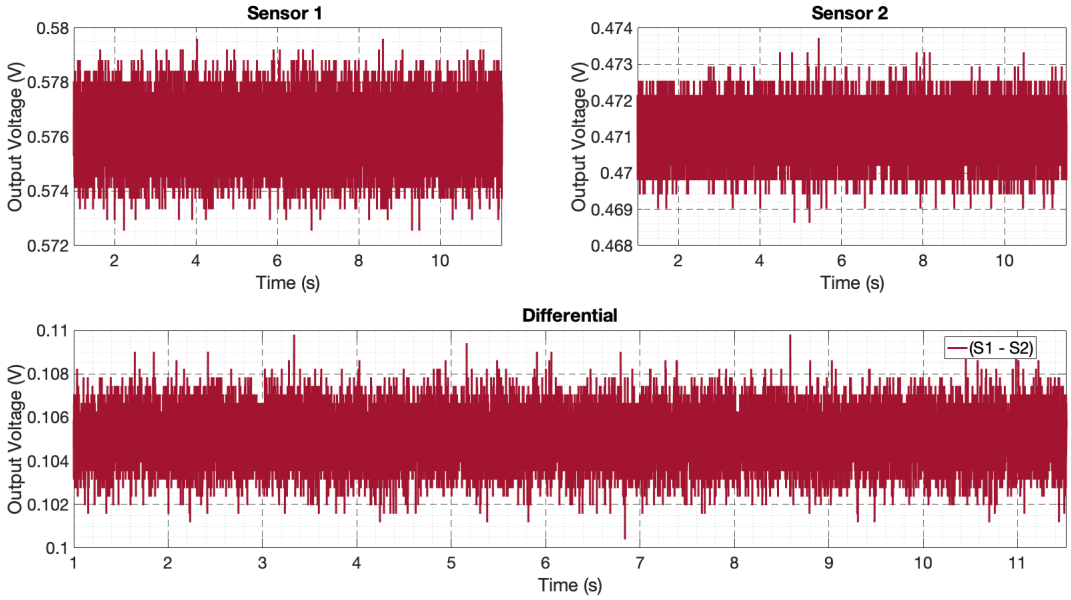

Figure 6.3: Measured Noise at no load for sensor 1 , sensor 2 and Differential

The presence of noise in the measurements could possibly be due to thermal Johnson–Nyquist noise which is a fundamental property of resistors and, thus also, of strain gauges. The thermal noise can be calculated as [55]

$$V_{\text{Nyquist}} = \sqrt{4 \cdot K \cdot T \cdot R \cdot B} \tag{6.6}$$

where $K = 1.380\,649 \times 10^{-23}\,\text{JK}^{-1}$ is the Boltzmann's constant, T is the absolute temperature of the resistor in K, B is the noise bandwidth in Hz and R is the resistance in Ω.

At the time of experiment, the room temperature was 22°. It is assumed that the resistor has the same temperature. The same data from Figure 6.3 was used and converted to resistance using the voltage divider equation discussed earlier. The bandwidth of the sensor was 1 KHz. Using eq. 6.6, the RMS noise voltage was found to be relatively small i.e 1168.7 nV and 794.74 nV for the top and bottom sensor respectively.

The noise power P can be calculated as :

$$P = 4 \cdot K \cdot T \cdot B \tag{6.7}$$

The noise power of the sensors was found to be 1.6568×10^{-17} W.

A 2$^{\text{nd}}$ order Butter-worth filter with a cutoff frequency of 5 Hz was used to filter the noisy data. Filtered data is shown in Figure 6.4. Also seen is the remaining noise in the measurements;

for both the sensors in the order of 0.0003 V. Furthermore, differential measurements are not sufficient to compensate for this drift, although their magnitude is relatively small.

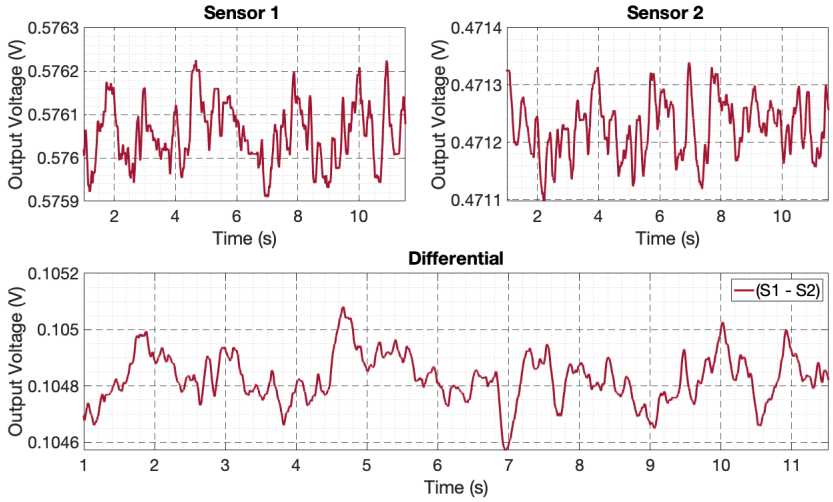

Figure 6.4: Noise filtered using a 2nd order Butter-worth low pass filter with a 5 Hz cutoff frequency

Non-Linearity

To determine the non-linearity in the sensors, fractional changes in resistance were measured against loading force ranging from 0 N - 10 N in steps of 1 N. Figure 6.5 shows non-linearity for sensor 1 and sensor 2 in tension and compression respectively.

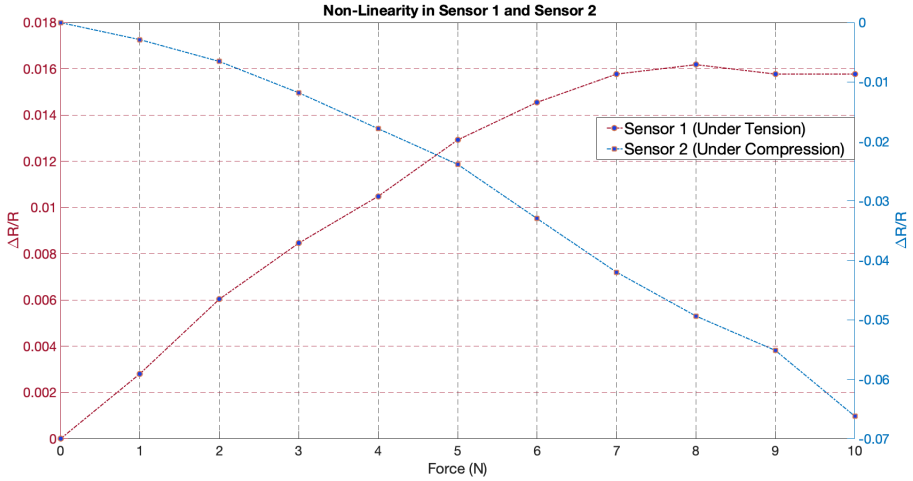

Figure 6.5: Non-linearity

In the case of sensor 1 (under tension), the relationship between force and $\Delta R/R$ is almost linear until 7 N, beyond which a non-linear region is observed. This could be the saturation limit of the top sensor. However, this is not the case for sensor 2 (under compression) where the linear relationship between force and $\Delta R/R$ is significantly better than sensor 1. Also, the maximum fractional change in resistance for sensor 2 is about 7% at 10 N when compared to sensor 1 with maximum resistance change of 1.6% at 8 N. This could indicate that the sensor is sensitive to compression than tension.

Gauge Factor

Another important parameter of the strain gauge is the Gauge Factor (GF) which defines the sensitivity to strain, given by [56]:

$$\mathrm{GF} = \frac{\Delta R/R}{\Delta L/L} \tag{6.8}$$

where change in length is denoted by ΔL under stress and ΔR is the change in resistance under stress.

Based on the material of the strain gauge, the GF can also be computed as [56]

$$\mathrm{GF} = 1 + 2\nu \tag{6.9}$$

For PLA, the poisson ratio (ν) is 0.39 (ANSYS Inc., USA). Therefore, the gauge factor is:

$$\mathrm{GF} = 1 + 2\mu = 1.78$$

However, this is only true for conductors with no piezo-resistive effect. It's expected that the gauge factor might be larger with piezo-resistive effect [20].

Gauge Factor Of Printed Strain Gauges

The sensitivity of the two printed strain gauges was measured in the form of the gauge factor. The sensitivity of the gauges was verified by measuring the fractional change in resistance against strain. As the beam was actuated using a linear actuator, the strain in the beam was derived from the actuation force using the Euler Beam theory as:

The drone arm can be approximated as a cantilever beam. Strain on a cantilever beam can be calculated as [8]:

$$\epsilon = \frac{6 \cdot F \cdot x}{E \cdot I} \tag{6.10}$$

where F is the force of the linear actuator, E is Young's modulus of the material, x is the distance from the motor axis to the sensor and I is the moment of inertia given by :

$$I = b \cdot t^2 \tag{6.11}$$

Here, the width of the beam is given by w and t is the thickness.

Figures 6.6 and 6.7 show $\Delta R/R$ against Strain ϵ for the two sensors. The test was conducted by actuating the beam starting from 0 N - 10 N in steps of 1 N and then unloaded back to 0 N in a similar manner.

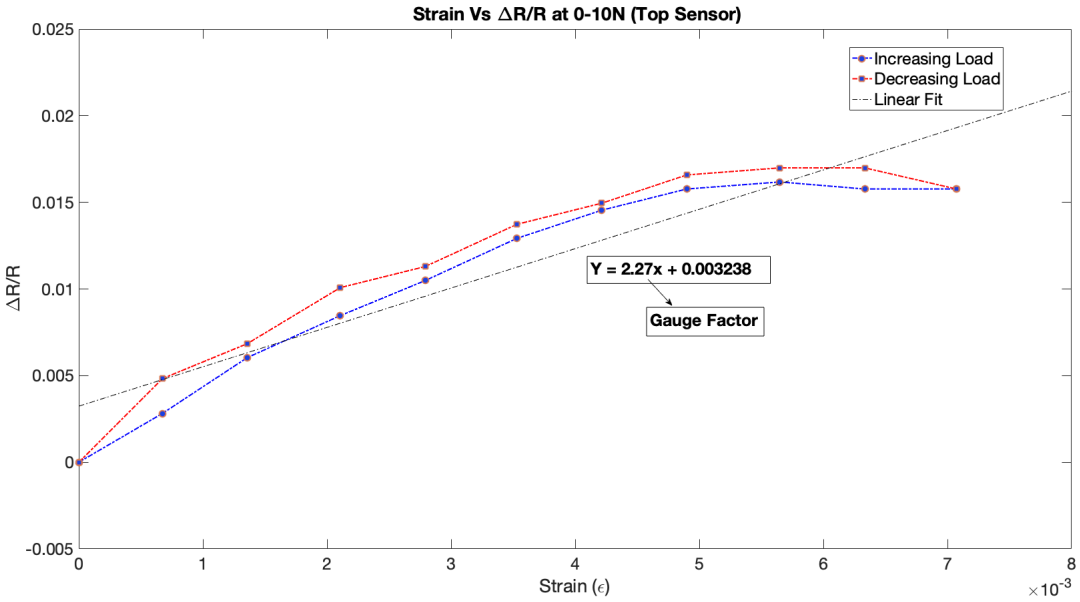

Figure 6.6: Gauge factor Of top sensor

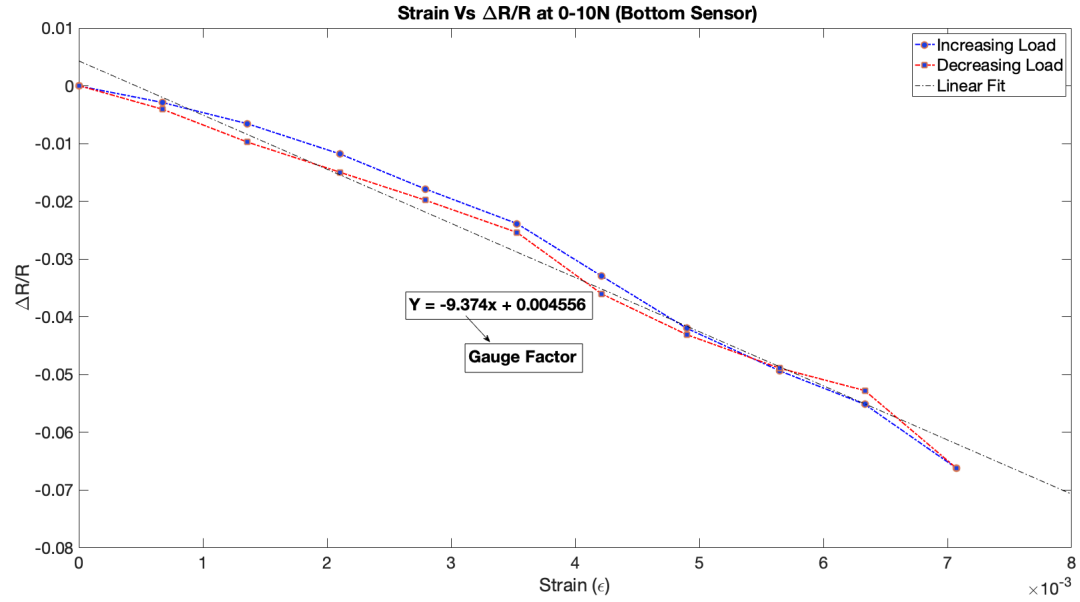

Figure 6.7: Gauge factor of bottom sensor

The results from the tests in Figure 6.6 and 6.7 show a relationship between $\Delta R/R$ and strain for the two sensors. Also seen is relatively small hysteresis for the two sensors. The gauge factor for the two sensors was obtained by taking the slope of the linear fit. A gauge factor of 2.27 for the Top sensor and -9.374 for the bottom sensor was obtained. When compared to the simple expression eq. 6.9 where a gauge factor of 1.78 was obtained for PLA, the top sensor has a relatively close gauge factor (2.27) whereas this is not the case for the bottom sensor (-9.374). When the beam is flipped upside down i.e. the sensor under tension is now in compression and vice versa, the two sensors had a similar gauge factor in tension (2.32) and compression (-9.402) as shown in Figure 6.8, indicating the fractional change in resistance is much higher when in

compression than tension. The higher gauge factor may be due to the piezo-resistive effect of the material [20].

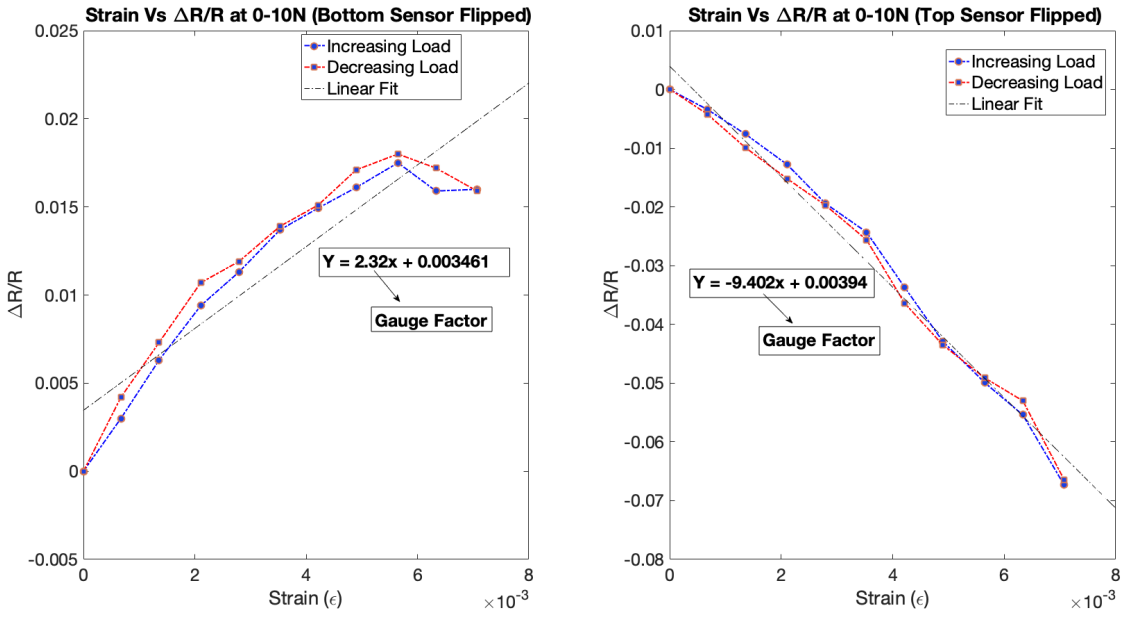

Figure 6.8: Gauge factor of top and bottom sensor when flipped: The sensor which was under tension in Figure 6.5, is now under compression and vice versa

Repeatability

Repeatability of the sensor is determined by actuating the drone arm in a sinusoidal manner from 1 N - 10 N for 10 periods. Figure 6.9 shows the results obtained from the repeatability test where the data has been filtered using a 2nd order Butterworth filter of 5 Hz cut-off frequency. The sampling frequency of the data is 2 KHz.

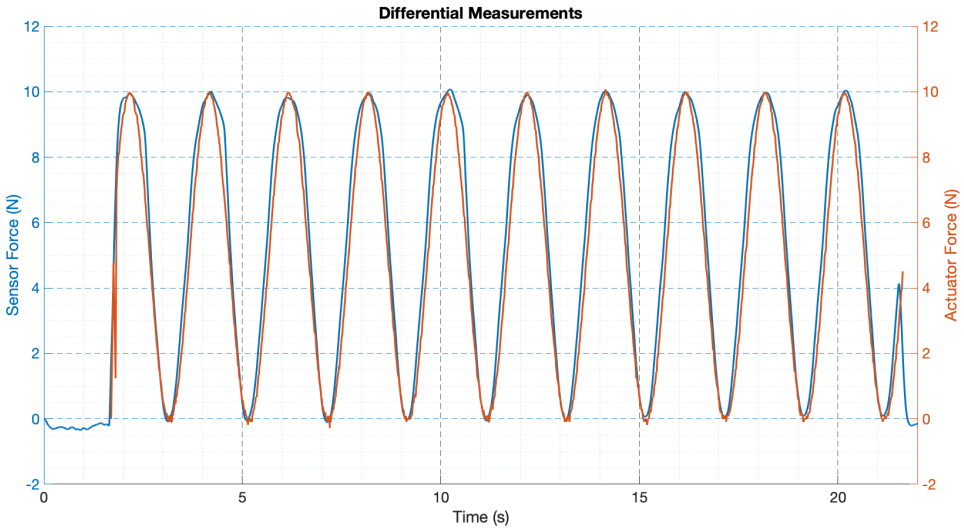

Figure 6.9: Repeatability of sensor measurements in comparison to the actuator

The results in Figure 6.9 indicate the repeatability of sensor measurements. The obtained differential measurements have a good agreement with the actuated force of the linear actuator. It is

assumed that the linear actuator is accurate. It would be ideal to have a load cell mounted on it to determine the actual force.

Hysteresis

The sensor was characterised for hysteresis by actuating the sensor from 0 N - 10 N and then unloaded back to 0 N in a similar manner. This was repeated for two cycles. Figure 6.10 shows the obtained filtered differential measurements from the two sensors.

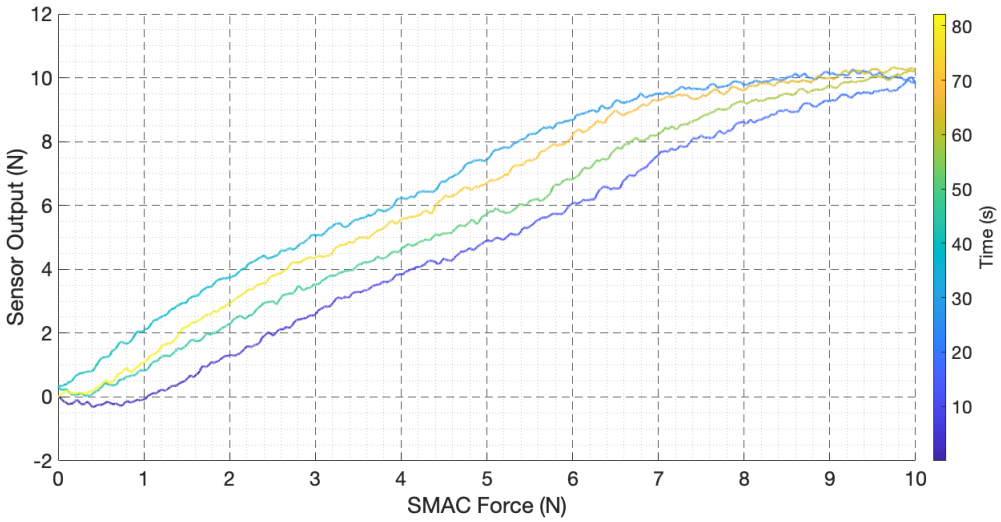

Figure 6.10: Hysteresis characterisation of the two printed sensors

From Figure 6.10, clearly seen is hysteresis in the sensors. The hysteresis is relatively larger in the first cycle (in blue) when compared to the second cycle (green (loading) and yellow (unloading)). In the first cycle, the response is almost linear at a force of 1 N - 7 N. It is also interesting to see the saturation region at 8 N - 10 N, contributing to differential measurements where this behaviour is also reported in the top sensor while checking for non-linearity in Figure 6.5. Overall, there was hysteresis in the sensor when actuated in the range of 0 N - 10 N with the linear actuator.

6.2 Data Analysis

6.2.1 Residuals

To check the accuracy of measurements obtained with both sensors, a residual analysis was performed in MATLAB (Mathworks Inc., USA) using the curve-fitting toolbox. A first-order polynomial function was used for the fitted curve which represents a linear fit. The best fit and residuals for sensor 1 (under tension) and sensor 2 (under compression) are shown in Figure 6.11 and 6.12 respectively.

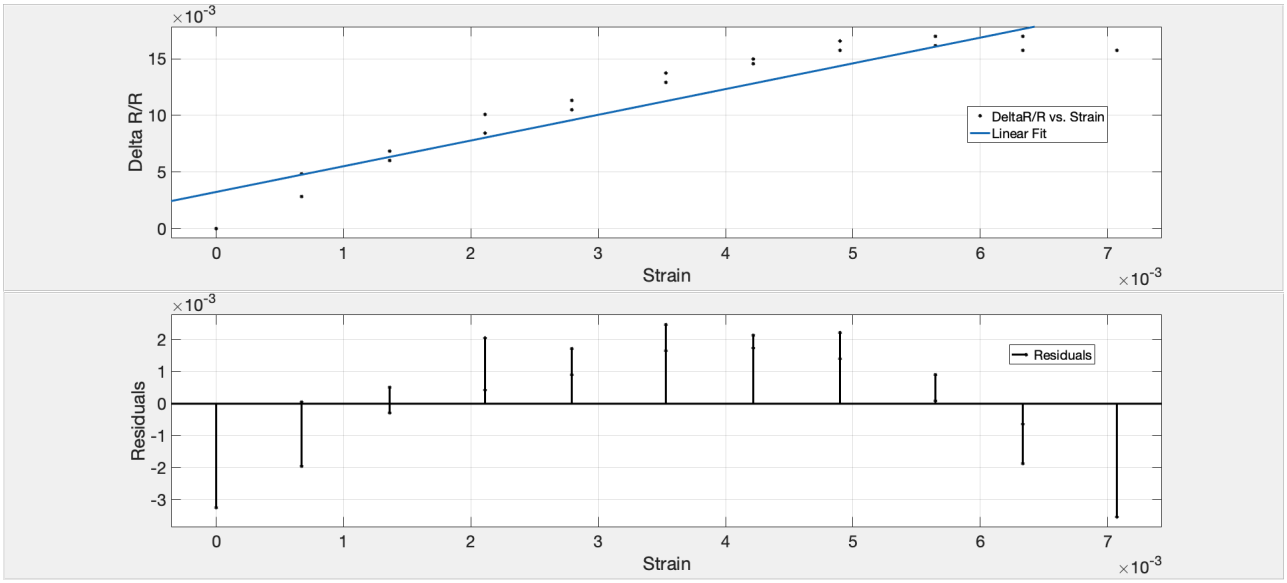

Figure 6.11: Residuals between best fit and sensor measurements for the top sensor

The top plot in Figure 6.11 shows the fractional change in resistance as a function of strain. It can be seen that there is a significant difference between the predicted output and sensor measurements. This could be possibly due to the chosen first-order polynomial function. The bottom plot in Figure 6.11 shows the residual as a function of strain where all the measurements are scattered around the 0 line. Residuals closest to 0 indicate a perfect fit between the measurements and the predicted output. The scattering of residuals at different strain is also due to the non-linearity of the sensor as seen earlier in Figure 6.5. A root mean square error (RMSE) of 0.00207 was found for the top sensor.

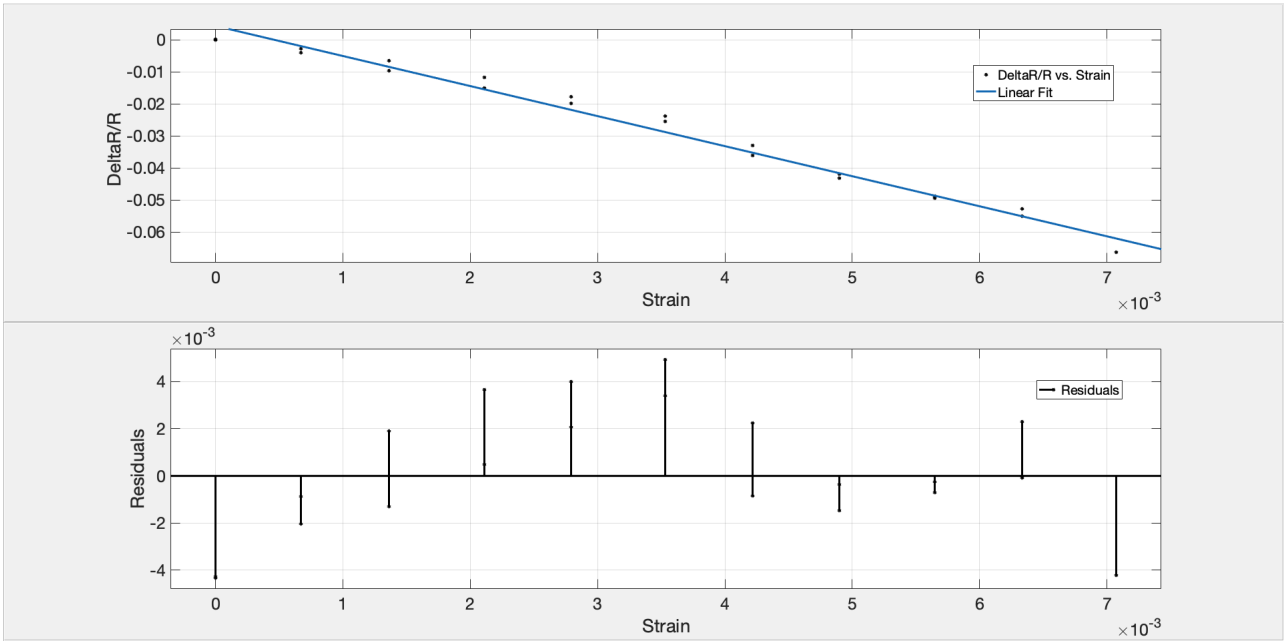

Figure 6.12: Residuals between best fit and sensor measurements for bottom sensor

As for the bottom sensor in Figure 6.12, a good correlation is seen between the predicted output and the obtained measurements. The root mean square error (RMSE) was found to be 0.0028. Once again, the residuals for the bottom sensor are minimal.

It must be noted that the best fit does not start from 0 in our case due to the consideration of a first-order polynomial i.e. linear fit as gauge factor is based on linear relationship between strain and fractional change in resistance. The gauge factor can again differ based on the chosen polynomial function as the slope of the line changes at higher polynomials. Also, the residual error may again increase/decrease based on polynomial functions. Overall, the residuals for both sensors are satisfactory despite considering a linear fit for a not so linear sensor.

6.2.2 Effect Of Infill Density

As the drone arm was printed with a 20% infill, it was necessary to analyse the effect of infill on strength of the beam when compared to infill of 100%. Firstly, the deflection of the drone arm was measured for force in the range of 0 N - 10 N. This deflection was then validated based on simulations from FEM and the simple Euler Beam Theory. Results are shown in Figure 6.13.

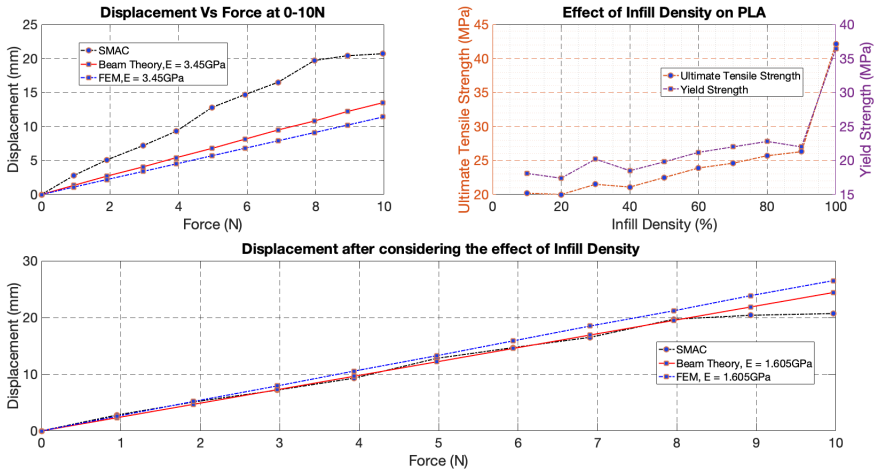

Figure 6.13: Measured deflection of the beam (Top left), effect Of infill density on yield strength and ultimate tensile strength for PLA [13] (Top right), deduced young's modulus from measured displacement (Bottom)

The top left plot in Figure 6.13 clearly shows the discrepancies between the measured deflections and results from FEM and Beam theory. It can be seen that the beam deflects about twice as much when compared to deflection from FEM and beam theory where the default Young's modulus of the material was 3.45 GPa. The top right plot shows the effect of infill density on ultimate tensile strength and yield strength for PLA [13]. Clearly seen is the increase in strength with an increase in infill percentage. Results from [13] show that at 100% infill, PLA has a yield strength of 36.40 MPa and an ultimate tensile strength of 42.15 MPa. As the drone arm was printed with 20% infill, the stiffness of the drone arm is compromised, causing it to deflect twice as much. Besides the effect of infill, there's also a possibility that the printed structure has different properties in a different direction due to their anisotropic behaviour.

Based on the obtained measurements of deflection, an effective Young's modulus was derived based on the simple beam theory equation assuming the drone arm as a cantilever beam. An effective Young's modulus ($\bar{E}$) of 1.605 GPa was obtained. Using this new Young's modulus, the drone arm was again then analysed using FEM and Euler beam theory. Results in the bottom plot indicate a good correlation between the measurements and FEM and Beam theory. This indicates that the effective Young's modulus of was significantly reduced relative to the the expected Young's modulus of the material due to the chosen Infill density.

The effect of infill density was also reported by [57] where the tensile properties of PLA increased with increase in infill density for a grid pattern. A young;s modulus of 2.76 GPa, 2.8 GPa and 3.28 GPa was obtained for 25%, 50% and 70% infill density respectively.

6.3 Motor Setup

To evaluate the feasibility of the developed thrust sensor, a series of experiments was conducted using a motor setup. The motor setup comprised of an aluminum profile on which the drone arm was rigidly mounted. An M3638 motor is used in combination with a 13 inch propeller with a pitch of 4.5. The closed-loop speed controller developed by Franchi et. al [58] is used. The major advantage of such a speed controller is that it can be implemented without any knowledge of motor-propeller parameters.

Measurement Protocol

Motor commands are sent to the motor via the electronic speed controller (ESC) using Matlab. Communications to the motor and ESC are made using the genomix package for the motor setup. The same Matlab script measures the actual frequency of the motor, current drawn and throttle percentage. The printed sensor on the other hand measures the deflections of the drone arm for a series of motor frequencies. Repeatability of the sensor is checked by sending motor commands in the range of 20 Hz - 90 Hz for a series of three tests. To characterise the hysteresis, the script sends motor commands starting from 20 Hz up till 90 Hz in steps of 10 Hz. The bandwidth of the sensor is checked using a simple sine wave script which sends sinusoidal motor frequency commands at 0.5 Hz, 1 Hz and 1.5 Hz. The sensor performance is then checked for different actuation frequencies. The same calibration equations from 6.1.1 are used to convert the voltage to thrust.

6.3.1 Results

This section presents the obtained results with the motor setup. The sensor is once again evaluated for noise, repeatability, hysteresis, and accuracy. Finally, the sensor is characterised in presence of the ground effect.

Noise At No-Load With Motor Mounted

Similar to Section 6.1.2, noise in the sensor is characterised by conducting three tests at no load but with the motor mounted on the drone arm. Figure 6.14 shows the presence of noise in the data.

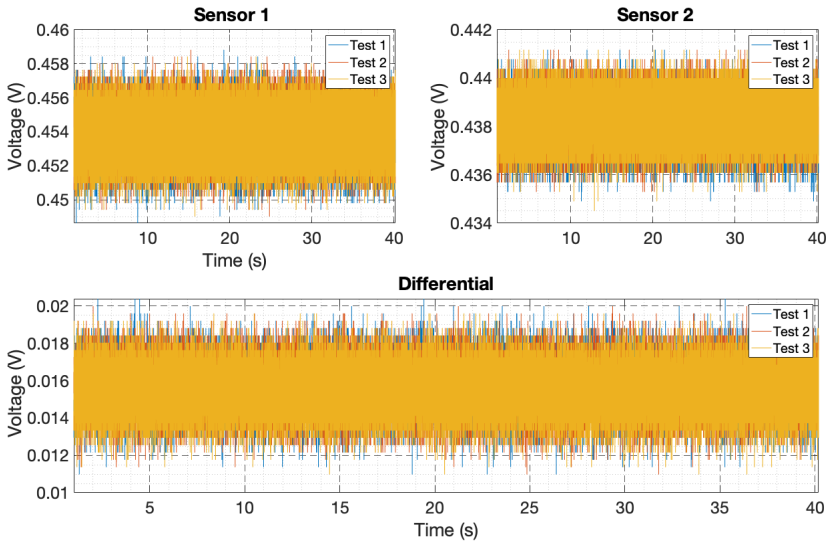

Figure 6.14: Measured noise at no load

To reduce the noise in the measurements a 2nd order Butter-worth filter with a cutoff frequency of 5 Hz has been used. Filtered data is shown in Figure 6.15 where the sensor drifts over a span of

40 s. This drift is compensated using differential measurements where a significant improvement is seen in the measurements (bottom plot in Figure 6.15), eliminating drift to a great extent. It is interesting to see that differential measurements can compensate for drift. However, this was not the case when a linear actuator was used.

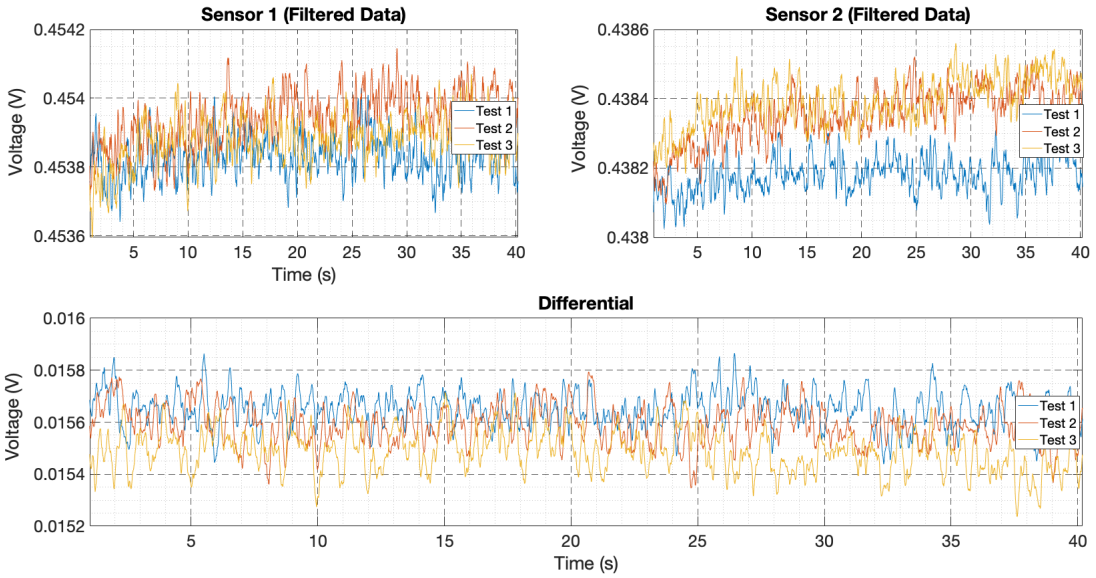

Figure 6.15: Filtered data

Bandwidth

The bandwidth of the sensor was characterised using a sinusoidal motor command in the range of 20 Hz - 90 Hz at different actuation frequencies. Figures 6.16 , 6.17 and 6.18 show results from the measurements at 0.5 Hz , 1 Hz and 1.5 Hz respectively.

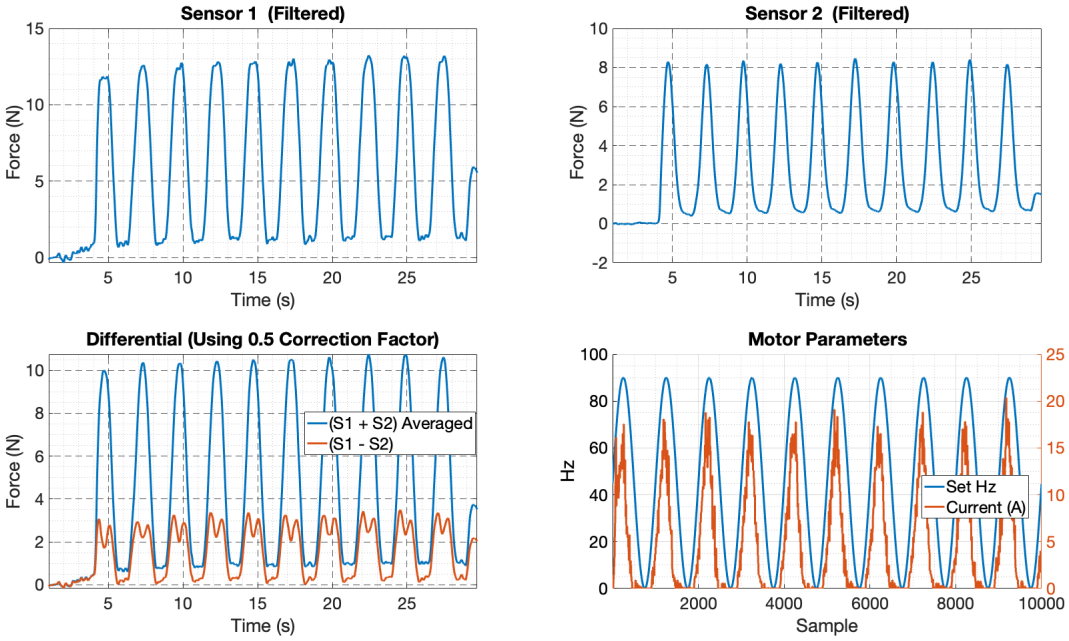

Figure 6.16: Actuation at 0.5Hz

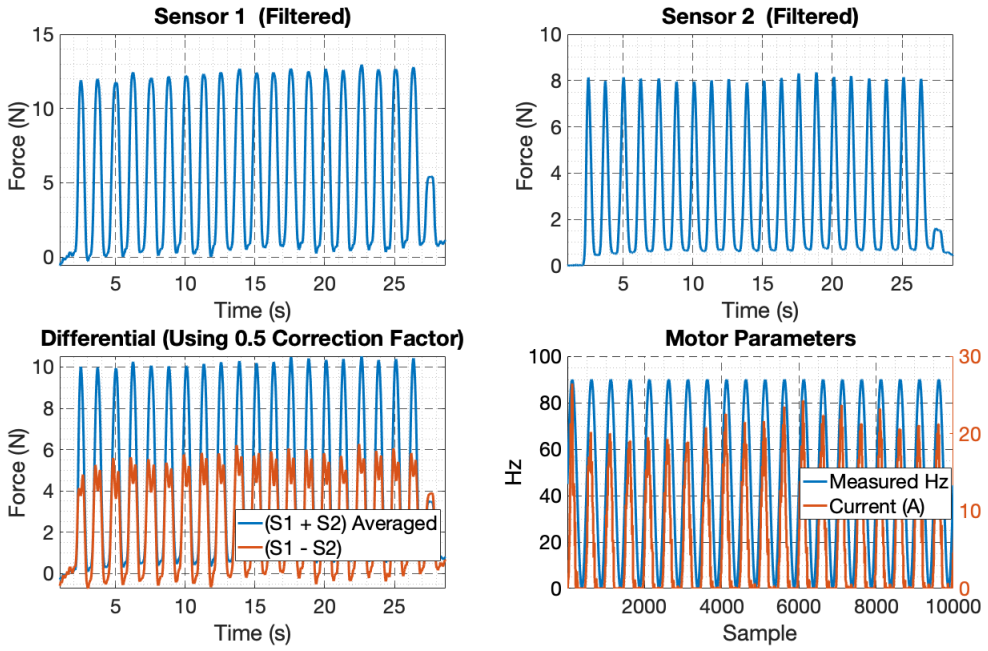

Figure 6.17: Actuation at 1Hz

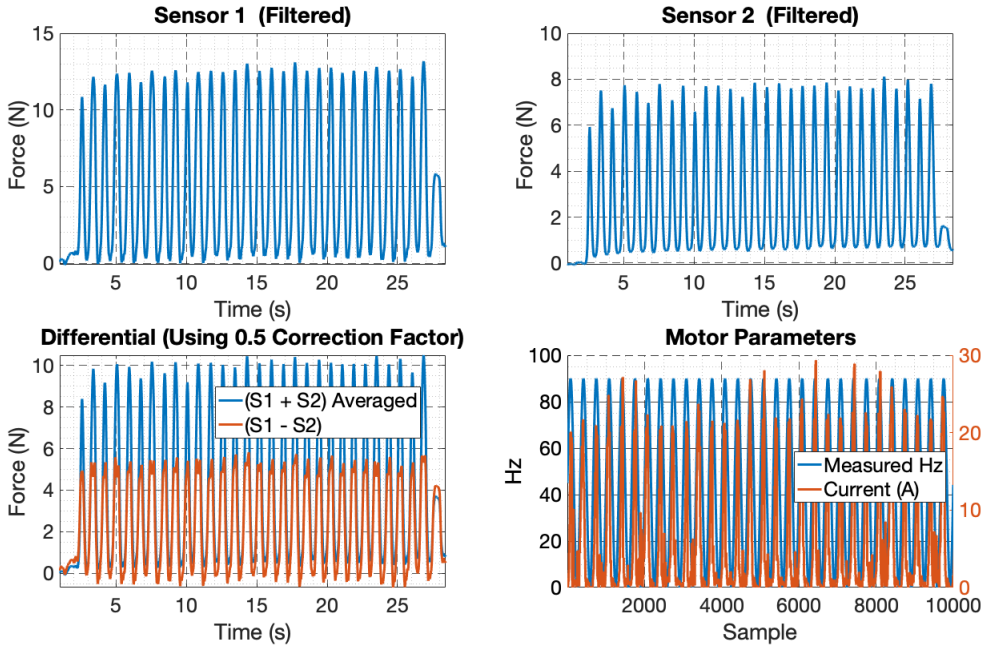

Figure 6.18: Actuation at 1.5Hz

Figures 6.16 , 6.17 and 6.18 show the effect of actuation frequency on measured thrust. At 0.5 Hz (Figure 6.16), the differential measurements seem to deviate slightly. A much higher deviation is seen in the case of the top sensor whereas the bottom sensor seems to drift at about 5 s. A higher deviation in measurements is also seen at 1.5 Hz in Figure 6.18 where measurements from both the sensors are non-repeatable, thereby affecting differential measurements as well. However, this is not the case at a frequency of 1 Hz (Figure 6.17). Over a span of 30 s, the measurements are much more repeatable than when the sensor was actuated at a frequency of 0.5 Hz and 1.5 Hz.

Repeatability

Figure 6.19 shows the repeatability of the sensors based on three tests. To characterise the repeatability of the sensor, the motor was run for 5000 samples in the frequency range of 20 Hz - 90 Hz.

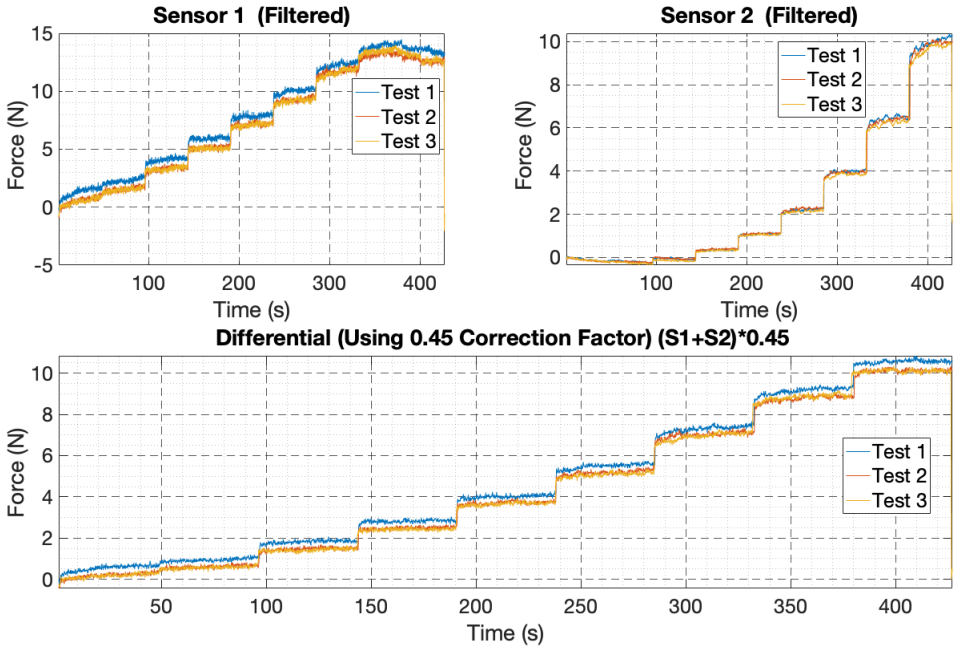

Figure 6.19: Repeatability test

From the results in Figure 6.19, it can be seen that the three results show a good agreement but with some delays. This is due to syncing issues while running the motor and reading measurements from the oscilloscope, thereby causing a delay between when the test was started and stopped, leading to more samples for one test than another). Also, at 350-400s, the top sensor seems to go into the non-linear region when the motor frequency is switched from 80 Hz to 90 Hz. The bottom sensor remains unaffected. Overall, the sensor measurements are repeatable.

Hysteresis

To check for hysteresis, the motor was given inputs from 20 Hz - 90 Hz for 5000 samples and back to 20 Hz in a similar manner. Figure 6.20 shows results from the hysteresis test.

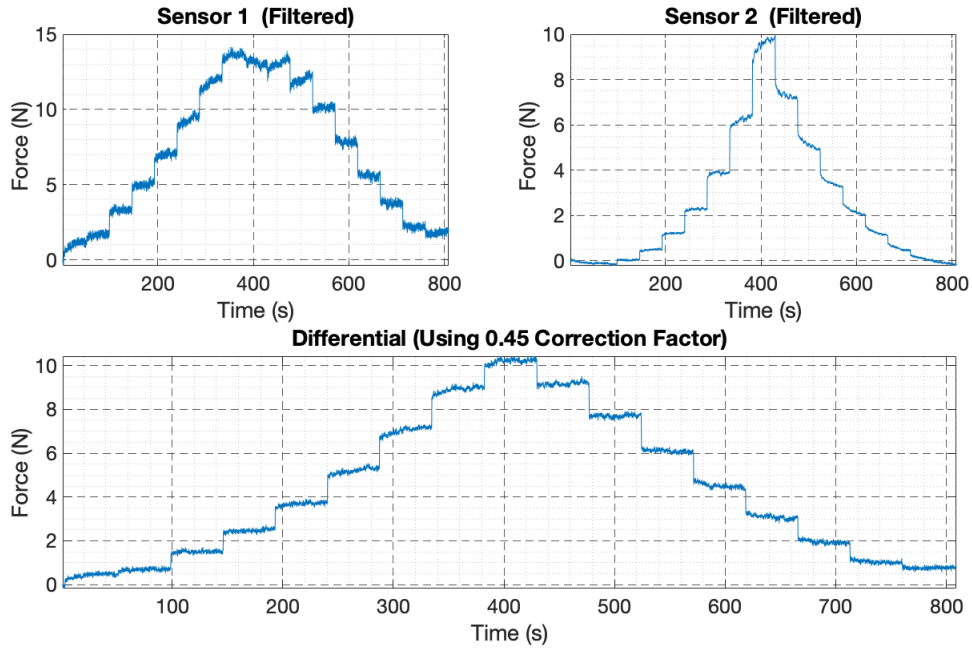

Figure 6.20: Hysteresis test

As seen from the results in Figure 6.20, there is a noticeable hysteresis in the two sensors as the obtained measurements while unloading do not have a good agreement with the loading cycle. Moreover, at the end of the unloading cycle, the measured force fails to reach the initial condition of 0 N. Also, from the differential plot, it can be observed that hysteresis is compensated to a small extent, although not the best. Furthermore, sensor 2 gives larger contributions to the differential signal than sensor 1, potentially due to the higher resistance change in compression than in tension. Again, the time delay between the tests is due to the difference in starting time. Also seen is drift in the sensor during the period of loading and unloading.

Accuracy

The accuracy of the sensor was characterised by measuring propeller thrust at a frequency cycle of 20 Hz - 90 Hz. The sensor was calibrated based on an F-T sensor and obtained measurements were then compared to the mathematical model of propeller thrust based on:

$$T = K \cdot f^2 \tag{6.12}$$

where T is the thrust , f is the frequency of the motor and K is the calibration factor. The comparison between the mathematical model and sensor is shown in Figure 6.21.

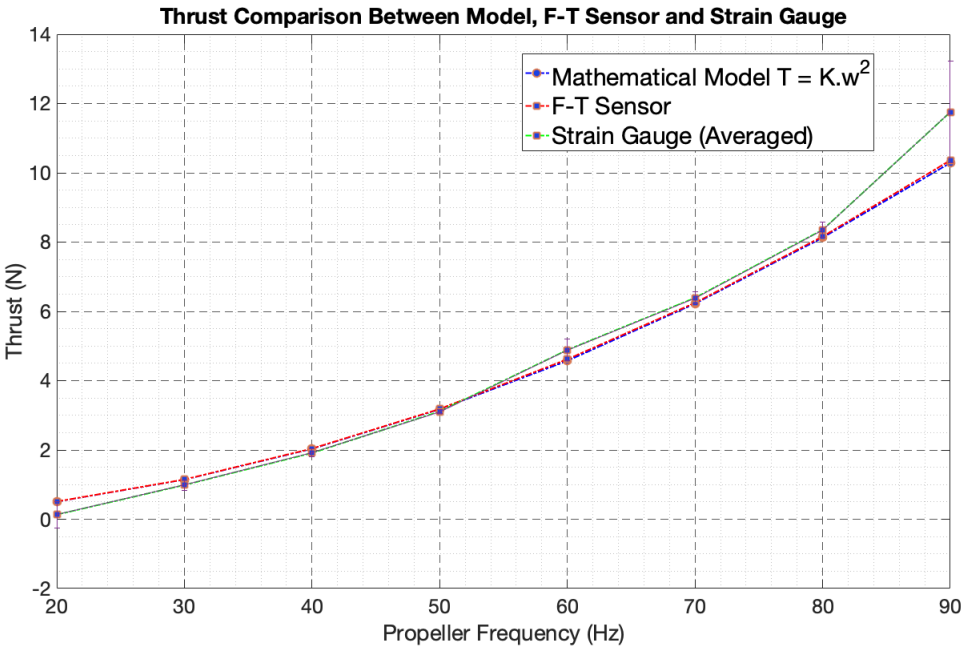

Figure 6.21: Thrust comparison

As seen from Figure 6.21, there is a good agreement between the strain gauge and the mathematical model. The calibrated sensor is able to provide accurate measurements of thrust until a frequency of 80 Hz. Also, at a frequency of 90 Hz the measured thrust is overestimated by 1.4 N.

6.3.2 Ground Effect

In this section, the performance of the sensor is characterised under the influence of the ground effect. A simple test setup is used in close proximity to the ground. The distance from the ground is increased in steps and the performance of the sensor is checked for these distances i.e. if the sensor can measure the increase in thrust due to the influence of the ground.

Modelling Of Ground Effect

The ground effect experienced by helicopters has been modelled using a PFI model (Potential flow with the method of images). This model involves using the method of images and potential flow containing a single source that models the airflow of the rotor. This model has been widely used due to its simplicity and accurate representation of the relationship between the thrust in ground effect and the height of the rotor to the ground [59].

In the Cheeseman model of the ground effect [60], the thrust ratio T_{ratio} is a function of radius of the rotor R and distance from the ground z, given by the equation:

$$T_{\text{ratio}} = \frac{T_{\text{IGE}}}{T_{\text{OGE}}} = \frac{1}{1-(R/4z)^2} \tag{6.13}$$

The condition of z/R > 0.25 must be satisfied to use the cheeseman model [60] . Here T_{IGE} is the thrust in ground effect, T_{OGE} is the thrust out of ground effect, R is the radius of the rotor and z is the distance of the rotor to the ground plane. Figure 6.22 shows the Cheeseman model for a 13 inch propeller. A clear increase in thrust ratio is seen as the ratio z/R decreases.

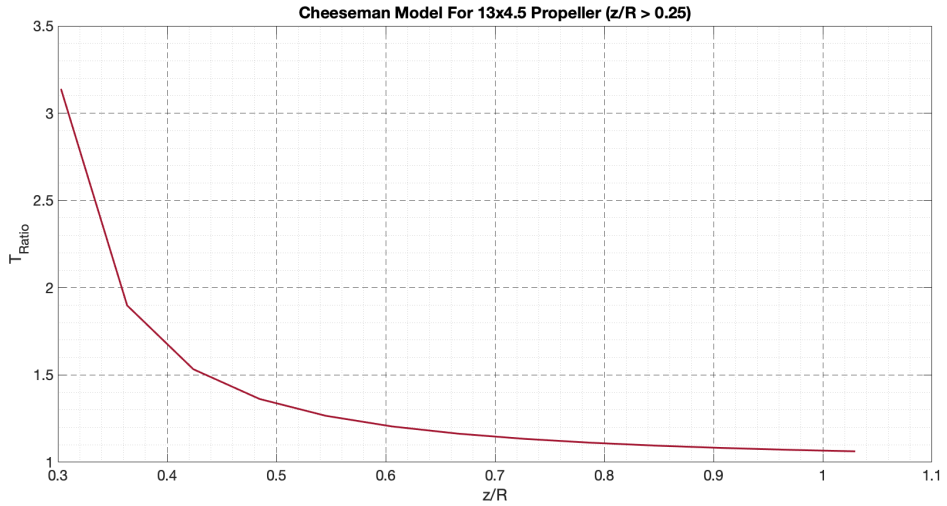

Figure 6.22: Cheeseman model depicting the relation between Thrust ratio and z/R for a 13 inch propeller with a pitch of 4.5

Measurement Protocol

To characterise ground effect, the drone arm is placed at a starting distance of 50 mm from the ground up till 210 mm in steps of 20 mm. For every distance, the motor commands are sent via the ESC to the motor using a Matlab script. The frequency of the motor is limited to a frequency cycle of 30 Hz - 60 Hz to avoid causing any damage to the drone arm under the influence of the ground effect. The sensor measures the thrust of the motor for every distance from the ground. The output voltage is converted to thrust based on calibration equations discussed earlier in Section 6.1.1. There were no provisions made to mount the F-T sensor on the drone arm. Hence, the experiments had to be conducted separately, first with the motor mounted on the F-T sensor and then with the drone arm. The two setups are shown in Figure 6.23

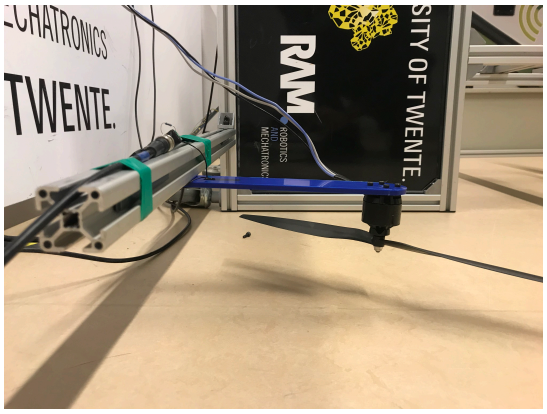

(a) Motor-propeller assembly on the drone arm

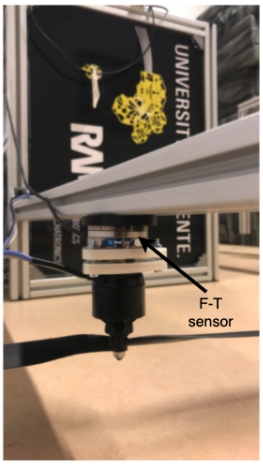

(b) Motor-propeller assembly mounted on the F-T sensor

Figure 6.23: Separate ground effect setups comprising of drone arm and F-T sensor

Results

The results in Figure 6.24 describe the influence of ground effect for a 13 inch propeller and the standard deviation is shown by the error bars. The effect of the ground is evaluated based on thrust ratio as a function of distance from the ground z. Tests are performed at various distances from the ground, starting at a distance of 50 mm or z/R ratio of 0.3 based on Equation 6.13. The distance is increased in steps of 20 mm until a distance of 210 mm from the ground or z/R ratio of 1.27. Each of these distances is measured from the ground to the propeller plane. Cheeseman Model is then validated using a printed strain gauge and a force-torque sensor. The experiment was conducted at a certain distance for a motor frequency ranging from 20 Hz - 60 Hz from which the average thrust ratio was obtained and plotted against z/R.

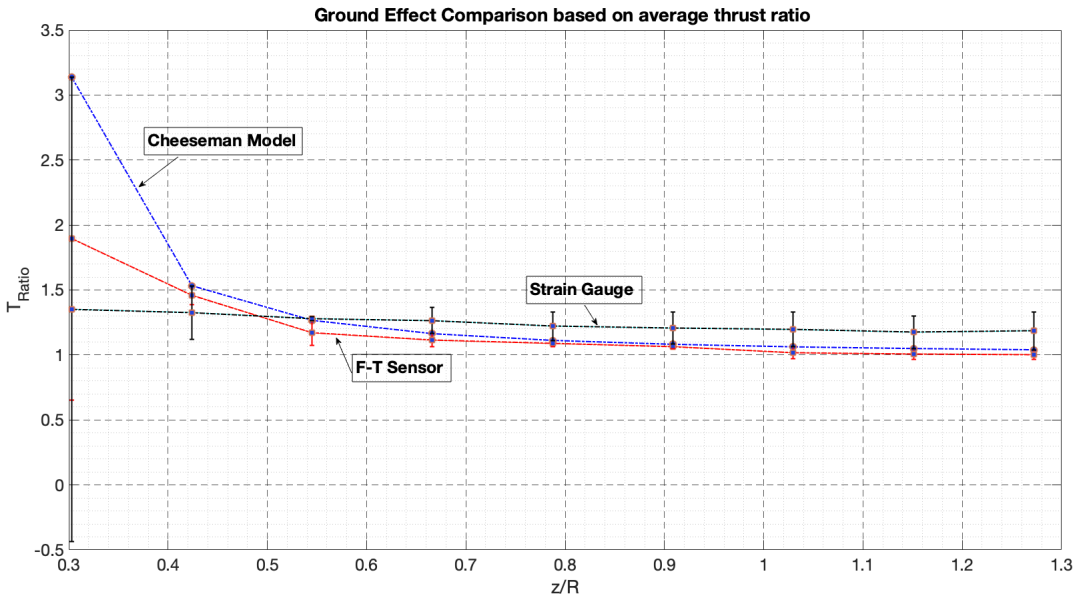

Figure 6.24: Cheeseman model validated using F-T sensor and printed strain gauge

As seen from strain gauge measurements in Figure 6.24, there is a significant increase in thrust when the rotor is in close proximity to the ground. It is also seen that the influence of the ground effect is negligible beyond z/R of 1.02 where the T_{ratio} is 1. When the propeller is in the range of 70 mm - 210 mm from the ground, both the F-T sensor and the printed strain gauge show a good correlation with the Cheeseman model, although not perfect. However, at a distance of 5 cm from the ground, there is a discrepancy between the sensors and the model. The influence of motor frequency on ground effect was also checked for a series of distance ranging from 50 mm - 170 mm. Figure 6.25 shows the measured thrust ratio by the strain gauge for different frequencies at different distances from the ground.

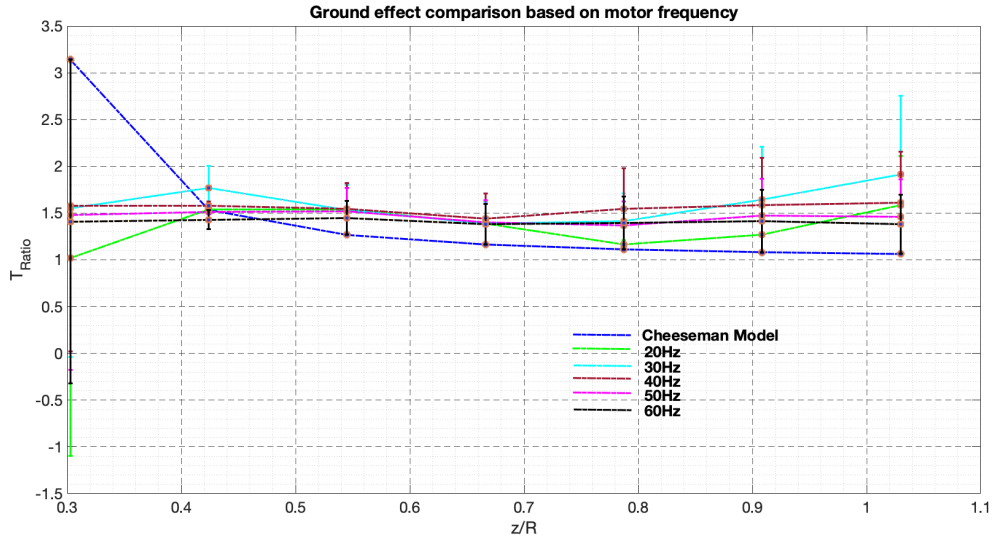

Figure 6.25: Thrust ratio based on motor frequency

From Figure 6.25, it can be seen that the largest error is at ground effect distance of 50 mm for the complete range of motor frequency. At 20 Hz, the measured T_{ratio} is 1, indicating no ground effect. The measured thrust ratio at 40 Hz - 60 Hz seems to follow the same trend throughout the range of distance.

It is interesting to see the Cheeseman model which is used in helicopters, is also able to predict the influence of ground in single rotors. However, some discrepancies are observed between the model and the sensor. This could be due to the limitations of the model:

- The Cheeseman model is based on inviscid potential flow which deals with high Reynolds number whereas a single rotor works at relatively low Reynolds number [61].
- The model does not take into account the effect of propeller pitch on thrust ratio.

Nevertheless, the model is able to provide an estimation of thrust in ground effect. The discrepancy between the strain gauge and the model could be due to various reasons. This is analysed in the next section.

6.3.3 Effect Of Drone Arm Deflection On Ground Effect

Due to the flexibility of the drone arm, it was important to analyse the effect of arm deflection on ground effect. The drone arm can deflect based on the magnitude of thrust produced in ground effect. This deflection can cause the thrust vector to tilt, thereby increasing the distance between the propeller plane and the ground as shown in the free-body diagram in Figure 6.26. F_{normal} is the actual thrust vector for a rigid beam. Any deflection of the beam causes a deflection of the thrust vector $F_{\text{deflected}}$.

This increase in distance, although small at a low motor frequency, can affect the ground thrust approximation significantly. In Figure 6.27, the left plot (a) shows the nominal thrust vector at 15 Hz at a distance of 50 mm from the ground. The right plot (b) in Figure 6.27 shows the deflection of the thrust vector at 60 Hz due to the flexibility of the beam.

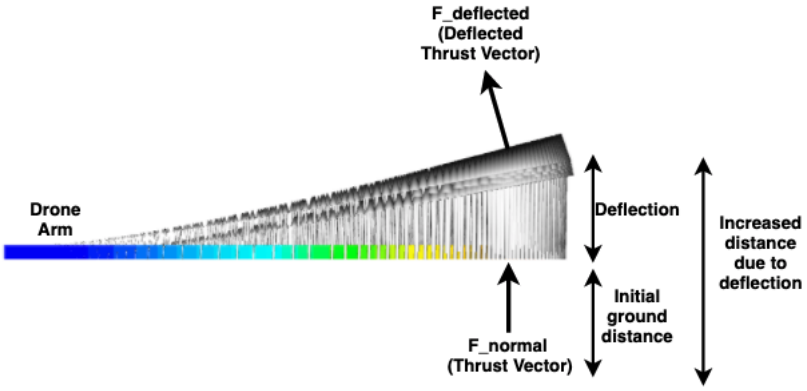

Figure 6.26: Effect of drone arm deflection when subjected to ground effect: F_{normal} is the thrust vector for a rigid beam. $F_{\text{deflected}}$ is the deflected thrust vector. An increase in ground effect distance is seen due to arm deflection

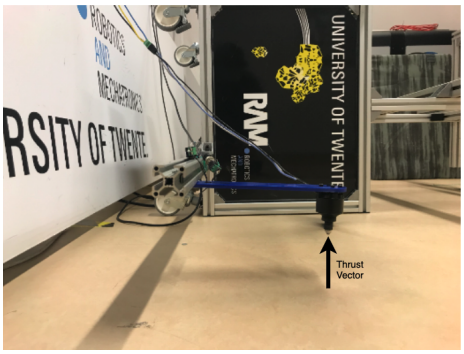

(a) Nominal thrust vector at 15 Hz.

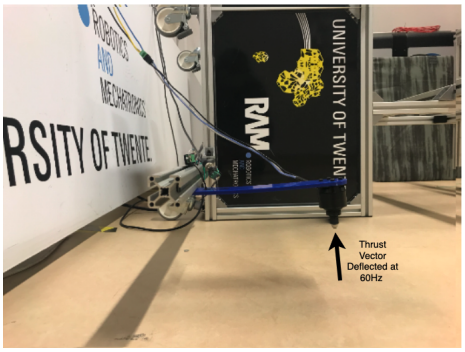

(b) Deflection of thrust vector at 60 Hz motor frequency. The propeller plane is at a distance of 50 mm from the ground

Figure 6.27: Deflection of drone arm causing the thrust vector to deflect, thereby affecting the distance from the ground

The measurement protocol is as follows:

First, The initial distance from the ground to the propeller plane was first measured. Next, the deflection δ of the arm was calculated based on the measured thrust by the sensor, using:

$$\delta = \frac{FL^3}{3EI} \tag{6.14}$$

where F is the measured thrust, E is Young's modulus of the material, the moment of inertia is given by I and L is the distance from the sensor to the motor axis.

Now, the new distance from the ground is the initial distance plus the deflection δ. Based on this adjusted distance, a new z/R ratio is obtained and the thrust ratio based on the Cheeseman model is calculated and compared to measurements from the F-T sensor and Strain gauge. The same setup from Figure 6.23 is used.

Results

At higher motor frequency, the deflection of the drone arm increases due to the magnitude of thrust produced. The experiments were conducted at a motor frequency range of 30 Hz - 60 Hz to evaluate the influence of deflection on thrust ratio. An F-T sensor was again used to validate

the sensor measurements and the Cheeseman Model. Results from the ground effect experiments are shown below in Figure 6.28:

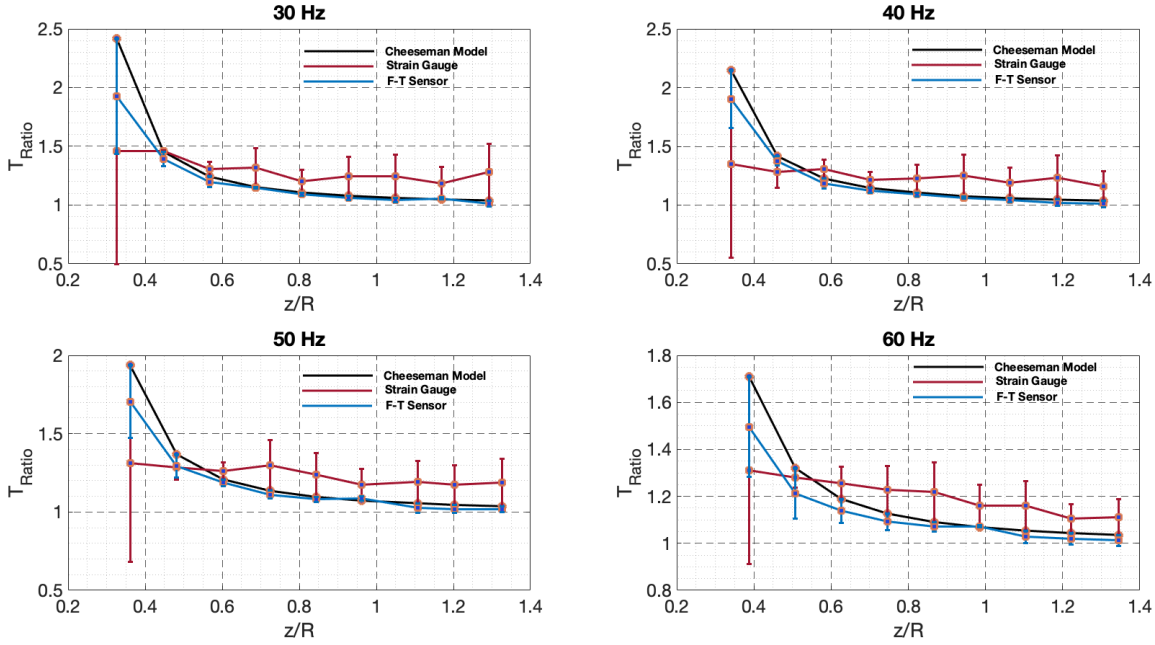

Figure 6.28: Influence of ground effect when drone arm deflection is considered

Clearly seen is the improved agreement between the F-T sensor and the Cheeseman model in Figure 6.28. However, for all motor frequencies, the error bar for the F-T sensor is the largest when the propeller is at a distance of 50 mm from the ground or a z/R ratio of 0.326. Nevertheless, the inclusion of drone arm deflection for calculating the new z/R ratio does affect the modelled thrust ratio.

Also, there is a major difference in measurements obtained with the F-T sensor and the strain gauge although the strain gauge was calibrated. This could be attributed to the way the F-T sensor was mounted independently on the test setup beam and not on the drone arm. Another potential cause could be that the natural frequency of the beam is excited easily. This is analysed in the next section.

Modal Analysis

To investigate the effect of natural frequency on the drone arm, modal analysis was performed using Simscale (SimScale GmbH, Germany). The effect of motor weight was also considered.

The following boundary conditions were applied for modal analysis (Figure 6.29):

- Fixed support on the left side of the drone arm (To replicate fixture on the test setup)
- Displacement constraint for the screws
- Weight of the motor 1.225 N

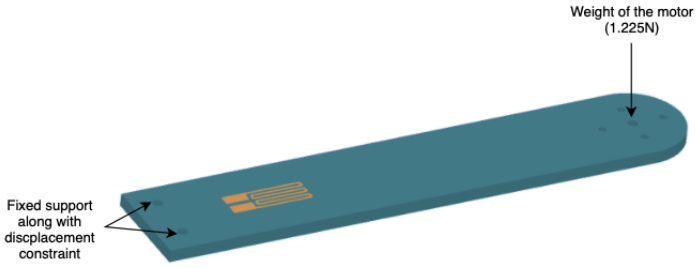

Figure 6.29: Boundary conditions applied to the drone arm

Figure 6.30 shows the first modal frequency of the drone arm.

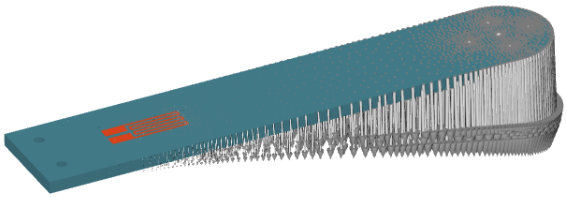

Figure 6.30: Modal frequency of the drone arm with motor weight included: The first mode has a frequency of 36.02 Hz

The first mode has a frequency of 36.02 Hz whereas the frequency of the motor is in the range of 20 Hz - 90 Hz. The condition of resonance is reached when the motor frequency equates to the natural frequency of the beam. However, this does not convey that the resonance has no effect when the motor frequency is lower or higher than natural frequency.

The beam acts like a mass-spring system as shown in Figure 6.31 with stiffness C. F_{normal} is the actual thrust vector for a rigid beam. However, this is not the case for the flexible drone arm. Any deflection of the beam causes the deflection of the thrust vector to $F_{\text{deflected}}$

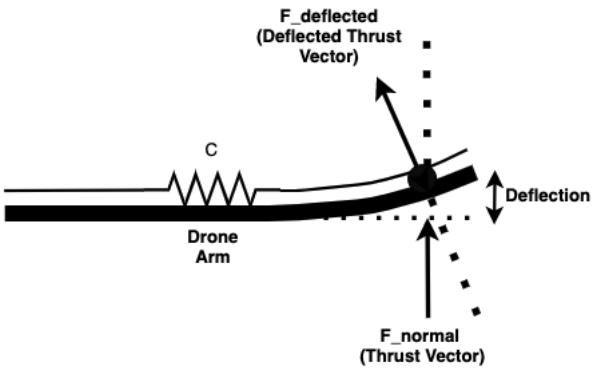

Figure 6.31: Free-body diagram of the drone arm deflection in close proximity to the ground , representing a mass-spring system

Theoretically, when the mass at the tip is much larger than the mass of the beam, the natural frequency of such a system can also be calculated as:

$$\omega_0 = \sqrt{\frac{C}{m}} \tag{6.15}$$

where mass is denoted by m and C is the bending stiffness of the beam.

The stiffness of the beam can be calculated as:

$$C = \frac{\text{Force}}{\text{Deflection}} \tag{6.16}$$

The bending stiffness of the beam was found to be 424.7 $\mathrm{N\,m^{-1}}$. Now, from Equation 6.15, with bending stiffness and mass known (0.125 kg), the natural frequency of the system is found to be 9.28 Hz. There is a significant difference of 26.7 Hz between the theoretical natural frequency and the one determined using the finite element method (FEM). This could possibly be due to the consideration of boundary conditions while the theoretical Equation 6.15 only considers the mass and stiffness of the beam assuming it is a single degree of freedom (SDOF) system.

It's also expected that the inertia plays a role in the natural frequency of the system as reported by [62] where the natural frequency was smaller when a mass was attached to it than without. There could be a better agreement between the theoretical natural frequency and FEM obtained frequency if the effect of inertia is considered.

In terms of vibration, the effect of natural frequency can be explained based on transmissibility, defined as the amplitude of vibration on a structure. Transmissibility is given by:

$$T = \frac{1}{(1-(w/W_0)^2)} \tag{6.17}$$

Where W_o is the natural frequency of the system and w is the input frequency i.e. the motor frequency in our case. Based on the estimated natural frequency of the system W_o and motor frequency w, the vibrations on the beam can be represented by a graph of transmissibility against frequency ratio as shown in Figure 6.32. The motor frequency is in the range of 15 Hz to 90 Hz.

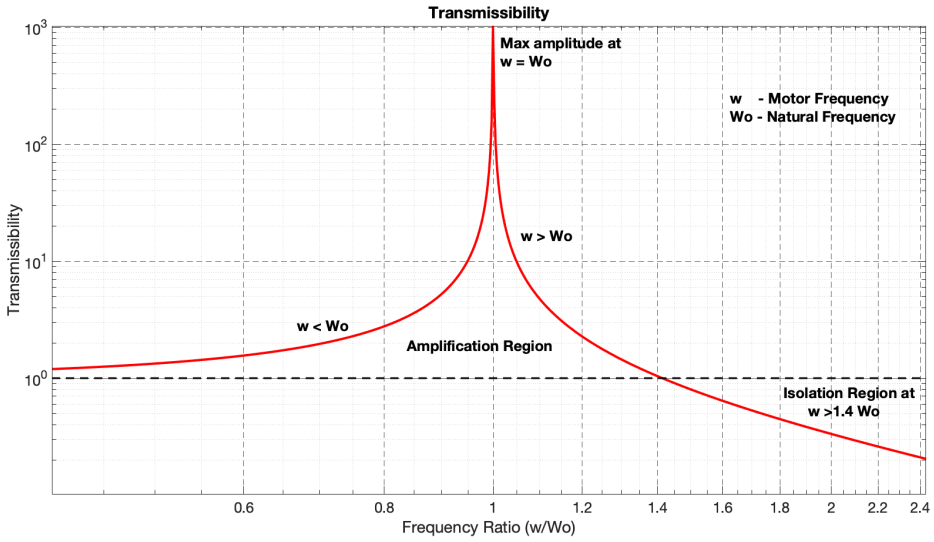

Figure 6.32: Amplitude of vibration based on the frequency ratio (w/W_o)

From Figure 6.32, it can be clearly seen that, at $w < W_o$, the amplitude of vibration builds up as it progresses towards the condition of resonance. At $w = W_o$, the amplitude of vibration is at its maximum. As the motor frequency further increases, the amplitude is reduced and it further drops below 0 at a frequency ratio of 1.4. This is the isolation region where vibrations have minimal effect on the system. The same also applies to the deduced theoretical natural frequency of 9.28 Hz except that the amplitude of vibration would be much smaller at $w = W_o$. As the motor frequency is the range of 15 Hz - 90 Hz, the condition of resonance might not be reached but some vibrations may still be present. Overall, it is interesting to see how vibrations can still exist on the beam outside the resonance condition and these vibrations could affect the obtained measurements by adding noise to the system.

6.4 Conclusion

Two experimental setups comprising of the linear actuator and motor setup were discussed and the sensor was characterised successfully. The sensor under tension was found to be more non-linear than the one in compression. The gauge factor of the two sensors was deduced. Also, the obtained sensor measurements were found to be repeatable. The hysteretic response was clearly seen with both setups. However, the hysteresis was much larger when the motor was used. The bandwidth of the sensor was found to be 1 Hz. The sensor was also characterised for ground effect and the influence of the ground was clearly seen in the extra thrust measured by both the strain gauge and F-T sensor. Despite the limitations of the Cheeseman model, it was able to provide an estimation of thrust in ground effect for an isolated rotor as seen in F-T sensor measurements. However, this was not the case for the printed sensor.

7 Controller

As seen previously, the drone arm is susceptible to a sudden increase in thrust in ground effect. Therefore, this chapter proposes a control architecture based on sensor feedback that attempts to control the thrust produced in ground effect and nullifying the effects of the same.

First, the controller hardware/software is discussed followed by a brief discussion of the controller objectives. Also, discussed are different types of controllers. A comparison is made between them to choose a desirable controller for the ground effect application. Next, the two commonly used control schemes are presented: feedback control and feed forward control.

Finally, an overview of the designed controller architecture is presented, followed by an analysis of certain parameters of the controller. The controller is then tested in ground effect and results are presented with a discussion. Finally, conclusions are made.

7.1 Instrumentation

The controller is designed and implemented in SIMULINK (Mathworks Inc., USA). The sensors are connected individually in a voltage divider configuration on a breadboard and data is read by an Arduino Mega. To improve the resolution, a 16-bit ADC is used. The feedback signals from the Arduino are incorporated in the controller architecture using the Arduino-SIMULINK Interface. Once again, the closed-loop speed controller developed by Franchi et. al [58] is used. A genomix package is used to send motor commands from SIMULINK to the motor.

7.2 Controller Architecture

In this section, the controller objectives are first discussed followed by different controllers such as: Proportional controller, Proportional Integral controller and Proportional Integral Derivative controller. Next, types of controller architectures are designed, followed by an overview of the controller. Finally, the designed controller is presented.

7.2.1 Controller objectives

The objective of the controller is to compensate for increase in thrust when the propeller is in close proximity to the ground. Besides this, other objectives are:

- Determining the type of controller to use
- Type of controller scheme to adopt: Feed forward control or feedback control or a combination of both.
- Tuning the parameters of the controller to achieve the desired response (set-point tracking)

7.2.2 Different Controllers

In this section, different types of controllers are discussed: mainly Proportional controller (P) , Proportional-Integral controller (PI) and Proportional-Integral-Derivative controller (PID).

Proportional controller (P)

As the name suggests, the controller only contains a proportional term with gain K_p. The block diagram of a proportional controller is shown in Figure 7.1. The output of the controller is given by:

$$u(t) = K_p e(t) \tag{7.1}$$

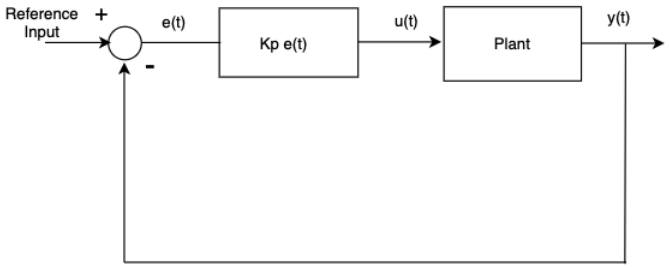

Figure 7.1: A proportional controller in a closed loop system

In a proportional controller, gain K_p only works on the error between the reference and the measured quantity. Although it is simple to tune, there can be offset error over time and this can affect the stability of the system.

Proportional-Integral controller (PI)

With the addition of the integral term to the proportional controller, the output of such a controller is given by [63]:

$$u(t) = K_p e(t) + K_i \int e(t)dt \tag{7.2}$$

Figure 7.2 shows a closed loop system with the proportional-integral controller.

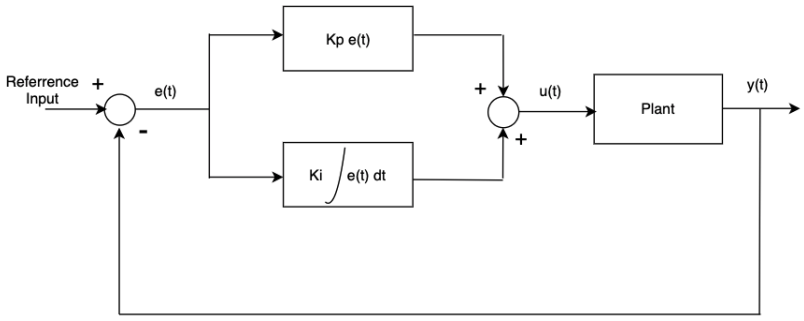

Figure 7.2: A proportional-integral controller in a closed loop system

In Figure 7.2, $e(t)$ is the error signal, $u(t)$ is the output of the controller fed to the plant and $y(t)$ is the output of the plant. Also, K_p and K_i are the gains of the proportional and integral controller respectively. In a PI controller, the proportional term works on the error between the reference and the measured quantity for interval of time t. The integral controller on the other hand eliminates the offset by continually integrating the error over time.

Proportional-Integral-Derivative controller (PID

The working of PID controller is similar to that of a PI controller except the addition of a derivative term as shown in Figure 7.3. A PID controller produces an output given by [63]:

$$u(t) = K_p e(t) + K_i \int e(t)dt + K_d \frac{de(t)}{dt} \tag{7.3}$$

The function of the derivative term is to predict the error signal behaviour and correct this on the basis of rate of change of the signal over time [63].

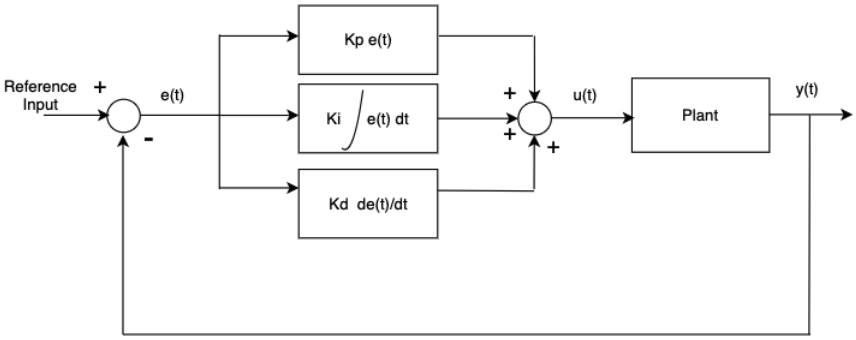

Figure 7.3: A proportional-integral-derivative controller in a closed loop system

Comparison between P, PI and PID controller

A comparison between the three controllers is provided in Table 7.1

P Controller	PI Controller	PID Controller
Simple to Tune	Tuning is more complicated	Tuning is most complicated
Development of offset with increased disturbance	There is no offset due to integral action	No offset
Less effective due to offset	Effective compared to P controller	Most effective
A high proportional gain can cause noise amplification	Less noise amplification compared to PID	Derivative term can amplify noise [64]

Table 7.1: Comparison between P, PI and PID controller

As seen in Table 7.1, a proportional (P) controller although simple can have offset error over time with increase in disturbance and this makes it less effective when compared to PI and PID controller. In the case of PI and PID controller, a similarity is that the integral action takes care of the offset and eliminates it. The addition of the derivative term in the PID controller makes it the most complicated to tune despite being the most effective amongst P and PI controller. In our application, the PI controller would suffice as only two parameters will have to be tuned for a non-linear system response. and a closed-loop control can be achieved while reducing the steady-state error (due to ground effect) as in the case of our application.

7.2.3 Control Schemes

Two commonly used controller schemes are discussed: Feedback control and feed forward control.

Feed forward control

In the case of the feed forward control, the disturbance is measured and the controller accounts for r this disturbances and rejects it before they impact the system [65]. Figure 7.4 shows the block diagram of a feed forward controller architecture.

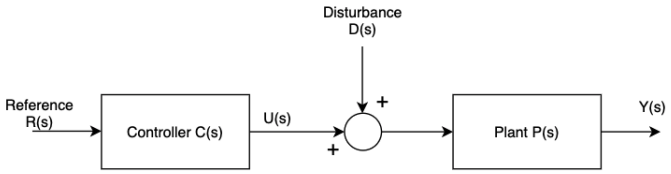

Figure 7.4: Feed forward controller architecture

From Figure 7.4,

$$U(s) = C(s) \cdot R(s) \tag{7.4}$$

After rejecting the disturbances, the plant output $Y(s)$ is given by:

$$Y(s) = P(s) \cdot C(s) \cdot R(s) \tag{7.5}$$

The design approach of such a controller is that the feed forward controller $C(s)$ is equated to the inverse of the plant $P(s)$ assuming the reference input $R(s)$ = plant output $Y(s)$ as [66]:

$$C(s) = \frac{1}{P(s)} \tag{7.6}$$

The disadvantage of such a controller architecture is that not all disturbances are measured and the approach may not be robust unless combined with feedback control. When combined, the controller architecture compensates both measured disturbances as well as other disturbances [65]. This is discussed in the next section.

Combination of feed forward and feedback control

In feedback control, the controller compares the reference point to the controlled variable and calculates the error, applied as a feedback to produce a control action that attempts to bring the controller variable to the reference point, thus eliminating the error. This control action is repeated until the error is completely eliminated. Figure 7.5 shows the block diagram of the combined control architecture where $E(s)$ is the error signal.

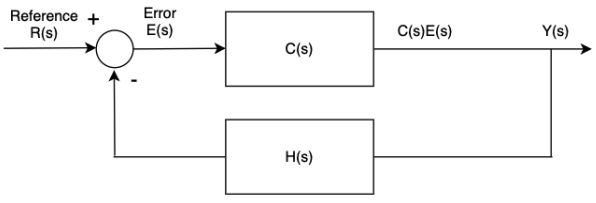

Figure 7.5: Combination of feed forward and feedback control

From Figure 7.5,

$$Y(s) = C(s) \cdot E(s) \tag{7.7}$$

The error $E(s)$ is calculated as:

$$E(s) = R(s) - H(s) \cdot Y(s) \tag{7.8}$$

Substituting $E(s)$ in 7.7,

$$Y(s) = C(s)(R(s) - H(s) \cdot Y(s)) \tag{7.9}$$

Rearranging the terms:

$$\frac{Y(s)}{R(s)} = \frac{C(s)}{1 + (C(s)H(s))} \tag{7.10}$$

where the transfer function for feed forward and feedback is given by $C(s)$ and $H(s)$ respectively. Hence, all the disturbances are accounted for with this combination. Therefore, in our application, this combination of controller architecture will be applied.

7.2.4 Controller Overview

With the type of controller and control scheme chosen, an overview of the designed controller architecture can now be presented as shown in Figure 7.6.

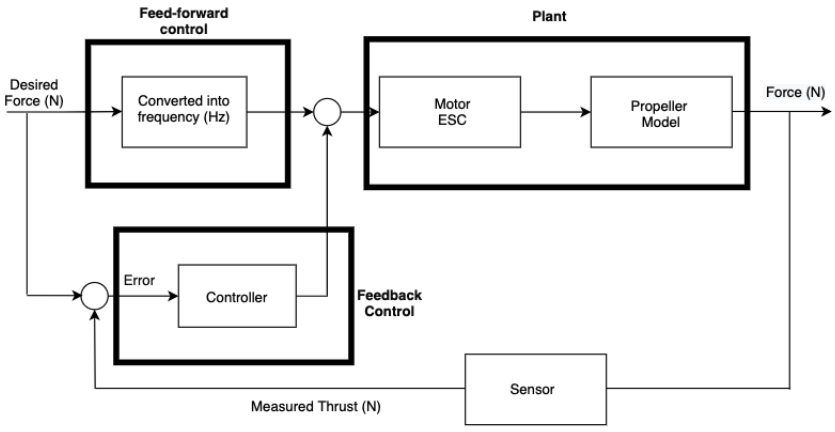

Figure 7.6: An overview of the controller architecture comprising of feedforward control in combination with feedback control

The designed controller as seen in Figure 7.6 is modelled in SIMULINK (Mathworks Inc., USA). The working of the controller is as follows: the input to the controller is the desired/reference thrust that is converted into frequency f based on the simple mathematical model of Thrust:

$$f = \sqrt{\frac{T}{K}} \tag{7.11}$$

where T is the Thrust and K is the calibration factor of the motor. This serves as the feed-forward term fed into the summation block. Also, the desired/reference thrust is fed into another summation block along with feedback signals from the sensor i.e. thrust value in this case. The sensor measurements are filtered using an analog filter design block consisting of a 2^{nd} order Butterworth low-pass filter with 5 Hz cut-off frequency. The error between the sensor output and reference thrust is then calculated and fed into a PI controller with saturation limits on integral response.

When tuned, the PI controller works on the error and feeds it back to the summation block that includes the feedforward. The final output i.e. the sum of feed-forward and feedback control is then fed into the ESC using a genomix package [58] which communicates with the motor. The

ESC then causes the motor to rotate at the desired frequency. This way, the controller helps in generating the required thrust while reducing the ground effect.

Measurement Protocol

First, the propeller is placed in close proximity to the ground. Initially, the propeller plane is a distance of 50 mm from the ground. The distance is increased in steps of 20 mm until 150 mm.The frequency of the motor is once again limited to a frequency cycle of 30 Hz - 60 Hz to avoid causing any damage to the drone arm under the influence of ground effect. Reference thrust is first set and the controller is run for 5 s and the response of the controller is observed.

7.3 PI Tuning

To obtain the desired response, it is important to tune the controller. The controller can either be tuned manually or using the auto-tuner app on SIMULINK. Due to the non-linear response of the system, a manual yet simple procedure was used, although iterative.

Proportional Controller

The manual procedure involves tuning K_p first while keeping K_i as zero. The gain value of K_p is increased in steps until the system starts to oscillate. This isn't the final value of K_p as this only indicates the range of the set gain value. Also, the response of K_p only depends on the error between the reference and the feedback. The effect of increasing gain values of K_p is seen in Figure 7.7

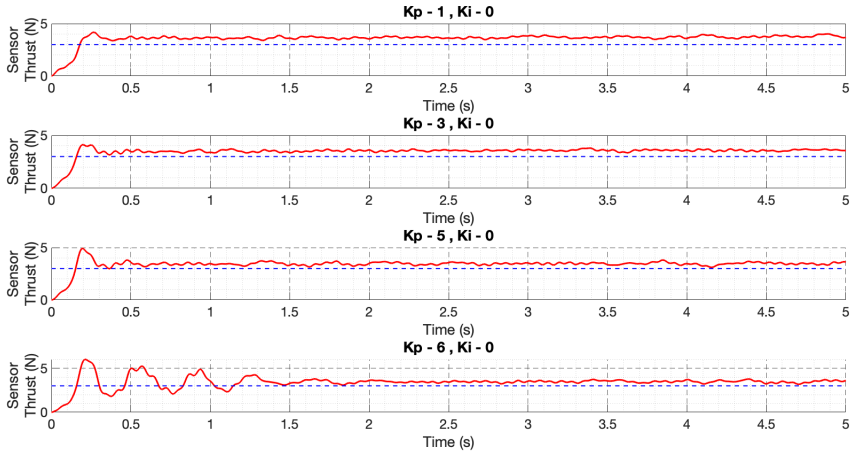

Figure 7.7: Effect of K_p on controller response: thrust measured by the sensor is plotted against time.

Figure 7.7 clearly shows the effect of increasing the gain value. With K_p = 1 , there is no overshoot. A slightly higher overshoot is seen when the gain value of K_p is increased to 3. As this gain value is further increased, the system tends to overshoot further at K_p = 5. A K_p gain of 6 causes the system to oscillate, indicating the gain value is too large. Increasing this gain value further can cause the system to be unstable, causing oscillations beyond control. Once the system starts to oscillate at this gain value, the K_p gain value of 6 is then halved. Therefore, the final value of the K_p is 3.

The step response characteristics for the gain values are shown in Table 7.2

	Kp = 1	**Kp = 3**	**Kp = 5**	**Kp = 6**
Rise time (s)	0.1594	0.1255	0.1215	0.1180
Settling time (s)	4.9583	4.9506	4.9642	4.9882
Overshoot (%)	13.2	15.8894	35.7	66.84
Peak	4.1772	4.1259	4.9144	6.0196
Peak time (s)	0.27	0.2	0.2	0.21

Table 7.2: Step response characteristics for K_p gain values

Integral Controller

The process of tuning the integral term is the same as the method discussed above. After a desired K_p is obtained, the gain value of K_i can then be tuned to achieve the desired system response i.e. the measured thrust tracks the reference thrust with minimal error. The integral controller works on the steady-state error until it reaches 0. The effect of increasing gain values of K_i is seen in Figure 7.8

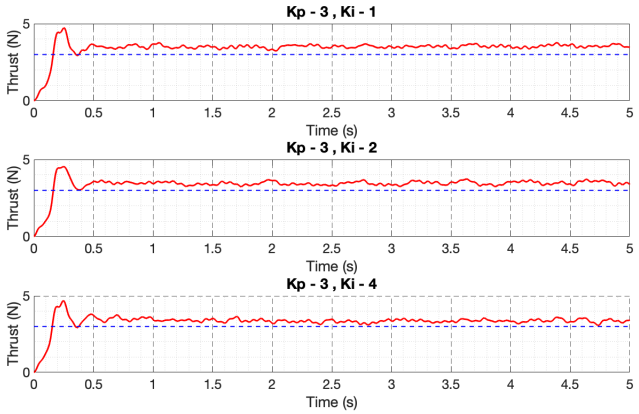

Figure 7.8: Effect of K_i on controller response

From Figure 7.8, keeping K_p constant and varying K_i, it can be seen that the response of the system changes. At K_i = 4 , small oscillations are seen , starting at 0.5 s. The same K_p tuning procedure is again followed. The gain value of K_i is then halved i.e. the final K_i is 2.

The step response characteristics for the gain values are shown in Table 7.3

	Ki = 1	**Ki = 2**	**Ki = 4**
Rise time (s)	0.13	0.1378	0.1274
Settling time (s)	4.94	4.98	4.96
Overshoot (%)	36.81	34.4	37.42
Peak	4.7322	4.544	4.69
Peak time (s)	0.25	0.25	0.25

Table 7.3: Step response characteristics for K_i gain values

Effect of Integral Saturation Limits on Controller Response

As discussed earlier, an integral controller works on the steady-state error. The response of the integral term can change over time until the system is stabilised. However, in some cases, the integral action can accumulate a large error during the rise time, in turn causing an overshoot and the integral action continues to increase [67, 68]. However, this behaviour was not seen in Figure 7.8, while tuning K_i. This is because the response of the integral was saturated to avoid

the continuous accumulation of error which can change the system response over time. With K_p and K_i tuned, the effect of the integral saturation limit was then investigated.

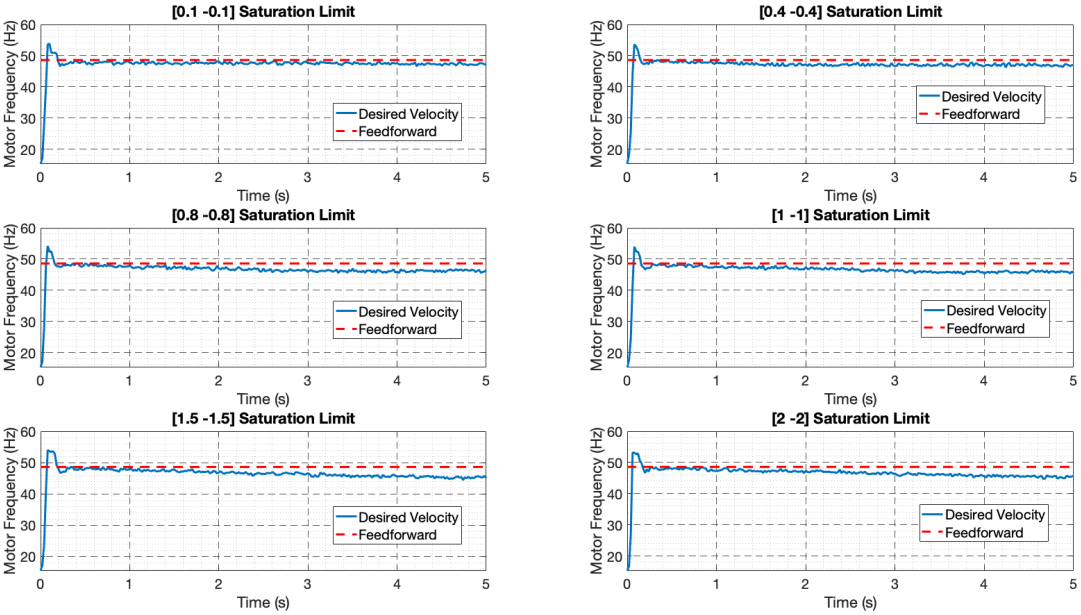

Figure 7.9: Effect of integral saturation limit

Figure 7.9 shows the influence of saturation limit on desired motor frequency (Hz) in comparison to a feed-forward frequency of 48.6 Hz, that corresponds to a 3 N reference thrust. With the response of the integral controller saturated to [0.1 -0.1], the desired rotor frequency has a good correlation with the feed-forward frequency, indicated by the dotted red line. As this saturation limit is increased to [0.4 -0.4], the frequency begins to slightly deviate at 1 s. The effect of saturation is further seen as the limit is increased. It can be observed that as the saturation limit is further increased to [2 -2], the deviation is much larger. Finally, when the integral response is saturated in the [0.1 -0.1] range, a stable system response is achieved.

Finally, the tuned controller has the following parameters: K_p = 3 , K_i = 2 and integral saturation limit in the range of [0.1 -0.1]

7.4 Results

The tuned controller is now validated for robustness and implementation in ground effect. The same motor and propeller combination was chosen and the experimental setup is the same as Figure 6.23. The controller is first tested at 50 mm from the ground and the distance is increased in steps of 20 mm until a distance of 150 mm. The distance is measured from the ground to the propeller plane. Also, the chosen propeller is spinning in the clockwise direction. Data is sampled at 128 Hz. Figure 7.10 and 7.11 report the results obtained with the designed controller.

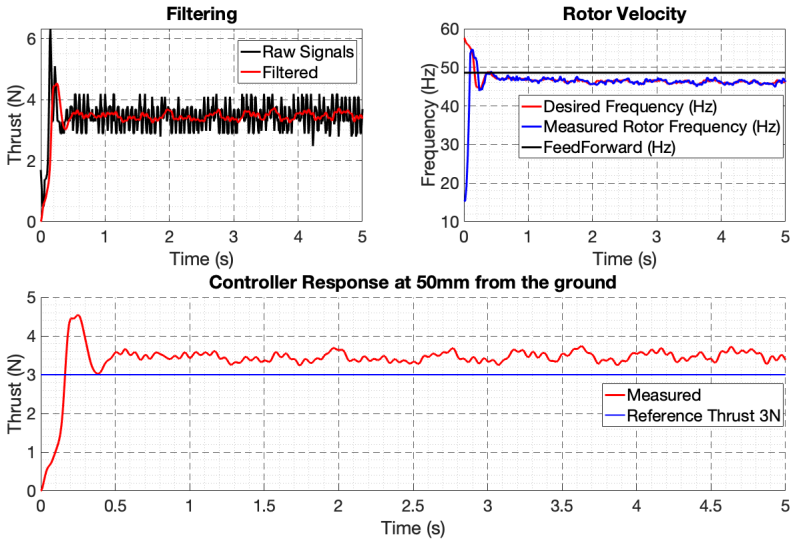

Figure 7.10: Controller response at 50 mm from the ground

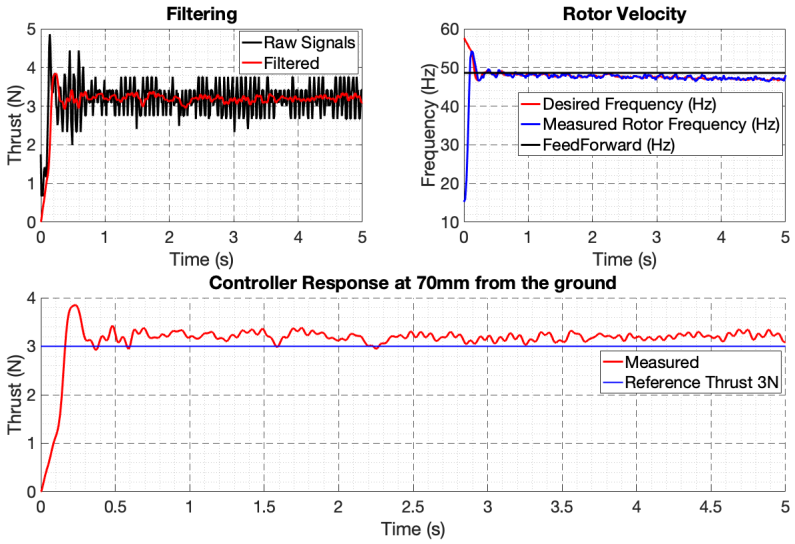

Figure 7.11: Controller response at 70 mm from the ground

The top left plot in Figure 7.10 and 7.11 shows the raw sensor signals that act as feedback. Due to the noise present in the sensor signals, a low-pass filter having a cut-off frequency of 5 Hz was used. The plot on the right shows a measure of motor frequency (Hz) over time. The black line indicates the feedforward frequency (Hz) based on the reference thrust whereas the red line indicates the desired frequency (Hz) based on the output of the controller. The final measured frequency is denoted by the blue line. It can be seen that at 0 s, the frequency starts at 15 Hz. This is due to the minimum frequency set for the motor used.

Also seen in Figure 7.10 and 7.11 is the good correlation between the desired frequency and measured frequency. Furthermore, it nicely follows the feed-forward frequency until it starts to drift over time. This is common as the deviation is needed to compensate for error between the measured force and the reference force i.e. as the force increases, the motor frequency should reduce to produce smaller force and vice versa.

The bottom plot in Figure 7.10 and 7.11 shows the measure of sensor thrust. Although an overshoot is seen, it is completely normal as the controller responds to a step input. Also, the ground

effect is compensated at approximately 0.5 s for both the cases (50 mm and 70 mm). Finally, the sensor measurement follows the reference thrust of 3 N although small discrepancies are still seen possibly due to the selection of controller parameters and possible noise in the system. The controller response for other distances in the range of 90 mm - 150 mm are shown in the Appendix in Figures A.7 - A.10.

The fast-fourier transform (FFT) of the raw sensor signals from ground effect experiments at 50 mm and 70 mm are shown in Figure 7.12

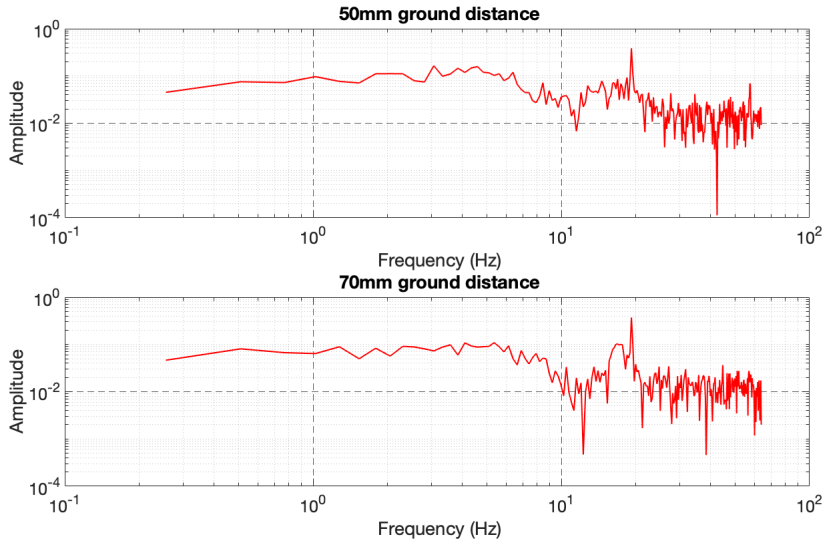

Figure 7.12: FFT of raw signals at 50 mm and 70 mm from the ground

From Figure 7.12, it can be seen that the behaviour of the signals is similar at both the distance. It is interesting to see that the first peak is at a frequency of 19.16 Hz for both the distance. The next dominant frequency is 57.74 Hz at 50 mm ground distance. However, this is not the case for 70 mm ground distance.

Analysis

While conducting a series of experiments to validate the controller, high-frequency components were seen in the raw signals. The possible reason for this could be resonance as discussed earlier in Section 6.3.3. Another reason could be the fluctuation of the motor frequency due to controller response. This was investigated by deflecting the beam manually to see if these high-frequency components exist in the absence of the motor. Figure 7.13 shows the response of the beam at different sampling frequencies and low pass filter with a cut-off frequency of 5 Hz.

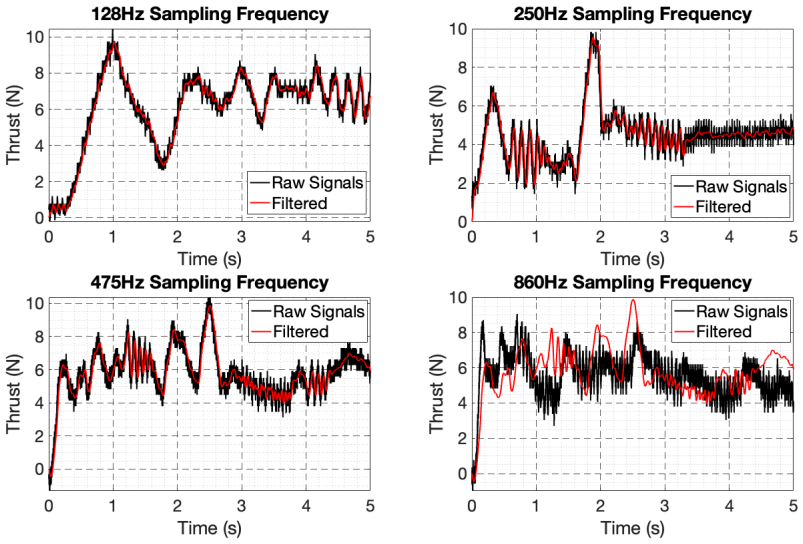

Figure 7.13: Manual deflection of the drone arm: the effect of sampling frequency is seen based on the high frequency components in the raw signals

From Figure 7.13, it can be seen that high-frequency components exist even when the beam is deflected manually. Therefore, it is not the fluctuation in motor frequency that causes this. Also, as the sampling frequency was further increased to a maximum of 860 Hz, more high-frequency components were seen. Another probable reason could be aliasing in the sensor signals. It would be ideal to use a low-pass RC filter or digital filter before performing the analog to digital conversion.

7.5 Discussion

From the experiments conducted, it can be seen that the designed controller architecture partly compensates for ground effect at a distance of 50 mm and 70 mm. Better results were obtained at other ground effect distance ranging from 90 mm - 150 mm, where the error between the reference thrust and the measured thrust was minimal, indicating the controller architecture could work but the performance of this architecture is limited, possibly due to the manual tuning approach adopted in this work. Also, the approach used to tune the saturation limits is not feasible where the limits were obtained by comparing the desired frequency to the feed-forward frequency. A better approach would be to tune this based on the controller goal i.e. to follow the reference force.

Furthermore, another tuning approach based on the pole-zero method could be adopted where the controller gains are chosen on the basis of pole-zero pattern, as described by [69]. Another possible alternative to the presented controller architecture is a cascaded controller architecture designed by [6]. Besides the control architecture, a relay-based auto tuning method can be used where optimum performance was obtained for feedback-feedforward controller architecture [70].

7.6 Conclusion

A comparison was made between P, PI and PID controller. The architecture of feed forward and feedback control was discussed. The effect of certain tuning parameters was addressed and the controller was tuned to achieve the desired response. From the obtained results, it was seen that thrust could be compensated partly at ground effect distance of 50 mm and 70 mm. Also, the performance of the controller at other distances from the ground was satisfactory with minimal error. The presence of noise in the system was also observed. Overall, the controller was able

to partly compensate for ground effect in approximately 0.5 s although some discrepancies were still seen due to the chosen controller parameters and tuning approach along with noise in the system.

8 Discussion

The applicability of integrated 3D printed sensor was demonstrated in this work. Results indicated that thrust can be computed indirectly by measuring the strain induced on the drone arm. Also, the design of the drone arm was vital to determine the range of measured thrust and sensitivity of the sensor. To reduce the weight of the drone arm, there was a need to compromise on infill density and use a 20% infill. Also, the printing time was reduced by 50% when compared to a infill density of 100%. An analysis of how different printing parameters can affect the performance of the sensor would be engaging.

In the future, the design of the drone arm could be adapted to make use of the true potential of the motor-propeller combination without limiting the frequency of the motor. Based on the dimensions of the drone arm and from FEM simulations, the sensor could only be characterised for a maximum force of 10.5 N. Beyond this force, there was a possibility of the beam approaching the limits of the design. It would be ideal to use a much thicker drone arm thereby making it possible to use larger propellers without compromising the actual potential of the motor. Also, a thicker drone arm would need a much sensitive sensor considering the deflection would be minimal with an increase in arm thickness. Connecting the sensor in a full-bridge Wheatstone circuit would make it much more sensitive to detect small changes in deflections compared to the voltage divider circuit which was used in this work.

The designed sensor was fabricated and characterised successfully to determine the non-linearity, drift and hysteresis in the sensor. Better results can be obtained if the drift and hysteretic behaviour is taken care of, for example through a model as presented by Kosmas [71]. While evaluating the feasibility of the thrust sensor using a motor setup, there was a good agreement between the measurements obtained from the three tests. However, with both the setups, hysteretic behaviour was clearly observed. Also, the calibration factor for the sensor may change over time possibly due to the conditions of the lab environment (temperature changes). Therefore, the effect of temperature on strain gauge measurements must be considered in the future. Also, the printed sensors were not annealed and this could play a role as well.

The sensor was also characterised under the influence of ground effect. The Cheeseman model was validated successfully with the F-T sensor, with some discrepancies, possibly due to limitations of the model i.e. the model is based on inviscid potential flow dealing with high Reynolds number, where the isolated rotor in our case, works at relatively low Reynolds number.

However, with the printed strain gauge, the error between the measurements was larger. This could be attributed to the way the F-T sensor was rigidly mounted and was not affected by external factors such as beam resonance. There was no provision made for the F-T sensor to be mounted on the drone arm and experiments had to be carried out separately with F-T sensor and strain gauge. In the next design of the arm, a provision will have to be made to accommodate the F-T sensor on the drone arm along with the embedded strain gauge.

Next, a controller architecture based on sensor feedback was presented. In events of ground effect, it was seen that thrust was compensated by the designed controller. At a distance of 50 mm and 70 mm from the ground, the measured thrust did not trace the reference thrust perfectly and was off by approximately 0.5 N. It is also possible that the controller will have to be much more aggressive due to the increase in thrust at these distances. Another tuning method will have to applied, for example the poles and zeros approach, discussed in [69] unlike the manual tuning method adopted in this work. The response of the controller will have to be much faster. Hence higher gains of K_p and K_i would be desirable especially at these distances although dependent on the tuning approach again.

While validating the designed controller, high-frequency components were seen in the sensor measurements. A possible reason could once again be beam resonance or aliasing in the signals or simply noise. A low-pass RC filter or a digital filter would be desirable in this case to reduce the aliasing as this noise could be limiting the bandwidth of the sensor.

9 Conclusion

In conclusion, the work presented here shows the potential of integrated 3D printed sensors in the field of drones. The research questions from Chapter 1 are assessed to see if the goals were met or not.

The first goal was: *measuring the thrust indirectly taking into account either the deflection of the drone arm or blade flapping.*

From blade flapping analysis, it was seen that the magnitude of blade deflection was quite small in the range of 2.4 mm - 4.6 mm. Also, to relate this small deflection to thrust would require complex calculations, considering the geometry of the propeller. To measure such a small deflection would require a very sensitive gauge. Moreover, it was the implementation of the sensor that posed a big challenge whereas on the other hand, it was possible to indirectly compute the thrust produced by the propeller by measuring the strain induced on the drone arm. By deducing the gauge factor of the sensor, it was possible to relate resistance change to strain and compute the thrust from strain equations for a cantilever beam i.e. the drone arm in our case.

Following this, the second goal was: *checking the feasibility of a 3D printed strain gauge for precise measurements of thrust.* It was found that the calibrated sensor was able to measure thrust accurately in the frequency range of 30 Hz - 90 Hz, using differential measurements. The obtained sensor measurements were repeatable. However, hysteresis in the sensors affected the measurements significantly. It would be ideal to have a hysteresis compensation model before implementing this on an actual drone. It was also seen that the calibration factor changed over time, possibly due to temperature changes or noise in the system.

The third goal of this work was: *to compensate sensor behaviour such as non-linearity, hysteresis and drift using differential measurements.* Using differential measurements, it was seen that drift could not be compensated. Also, differential measurements had no effect on hysteresis and non-linearity whatsoever. The exact contribution of differential measurements on sensor behaviour could not be determined from this work.

The final goal of this work was *to develop a controller architecture based on sensor-feedback taking into account the behaviour of the sensor.* The developed controller architecture was able to stabilise the thrust produced under the influence of ground effect in approximately 0.5 s. However, some uncertainties were still seen in the measurements such as an error of approximately 0.5 N at a distance of 50 mm and 70 mm from the ground. This is due to the chosen controller parameters at these distances along with noise in the system. Also, various other tuning approaches will have to be looked into as the manual approach may not be feasible.

In conclusion, it is evident that 3D printed sensors have a potential in the field of drones. Due to the advantages offered by fused deposition modelling (FDM), it is possible to adapt the sensor design to meet varying requirements. However, it is the sensor behaviour that poses a challenge and hence there is a need for further research before they can be implemented.

Recommendation For Future Work

In the future, it would be interesting to see the integration of the sensors on an actual drone and the response of such sensors in a wind tunnel, at a different velocity as this would replicate actual flying conditions. The effect of drag must also be considered to see if the sensor measurements would be affected by this.

Bibliography

[1] G. Wolterink, R. Sanders, and G. Krijnen, "Thin, flexible, capacitive force sensors based on anisotropy in 3d-printed structures," in *2018 IEEE SENSORS*, pp. 1–4, IEEE, 2018.

[2] A. Dijkshoorn, M. Schouten, G. Wolterink, R. Sanders, and G. Krijnen, "Characterizing the electrical properties of anisotropic, 3d-printed conductive sheets," in *2019 IEEE International Conference on Flexible and Printable Sensors and Systems (FLEPS)*, pp. 1–3, IEEE, 2019.

[3] J. Gooding and T. Fields, "3d printed strain gauge geometry and orientation for embedded sensing," in *58th AIAA/ASCE/AHS/ASC Structures, Structural Dynamics, and Materials Conference*, p. 0350, 2017.

[4] M. Maurizi, J. Slavič, F. Cianetti, M. Jerman, J. Valentinčič, A. Lebar, and M. Boltežar, "Dynamic measurements using fdm 3d-printed embedded strain sensors," *Sensors*, vol. 19, no. 12, p. 2661, 2019.

[5] A. Gong, H. Maunder, and D. Verstraete, "Development of an in-flight thrust measurement system for uavs," in *53rd AIAA/SAE/ASEE Joint Propulsion Conference*, p. 5092, 2017.

[6] "Development of a multi-rotor platform with integrated thrust sensor," Master's thesis, University of Twente, 2014.

[7] J. Bazin, *Strain Gauge Utilization for Aerial Vehicle Dynamic Load Measurement.* PhD thesis, 2016.

[8] C. S. Marchman, "Thrust sensing for small uavs," 2016.

[9] N. Instruments, "Strain gauge measurement–a tutorial," 1998.

[10] S. R. Katz, "Factors affecting strain gauge selection for smart structure applications," in *Smart Structures and Materials 1998: Sensory Phenomena and Measurement Instrumentation for Smart Structures and Materials*, vol. 3330, pp. 20–27, International Society for Optics and Photonics, 1998.

[11] H. Huang, G. M. Hoffmann, S. L. Waslander, and C. J. Tomlin, "Aerodynamics and control of autonomous quadrotor helicopters in aggressive maneuvering," in *2009 IEEE international conference on robotics and automation*, pp. 3277–3282, IEEE, 2009.

[12] W. Johnson, *Helicopter theory.* Courier Corporation, 2012.

[13] A. Pandzic, D. Hodzic, and A. Milovanovic, "Effect of infill type and density on tensile properties of plamaterial for fdm process.," *Annals of DAAAM & Proceedings*, vol. 30, 2019.

[14] M. R. Khosravani and T. Reinicke, "3d-printed sensors: Current progress and future challenges," *SENSORS AND ACTUATORS A-PHYSICAL*, vol. 305, 2020.

[15] M. Liu, Q. Zhang, Y. Shao, C. Liu, and Y. Zhao, "Research of a novel 3d printed strain gauge type force sensor," *Micromachines*, vol. 10, no. 1, p. 20, 2019.

[16] M. Amjadi, K.-U. Kyung, I. Park, and M. Sitti, "Stretchable, skin-mountable, and wearable strain sensors and their potential applications: a review," *Advanced Functional Materials*, vol. 26, no. 11, pp. 1678–1698, 2016.

[17] M. T. Rahman, R. Moser, H. M. Zbib, C. Ramana, and R. Panat, "3d printed high performance strain sensors for high temperature applications," *Journal of Applied Physics*, vol. 123, no. 2, p. 024501, 2018.

[18] A. Dorigato, V. Moretti, S. Dul, S. Unterberger, and A. Pegoretti, "Electrically conductive nanocomposites for fused deposition modelling," *Synthetic Metals*, vol. 226, pp. 7–14, 2017.

[19] K. Chizari, M. A. Daoud, A. R. Ravindran, and D. Therriault, "3d printing of highly conductive nanocomposites for the functional optimization of liquid sensors," *Small*, vol. 12, no. 44, pp. 6076–6082, 2016.

[20] A. Dijkshoorn, P. Werkman, M. Welleweerd, G. Wolterink, B. Eijking, J. Delamare, R. Sanders, and G. J. Krijnen, "Embedded sensing: Integrating sensors in 3-d printed structures," *Journal of Sensors and Sensor Systems*, vol. 7, no. 1, p. 169, 2018.

[21] J. Burstyn, N. Fellion, P. Strohmeier, and R. Vertegaal, "Printput: Resistive and capacitive input widgets for interactive 3d prints," in *IFIP Conference on Human-Computer Interaction*, pp. 332–339, Springer, 2015.

[22] S. Taillier, "Drone operator fined after uav crashed into geraldton triathlete," *ABC News*, vol. 13, 2014.

[23] A. Sanchez, L. G. Carrillo, E. Rondon, R. Lozano, and O. Garcia, "Hovering flight improvement of a quad-rotor mini uav using brushless dc motors," *Journal of Intelligent & Robotic Systems*, vol. 61, no. 1-4, pp. 85–101, 2011.

[24] L. Traub, "Validation of endurance estimates for battery powered uavs," *Aeronautical Journal*, vol. 117, no. 1197, pp. 1155–1166, 2013.

[25] R. J. Stephen, K. Rajanna, V. Dhar, K. K. Kumar, and S. Nagabushanam, "Thin-film strain gauge sensors for ion thrust measurement," *IEEE sensors journal*, vol. 4, no. 3, pp. 373–377, 2004.

[26] G. M. Hoffmann, H. Huang, S. L. Waslander, and C. J. Tomlin, "Precision flight control for a multi-vehicle quadrotor helicopter testbed," *Control engineering practice*, vol. 19, no. 9, pp. 1023–1036, 2011.

[27] N. Shahrubudin, T. Lee, and R. Ramlan, "An overview on 3d printing technology: technological, materials, and applications," *Procedia Manufacturing*, vol. 35, pp. 1286–1296, 2019.

[28] Z.-X. Low, Y. T. Chua, B. M. Ray, D. Mattia, I. S. Metcalfe, and D. A. Patterson, "Perspective on 3d printing of separation membranes and comparison to related unconventional fabrication techniques," *Journal of Membrane Science*, vol. 523, pp. 596–613, 2017.

[29] A. Standard *et al.*, "Standard terminology for additive manufacturing technologies," *ASTM International F2792-12a*, 2012.

[30] Y. Xu, X. Wu, X. Guo, B. Kong, M. Zhang, X. Qian, S. Mi, and W. Sun, "The boom in 3d-printed sensor technology," *Sensors*, vol. 17, no. 5, p. 1166, 2017.

[31] G. Wolterink, R. Sanders, F. Muijzer, B.-J. van Beijnum, and G. Krijnen, "3d-printing soft semg sensing structures," in *2017 IEEE SENSORS*, pp. 1–3, IEEE, 2017.

[32] J. Edgar and S. Tint, "Additive manufacturing technologies: 3d printing, rapid prototyping, and direct digital manufacturing," *Johnson Matthey Technology Review*, vol. 59, no. 3, pp. 193–198, 2015.

[33] T. Srivatsan and T. Sudarshan, *Additive manufacturing: innovations, advances, and applications.* CRC Press, 2015.

[34] V. G. Surange and P. V. Gharat, "3d printing process using fused deposition modelling (fdm)," *International Research Journal of Engineering and Technology (IRJET), 3 (3)*, 2016.

[35] J. C. Camargo, Á. R. Machado, E. C. Almeida, and E. F. M. S. Silva, "Mechanical properties of pla-graphene filament for fdm 3d printing," *The International Journal of Advanced Manufacturing Technology*, vol. 103, no. 5-8, pp. 2423–2443, 2019.

[36] K. M. Nampoothiri, N. R. Nair, and R. P. John, "An overview of the recent developments in polylactide (pla) research," *Bioresource technology*, vol. 101, no. 22, pp. 8493–8501, 2010.

[37] N. G. Tanikella, B. Wittbrodt, and J. M. Pearce, "Tensile strength of commercial polymer materials for fused filament fabrication 3d printing," *Additive Manufacturing*, vol. 15, pp. 40–47, 2017.

[38] S. Wickramasinghe, T. Do, and P. Tran, "Fdm-based 3d printing of polymer and associated composite: A review on mechanical properties, defects and treatments," *Polymers*, vol. 12, no. 7, p. 1529, 2020.

[39] S. H. Ahn, C. Baek, S. Lee, and I. S. Ahn, "Anisotropic tensile failure model of rapid prototyping parts-fused deposition modeling (fdm)," *International Journal of Modern Physics B*, vol. 17, no. 08n09, pp. 1510–1516, 2003.

[40] C. M. Vicente, T. S. Martins, M. Leite, A. Ribeiro, and L. Reis, "Influence of fused deposition modeling parameters on the mechanical properties of abs parts," *Polymers for Advanced Technologies*, vol. 31, no. 3, pp. 501–507, 2020.

[41] M. Dawoud, I. Taha, and S. J. Ebeid, "Mechanical behaviour of abs: An experimental study using fdm and injection moulding techniques," *Journal of Manufacturing Processes*, vol. 21, pp. 39–45, 2016.

[42] M. Seidl, J. Safka, J. Bobek, L. Behalek, and J. Habr, "Mechanical properties of products made of abs with respect to individuality of fdm production processes," *Modern Machinery Science Journal*, vol. 2, pp. 1748–1751, 2017.

[43] D. Croccolo, M. De Agostinis, and G. Olmi, "Experimental characterization and analytical modelling of the mechanical behaviour of fused deposition processed parts made of abs-m30," *Computational Materials Science*, vol. 79, pp. 506–518, 2013.

[44] S. Park, J. Yoo, and S. Shin, "Improved aerodynamic analysis for multirotor-type uas flight simulation using dynamic inflow and rigid blade flapping," *Journal of Aerospace Engineering*, vol. 33, no. 4, p. 04020021, 2020.

[45] A. R. S. Bramwell, D. Balmford, and G. Done, *Bramwell's helicopter dynamics.* Elsevier, 2001.

[46] M. Bangura, M. Melega, R. Naldi, and R. Mahony, "Aerodynamics of rotor blades for quadrotors," *arXiv preprint arXiv:1601.00733*, 2016.

[47] J. D. Singleton and W. T. Yeager Jr, "Important scaling parameters for testing model-scale helicopter rotors," *Journal of Aircraft*, vol. 37, no. 3, pp. 396–402, 2000.

[48] N. Nowicki, "Measurement and modelling of multicopter uas rotor blade deflection in hover," 2016.

[49] APC, "Performance data." https://www.apcprop.com/technical-information/performance-data/.

[50] M. Husaini, Z. Samad, and M. R. Arshad, "Autonomous underwater vehicle propeller simulation using computational fluid dynamic," *Computational Fluid Dynamics Technologies and Applications*, pp. 293–314, 2011.

[51] F. Liebers, "Resonance vibrations of aircraft propellers," 1932.

[52] A. L. Window and S. Geoffry, "Holister," *Strain gauge technology. Applied science publishers*, 1982.

[53] Protoplant, "Conductive pla." https://www.proto-pasta.com/pages/conductive-pla.

[54] K. Kim, J. Park, J.-h. Suh, M. Kim, Y. Jeong, and I. Park, "3d printing of multiaxial force sensors using carbon nanotube (cnt)/thermoplastic polyurethane (tpu) filaments," *Sensors and Actuators A: Physical*, vol. 263, pp. 493–500, 2017.

[55] M. Khan, G. Dumstorff, C. Winkelmann, and W. Lang, "Investigations on noise level in ac- and dc-bridge circuits for sensor measurement systems," in *8th GMA/ITG Conference Sensors and Measurement Systems*, 2016.

[56] M. Babalola and V. Akpan, "Experimental determination of the poisson's ratio (μ) and gauge factor (k) values of a practical strain gauge (120-sra, foil type)," *Ife Journal of Science*, vol. 8, no. 1, pp. 47–58, 2006.

[57] M. Rismalia, S. Hidajat, I. Permana, B. Hadisujoto, M. Muslimin, and F. Triawan, "Infill pattern and density effects on the tensile properties of 3d printed pla material," in *Journal of Physics: Conference Series*, vol. 1402, p. 044041, IOP Publishing, 2019.

[58] A. Franchi and A. Mallet, "Adaptive closed-loop speed control of bldc motors with applications to multi-rotor aerial vehicles," in *2017 IEEE International Conference on Robotics and Automation (ICRA)*, pp. 5203–5208, IEEE, 2017.

[59] P. Sanchez-Cuevas, G. Heredia, and A. Ollero, "Characterization of the aerodynamic ground effect and its influence in multirotor control," *International Journal of Aerospace Engineering*, vol. 2017, 2017.

[60] S. A. Conyers, M. J. Rutherford, and K. P. Valavanis, "An empirical evaluation of ground effect for small-scale rotorcraft," in *2018 IEEE International Conference on Robotics and Automation (ICRA)*, pp. 1244–1250, IEEE, 2018.

[61] D. D. C. Bernard, M. Giurato, F. Riccardi, and M. Lovera, "Ground effect analysis for a quadrotor platform," in *Advances in Aerospace Guidance, Navigation and Control*, pp. 351–367, Springer, 2018.

[62] K. Hosokawa, "Effect of moment of inertia of attached mass on natural frequencies of cantilevered symmetrically laminated plates," *EPI International Journal of Engineering*, vol. 1, no. 2, pp. 35–39, 2018.

[63] D. E. Oku and E. P. Obot, "Comparative study of pd, pi and pid controllers for control of a single joint system in robots,"

[64] W. Altmann, *Practical process control for engineers and technicians*. Elsevier, 2005.

[65] W. A. Poe and S. Mokhatab, *Modeling, control, and optimization of natural gas processing plants*. gulf professional publishing, 2016.

[66] M. Boerlage, R. Tousain, and M. Steinbuch, "Reference trajectory relevant jerk derivative feedforward control for motion systems," *Measurement*, vol. 2, p. 3, 2004.

[67] M. Tariq, T. Bhattacharya, N. Varshney, and D. Rajapan, "Fast response antiwindup pi speed controller of brushless dc motor drive: Modeling, simulation and implementation on dsp," *Journal of electrical systems and information technology*, vol. 3, no. 1, pp. 1–13, 2016.

[68] B. Singh and S. Singh, "State of the art on permanent magnet brushless dc motor drives," *journal of power electronics*, vol. 9, no. 1, pp. 1–17, 2009.

[69] O. Ono, "Parameter tuning of pid control based on pole-zero area placement using characteristics graphic patterns," *IFAC Proceedings Volumes*, vol. 26, no. 2, pp. 483–486, 1993.

[70] R. Kumar, S. Singla, and V. Chopra, "Comparison among some well known control schemes with different tuning methods," *Journal of applied research and technology*, vol. 13, no. 3, pp. 409–4015, 2015.

[71] D. Kosmas, "Model-based hysteresis compensation and control with 3d printed lousy sensors," Master's thesis, University of Twente, 2020.

A Appendix 1

A.1 Modal analysis of propeller

Modal analysis was performed on an 8x4.5 inch propeller to investigate the effect of material properties on the natural frequency of the propeller. Results from the modal analysis are shown below for ABS Plastic and PLA in Figures A.1 - A.6:

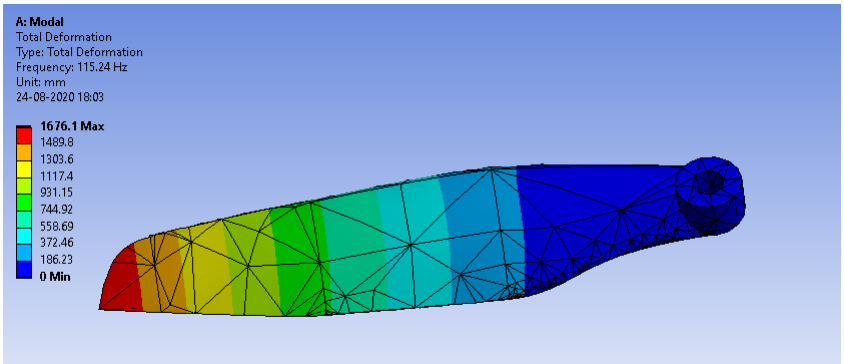

Figure A.1: First mode shape of ABS Plastic

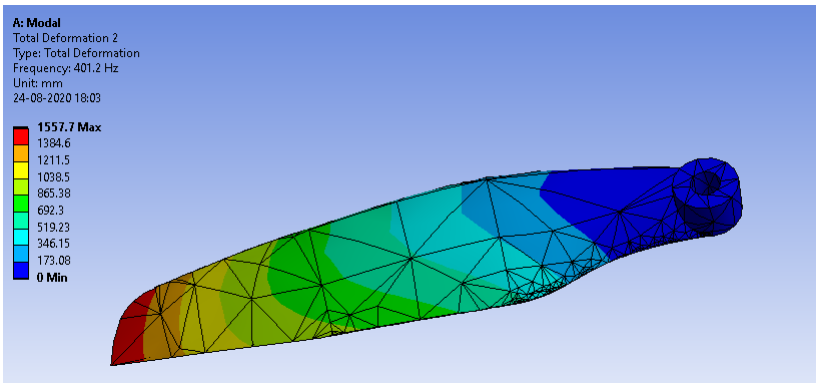

Figure A.2: Second mode shape of ABS Plastic

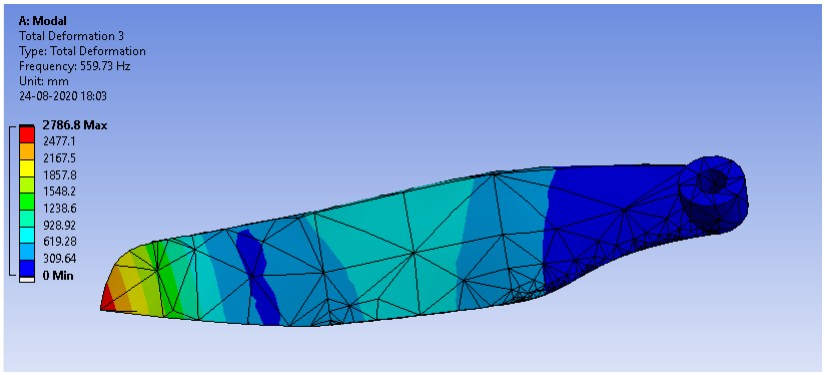

Figure A.3: Third mode shape of ABS Plastic

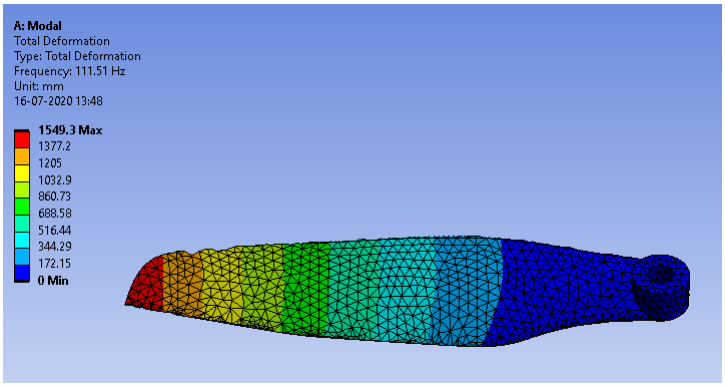

Figure A.4: First mode shape of PLA

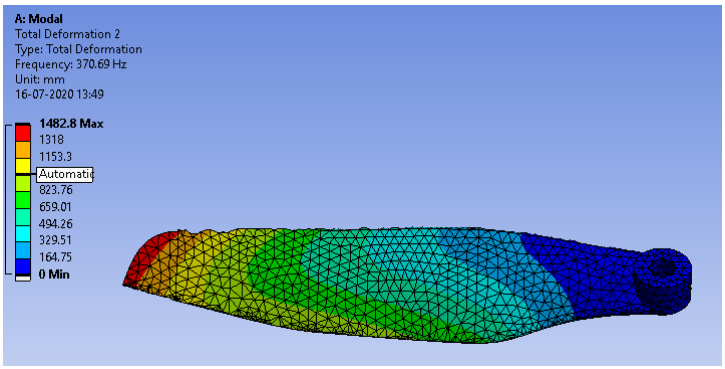

Figure A.5: Second mode shape of PLA

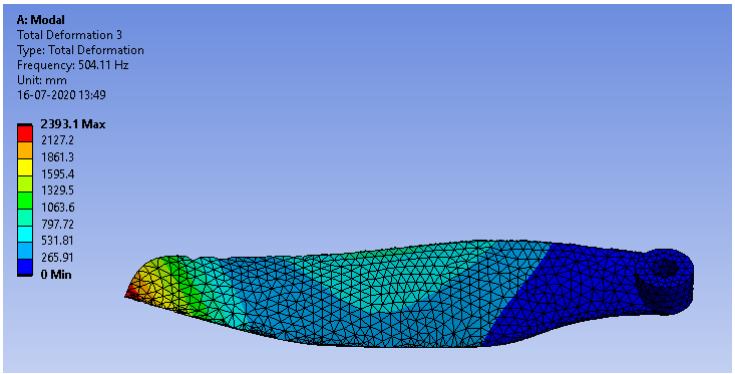

Figure A.6: Third mode shape of PLA

A.2 Controller response in ground effect

Figure A.7 – A.10 report the results obtained with the designed controller at a distance of 90 mm - 150 mm with increments of 20 mm. When compared to results for 50 mm and 70 mm in Figure 7.10 and 7.11, the error between the desired thrust and measured thrust is much smaller. Also, the measured thrust nicely follows the desired thrust.

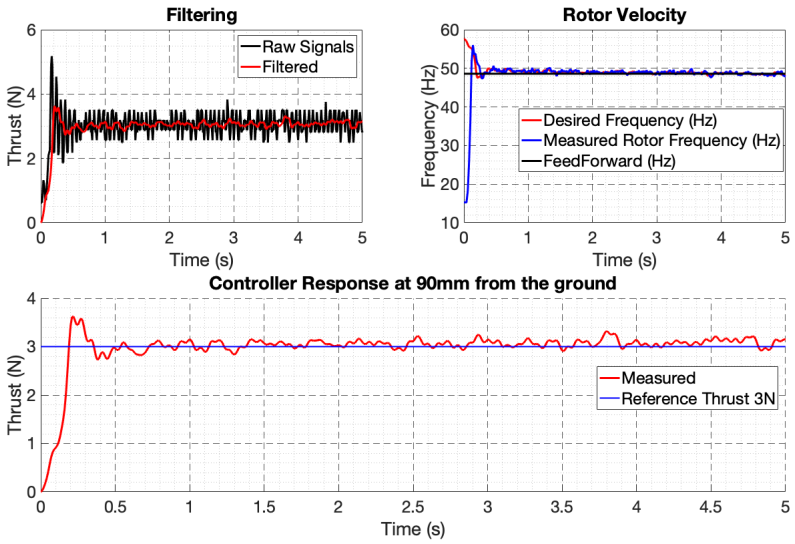

Figure A.7: Controller response at 90 mm from the ground

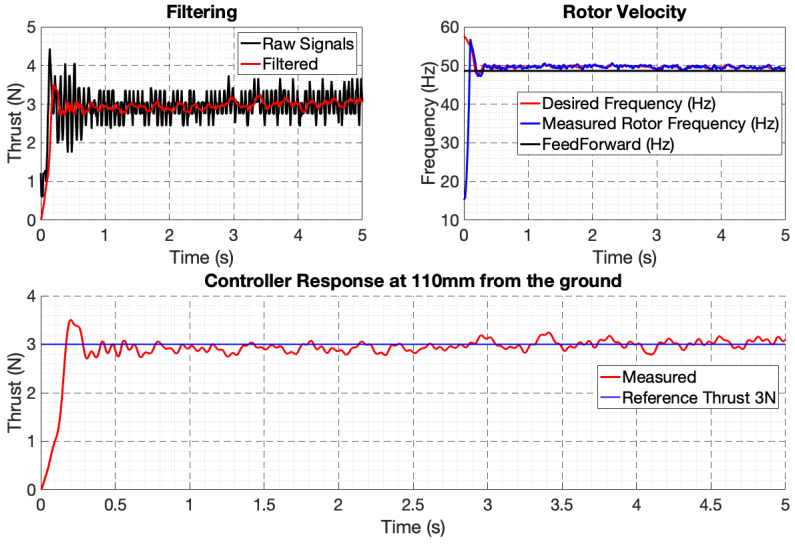

Figure A.8: Controller response at 110 mm from the ground

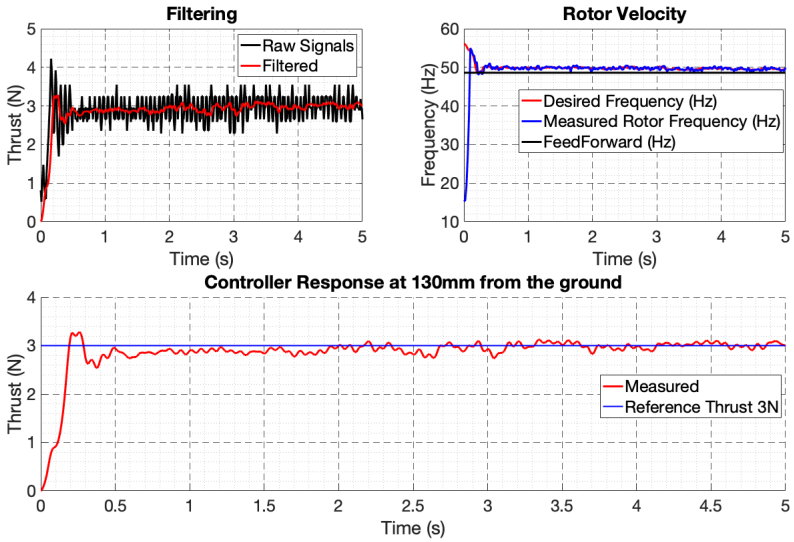

Figure A.9: Controller response at 130 mm from the ground

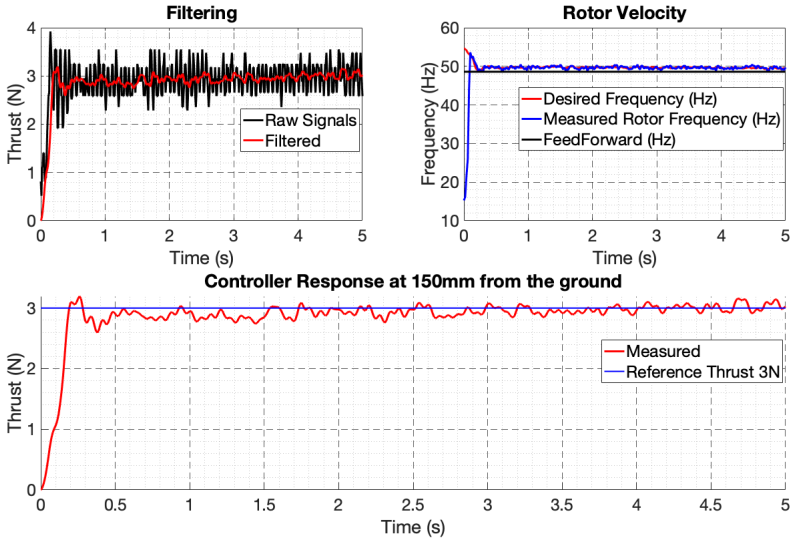

Figure A.10: Controller response at 150 mm from the ground